A measurement of W+jet and Z+jet cross sections in the tau decay channel, and their ratio in the ATLAS experiment

Peter Kadlečík

Department of High Energy Physics
Niels Bohr Institute
The PhD School of Science
Faculty of Science
University of Copenhagen
Denmark

A thesis submited for the degree
PhilosophiæDoctor (PhD)

July 2012

Abstract

English version

The amount of collision data delivered by the Large Hadron Collider and collected by the ATLAS detector in Spring 2011 was sufficient enough so that a variety of important measurements could be carried out. Among them are the measurements of the W+jet and the Z+jet cross sections in the tau decay channel of the W and Z boson, and the W+jet to Z+jet cross sections ratio measurement, the so called R_{JET} measurement. The goal of these measurements is, by comparing the theoretical predictions and the measured quantities, to investigate, whether signs of physics beyond the Standard Model can be observed in the W($\rightarrow \tau\nu$)+jet or the Z($\rightarrow \tau\tau$)+jet signatures. The R_{JET} measurement is an extra measurement which tested the possibility of canceling some systematic uncertainties which entered both W($\rightarrow \tau\nu$)+jet and Z($\rightarrow \tau\tau$)+jet cross section measurements, and thus provide a measurement with an enhanced sensitivity. This thesis provides the W($\rightarrow \tau\nu$)+jet and the Z($\rightarrow \tau\tau$)+jet observations and cross section measurements and their R_{JET} ratio is estimated. The W($\rightarrow \tau\nu$)+jet cross section is estimated to be $\sigma_{W+jet} = 1.08 \pm 0.06(\mathrm{stat.}) \pm 0.21(\mathrm{syst.}) \pm 0.03(\mathrm{lumi.})$ nb, and the Z($\rightarrow \tau\tau$)+jet cross section is estimated to be $\sigma_{Z+jet} = 0.130 \pm 0.015(\mathrm{stat.}) \pm 0.023(\mathrm{syst.}) \pm 0.004$ (lumi.) nb. The R_{JET} ratio is estimated to be $R_{\mathrm{JET}} = 8.3 \pm 1.0(\mathrm{stat.}) \pm 1.5(\mathrm{syst.})$. The measured cross sections as well as the R_{JET} ratio correspond within the uncertainty with the theoretical predictions. Future improvements of the analysis are discussed in the summary of the thesis.

Abstract

Dansk version

Antallet af kollisioner opsamlet af ATLAS eksperimentet ved The Large Hadron Collider war i foråret 2011 tilstrækkeligt til at en serie vigtige målinger kunne udføres. Blandt dem var målingen af W+jet samt Z+jet tværsnittet i tau henfaldskanalerne for W og Z bosonerne og W+jet/Z+jet tværsnit forholdet, den såkaldte R_{JET} måling. Motivationen for disse målinger er at søge efter ny fysik der afviger fra standardmodellen ved at sammenligne med teoretiske forudsigelser for W($\rightarrow \tau\nu$)+jet eller Z($\rightarrow \tau\tau$)+jet signaturerer. Med R_{JET} målingen forbedres følsomheden da dan giver mulighed for at nedbringe visse systematiske usikkerheder som ellers påvirker både W($\rightarrow \tau\nu$)+jet og Z($\rightarrow \tau\tau$)+jet tværsnit målingerne. I denne afhandling måles W($\rightarrow \tau\nu$)+jet og Z($\rightarrow \tau\tau$)+jet tværsnittet og deres R_{JET} forhold estimeres. Tværsnittet for W($\rightarrow \tau\nu$)+jet måles til at være σ_{W+jet} = 1.08 $\pm$ 0.06(stat.) $\pm$ 0.21(syst.) $\pm$ 0.03(lumi.) nb. Tværsnittet for Z($\rightarrow \tau\tau$)+jet er målt til: σ_{Z+jet} = 0.130 $\pm$ 0.015(stat.) $\pm$ 0.023(syst.) $\pm$ 0.004 (lumi.) nb. R_{JET} forholdet er estimeret til R_{JET} = 8.3 $\pm$ 1.0 (stat.) $\pm$ 1.5 (syst.). De målte tværsnit samt R_{JET} forholdet er konsistente med teoretiske forudsigelser fra standardmodellen. Yderligere forbedring af analysen diskuteres i konklusionen af afhandlingen.

Acknowledgements

For many useful comments and advices concerning this thesis, but also for advices throughout the whole PhD study, I would like to thank my supervisor Mogens Dam. For many fruitful discussions on various topics concerning high energy physics, and for being great friends, I would like to thank Stefania Xella, Zofia Czyczuła, Margar Simonyan and Pavel Ježˇ. For providing funding of my research I would like to thank the PhD school of science at the Copenhagen University. Last but not least, for a friendly support in my research, and creating a great working environment, I would like to thank the whole HEP group at the Niels Bohr Institute.

Contents

1

Introduction

Over the last three centuries, the understanding of physics and Nature in general has evolved dramatically. From trying to explain phenomena observed directly in our immediate surroundings we have come to the point of being able to explain events at scales smaller than the atomic nuclei (10^{-15} m) and phenomena at the scale of Galaxies.

The history of physics is however not only a success story. Several attempts have been done to develop a "unified theory of physics", however, so far all of them have failed. When in the early part of the 20th century the physicists saw "only two little clouds in the blue sky of physics"[1] nobody could have known that during the following decades several physics revolutions would happen. The first revolution was the Einstein's Theory of Relativity that has changed our view on matters such as time and space. The other revolution was started by physicists such as Planck, Bohr, Schrödinger and Heisenberg and lead to Quantum Mechanics.

Currently there is no unified theory that would explain phenomena at the scales of stars and galaxies (described by the General Relativity), and at the same time explain phenomena at scales of atoms, nuclei and elementary particles (described by Quantum Mechanics and the so-called Standard Model). Some physics theories, such as the so-called String theory, claim to be able to provide this unification, while some other exotic physics models use a different approach and try to address some single problems which need to be solved before unifying the physics. All of these physics theories have yet to be proven.

[1] William Thomson, 1st Baron Kelvin (1824 - 1907) in 1901 in the lecture with the title Nineteenth-Century Clouds over the Dynamical Theory of Heat and Light (1).

1. INTRODUCTION

In this thesis, first, the theory of the Standard Model and an experimental facility used for studying it and testing it will be described. Later, results of measurements in which we could potentially observe discrepancies between the Standard Model predictions and real data observations will be presented. The real data is obtained from the ATLAS detector built at the Large Hadron Collider at CERN [1]. In the last part I summarize the measurements, discuss the results, and discuss some possible improvements of the measurements for the future.

[1] European Organization for Nuclear Research

2

Theoretical Overview

2.1 Standard Model

The Standard Model is a theory in physics that precisely describes Nature at the scales from elementary particles up to atoms. From an experimental point of view it is a very successful theory, and currently there is no experiment that has showed a confirmed disagreement between measurement and Standard Model predictions. The particles of the Standard Model include three families of fermions (and their corresponding anti-fermions) and gauge bosons, as illustrated in figure 2.1.

The fermions are divided into leptons and quarks, which, within the Standard Model, are represented by fermion fields. Imposing local gauge invariance on the fermion fields results into the introduction of the so-called gauge fields. From the gauge fields, the physical fields that provide interactions between the fermions can be derived. The electromagnetic interaction is provided by the photon γ, the weak interactions are provided by the $W^{\pm}$ and the Z boson, and the strong interaction is provided by the gluons g.

The Lagrangian of the Standard Model, $\mathcal{L}_{\mathrm{SM}}$, consists of the Lagrangian of the unified electroweak sector, $\mathcal{L}_{\mathrm{EW}}$, and the Quantum Chromodynamics (QCD) Lagrangian, $\mathcal{L}_{\mathrm{QCD}}$, which describes strong interactions. The $\mathcal{L}_{\mathrm{SM}}$ is invariant to the local group transformation $SU(2)_L \otimes U(1)_Y \otimes SU(3)_C$, where Y represents the weak hypercharge, L the left-handed chirality and C the color charge of strong interactions. If the neutrinos are massless, the Standard Model includes 18 free parameters and if the neutrinos have mass it includes 25 free parameters.

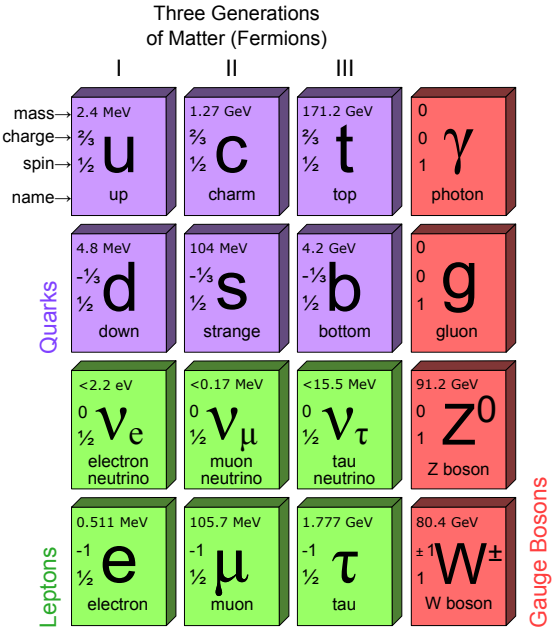

Figure 2.1: Particles of the Standard Model.

2.1.1 The Electroweak Lagrangian

The $\mathcal{L}_{\text{EW}}$ (2) (3) is based on the transformation $SU(2)_L \otimes U(1)_Y$, where the transformation $SU(2)_L$ denotes the rotation in the space of the weak isospin, T, and the $U(1)_Y$ the rotation in the space of the weak hypercharge, Y. Both Y and T are quantum numbers of the Standard Model particles, and the relation between Y and T_3, which is the third component of T, can be expressed via the Gell-Mann-Nishijima equation as $Y = 2(Q - T_3)$, where Q is the electric charge.

Depending on their chiral projections, the fermions are grouped as SU(2) singlets (right-handed, R; $T = 0$) and SU(2) doublets (left-handed, L; $T_3 = \pm 1/2$). For the first family (analogous for the second and third family) for the quark sector, this can be written as:

$$\psi_1(x) = \begin{pmatrix} u \\ d' \end{pmatrix}_L, \quad \psi_2(x) = u_R, \quad \psi_3(x) = d_R, \tag{2.1}$$

where the u and d constituents of the fields $\psi(x)$ are the Dirac spinors for each fermion type with the given chirality, and d'_L is a linear combination of mass eigenstate spinors

d, s and b, following the formula:

$$\begin{pmatrix} d' \\ s' \\ b' \end{pmatrix} = CKM \begin{pmatrix} d \\ s \\ b \end{pmatrix},$$

where CKM is the Cabbibo-Kobayashi-Maskawa matrix (4). For the lepton sector, the fields $\psi_1(x)$, $\psi_2(x)$, $\psi_3(x)$ from 2.1 have the form:

$$\psi_1(x) = \begin{pmatrix} \nu_e \\ e^- \end{pmatrix}_L, \quad \psi_2(x) = \nu_{eR}, \quad \psi_3(x) = e^-_R, \tag{2.2}$$

The fields $\psi(x)$ from 2.1 and 2.2 transform under the $SU(2)_L \otimes U(1)_Y$ symmetry as:

$$\begin{aligned} \psi_1(x) &\to \psi_1'(x) = e^{iY_1\beta(x)+iT_i\alpha^i(x)}\psi_1(x), \\ \psi_2(x) &\to \psi_2'(x) = e^{iY_2\beta(x)}\psi_2(x), \\ \psi_3(x) &\to \psi_3'(x) = e^{iY_3\beta(x)}\psi_3(x), \end{aligned} \tag{2.3}$$

where $\alpha^i(x)$, $\beta(x)$ (for $i = 1, 2, 3$) are real functions, the parameters Y_1, Y_2 and Y_3 are the hypercharges of the given fields $\psi(x)$, and T_i are the weak isospin components that can be expressed using the Pauli matrices, σ_i, as $T_i = \sigma_i/2$.

The Lagrangian $\mathcal{L}_{\mathrm{EW}}$ can be in the simplest form expressed as:

$$\mathcal{L}_{\mathrm{EW}} = \mathcal{L}_{\mathrm{f}} + \mathcal{L}_{\mathrm{gauge}} + \mathcal{L}_{\phi} + \mathcal{L}_{\mathrm{Yukawa}} \tag{2.4}$$

The term $\mathcal{L}_{\mathrm{f}}$ represents the kinetic energies of the fermions and their interactions with the gauge fields. It is expressed as:

$$\mathcal{L}_{\mathrm{f}} = \sum_{j=1}^{3} (\overline{\psi}_L^j i\gamma^\mu (D_L)_\mu \psi_L^j + \overline{\psi}_R^j i\gamma^\mu (D_R)_\mu \psi_R^j), \tag{2.5}$$

where j is the fermion family index, and γ^μ are the gamma matrices. The coupling of the fermions to the gauge fields is "hidden" in the covariant derivatives $(D_L)_\mu$ and $(D_R)_\mu$, which have the forms:

$$\begin{aligned} (D_L)_\mu &= \partial_\mu + igT_iW_\mu^i + ig'B_\mu Y/2, \\ (D_R)_\mu &= \partial_\mu + ig'B_\mu Y/2, \end{aligned} \tag{2.6}$$

where g' is the $U(1)_Y$ coupling constant, and g is the $SU(2)_L$ coupling constant, both connected to the electric charge e through the Weinberg angle, θ_W, as $e = g\sin\theta_W = g'\cos\theta_W$.

The Lagrangian $\mathcal{L}_{\text{gauge}}$ describes kinetic energies and self-interactions of the gauge fields:

$$\mathcal{L}_{\text{gauge}} = -\frac{1}{4}F^i_{\mu\nu}F^{\mu\nu i} - \frac{1}{4}B_{\mu\nu}B^{\mu\nu} \tag{2.7}$$

The four gauge fields strength tensors $F^i_{\mu\nu}$ (for $i = 1, 2, 3$) and $B_{\mu\nu}$ are expressed via the gauge fields B_μ and W^i_μ as:

$$B_{\mu\nu} = \partial_\mu B_\nu - \partial_\nu B_\mu, \qquad F^i_{\mu\nu} = \partial_\mu W^i_\nu - \partial_\nu W^i_\mu - g\epsilon_{ijk}W^j_\mu W^k_\nu, \tag{2.8}$$

where ϵ_{ijk} is the Levi-Civita symbol.

The $\mathcal{L}_\phi$ in the equation 2.4 describes the scalar part of the Lagrangian:

$$\mathcal{L}_\phi = ((D_L)^\mu\phi)^\dagger(D_L)_\mu\phi - V(\phi), \tag{2.9}$$

where ϕ is a complex $SU(2)$ isospin doublet of two scalar fields, and the potential $V(\phi)$ is expressed as:

$$V(\phi) = \mu^2\phi^\dagger\phi + \lambda(\phi^\dagger\phi)^2 \ , \lambda > 0 \tag{2.10}$$

For $\mu^2 < 0$ there will be a spontaneous symmetry breaking, and the minimum of the potential V will occur at a non-zero value v, often referred to as the vacuum expectation value. The λ term in equation 2.10 describes quadratic self-interaction between the fields ϕ. After a suitable gauge transformation ϕ can be expressed as:

$$\phi = \frac{1}{\sqrt{2}}\begin{pmatrix} 0 \\ v + h \end{pmatrix},$$

with h usually referred to as the Higgs field.

The physical fields of photons (A_μ), Z (Z_μ) and $W^\pm$ bosons are defined via the gauge fields B_μ and W^i_μ as:

$$A_\mu = \frac{g'W^3_\mu + gB_\mu}{\sqrt{g'^2 + g^2}}, \tag{2.11}$$

$$Z_\mu = \frac{gW^3_\mu - g'B_\mu}{\sqrt{g'^2 + g^2}}, \tag{2.12}$$

$$W^{\pm} = \frac{1}{\sqrt{2}}(W^1 \mp iW^2), \tag{2.13}$$

and after the spontaneous symmetry breaking the physical fields obtain the masses:

$$\mathrm{M}_W = \frac{gv}{2} \tag{2.14}$$

$$\mathrm{M}_Z = \frac{\mathrm{M}_W\sqrt{g'^2 + g^2}}{g} \tag{2.15}$$

The field of the photons remains massless.

The last term in equation 2.4, $\mathcal{L}_{\mathrm{Yukawa}}$, describes the coupling of the fermions to the Higgs field through which the fermions obtain masses. After the spontaneous symmetry breaking, in the unitary gauge, $\mathcal{L}_{\mathrm{Yukawa}}$ can be written in the form:

$$\mathcal{L}_{\mathrm{Yukawa}} = -(1 + \frac{h}{v})\sum_{i=1}^{3}(m_d^i\overline{d}_i d^i + m_u^i\overline{u}_i u^i + m_l^i\overline{l}_i l^i), \tag{2.16}$$

where the sum runs over the three fermion families and the spinors d_i, u_i and l_i, with the masses m_d^i, m_u^i and m_l^i describe the down-type quarks, up-type quarks and leptons in each family i. The masses of the fermions represent 9 parameters of the Standard Model. In equation 2.16, the neutrinos are considered massless. In case the neutrinos have non-zero masses, additional three parameters, m_ν^i, enter into the Standard Model[1] with additional terms $(m_\nu^i\overline{\nu}_i\nu^i)$ contributing into the sum in the $\mathcal{L}_{\mathrm{Yukawa}}$ expression.

The W and Z bosons were discovered at the UA1 and UA2 experiments in proton-antiproton collisions at the SPS accelerator at CERN, in 1983 (5) (6), after their existence was predicted by the Standard Model.

The mass of the W boson can be estimated as $\mathrm{M}_W \simeq \frac{(\pi\alpha/\sqrt{2}G_F)^{1/2}}{\sin(\theta_W)}$, where we use the knowledge of the Fermi constant $G_F \simeq 1.1663 \times 10^{-5}$ GeV^{-2} (related to the vacuum expectation value as $v = (\sqrt{2}G_F)^{-1/2} \simeq 246$ GeV), which can be estimated in muon lifetime measurements (7), the fine structure constant $\alpha \simeq 1/137.036$ determined from e.g. the measurement of the anomalous magnetic moment of the electron (8),

[1] In addition to the three neutrino mass parameters, if the neutrinos have non-zero masses, 3+1 parameters (three angles and one phase) in the so-called Maki-Nakagava-Sakata matrix, which describes neutrino oscillations and for neutrinos it can be interpreted in the same way as the CKM matrix for the down-type quarks, contribute to the additional free parameters of the Standard Model.

and $\sin^2(\theta_W) \simeq 0.23$ measured e.g. in the process of deep inelastic neutrino-nucleon scattering, from the neutral current to charged current cross sections ratio (9). The expected masses of the W boson and the Z boson are $M_W \simeq 80.4$ GeV, and $M_Z \simeq 91.2$ GeV. The constants G_F, α and M_Z can fully substitute the parameters g, g' and v, and are the most precisely measured parameters of the Standard Model.

Both W and Z bosons have very short lifetimes of $\sim 10^{-25}$ s and decay immediately. Their branching ratios are shown in table 2.1.

W+ decay modes	Branching ratio
$e^+\nu$	(10.75 ± 0.13) %
$\mu^+\nu$	(10.57 ± 0.15) %
$\tau^+\nu$	(11.25 ± 0.20) %
hadrons	(67.60 ± 0.27) %
Z decay modes	
e^+e^-	(3.363 ± 0.004) %
$\mu^+\mu^-$	(3.366 ± 0.007) %
$\tau^+\tau^-$	(3.367 ± 0.008) %
$\nu\nu$	(20.00 ± 0.06) %
hadrons	(69.91 ± 0.06) %

Table 2.1: Main branching fractions of the W^+ (W^- is charged conjugate) and Z bosons. Hadrons denote the decay into a quark and an anti-quark (4).

2.1.2 Quantum Chromodynamics

The $\mathcal{L}_{\mathrm{QCD}}$ lagrangian describes the strong interactions (4). It is based on the $SU(3)_C$ symmetry. The $\mathcal{L}_{\mathrm{QCD}}$ can be written as:

$$\mathcal{L}_{\mathrm{QCD}} = \sum_q \overline{\psi}_{q,a}(i\gamma^\mu \partial_\mu \delta_{ab} - g_s \gamma^\mu t^C_{ab} A^C_\mu - m_q \delta_{ab})\psi_{q,b} - \frac{1}{4} F^A_{\mu\nu} F^{\mu\nu A} \tag{2.17}$$

where the $\psi_{q,a}$ is the quark-field spinor for a quark of flavour q and mass m_q. The indices a and b run from $a, b = 1$ to $N_C = 3$ and represent the so-called "color" charge of the quarks ("red", "green", "blue"), which is a quantum number carried only by quarks (anti-quarks) and gluons. A^C_μ describes the gluon fields ($N_c^2 - 1 = 8$ kinds of gluons), t^C_{ab} correspond to eight 3×3 matrices representing the generators of the $SU(3)$ group and g_s is the QCD coupling constant. The field strength tensors $F^A_{\mu\nu}$ are

expressed as:

$$F^A_{\mu\nu} = \partial_\mu A^A_\nu - \partial_\nu A^A_\mu - g_s f_{ABC} A^B_\mu A^C_\nu \tag{2.18}$$

where f_{ABC} are the structure constants of the $SU(3)$ group. In the formula for $\mathcal{L}_{\text{QCD}}$ the first term describes the kinetic energy of the quarks and the interaction of quarks and gluons, while the second term, together with equation 2.18, describes kinetic energy of the gluons and self interaction of the gluons (represented by the last term in equation 2.18) typical for non-Abelian gauge theories.

The constant g_s is related to a more widely used α_s, called the strong coupling constant, as $\alpha_s = \frac{g_s^2}{4\pi}$. At the energy scale Q, representing the momentum transfer in the strong interaction, the strong coupling constant $\alpha_s(Q)$ indicates the effective strength of the interaction (4). In figure 2.2, the scale dependence of $\alpha_s(Q)$ is demonstrated and a good agreement of the theoretical prediction of $\alpha_s(Q)$, represented by the combined world average curves, and the recent measurements is shown, providing a strong evidence of the correct predictions of the QCD.

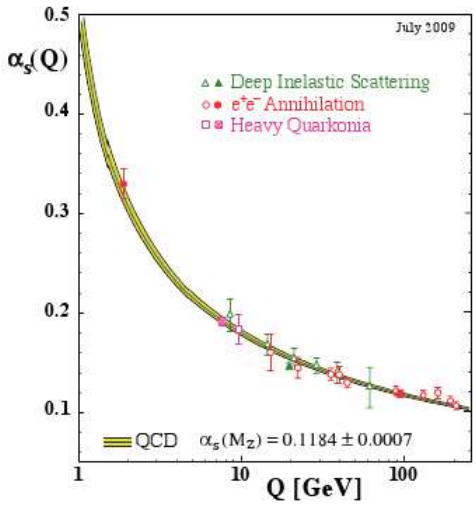

Figure 2.2: Measurements of the α_s in various experiments as a function of the respective energy scale Q. The curves are QCD predictions for the combined world average value of α_s (10).

A typical feature of the QCD is the so-called color confinement. Due to the color confinement, which shows up as a linear increase in the potential energy between two

particles with color as a function of the distance of the particles, in nature it is impossible to observe free quarks. Quarks are bound in color-neutral hadrons. The process of the formation of color neutral hadrons from colored particles, such as quarks or gluons, is called hadronization, and it is a process happening in the non-perturbative QCD regime. The hadronization usually results in the creation of several stable hadrons, which can be associated into collimated bunches called jets. Depending on how many quarks are bound in the hadron, the hadrons are divided in mesons (particles composed of a quark and an anti-quark) and baryons (particles composed of three quarks). All observed hadrons are color singlets.

The only stable hadron is the proton. The proton is composed of two u quarks and one d quark. These quarks are referred to as the "valence quarks" and their interaction is mediated by the gluons. The gluons can self interact, and/or create virtual quark pairs referred to as the "sea quarks". All constituents of the proton are the so-called partons. It is useful to define the so-called Bjorken variable x which represents what fraction of the total momentum of the proton p_{proton} is carried by a given parton a: $p_a = p_{\text{proton}} \cdot x$ (4). The probability density of finding in the proton the parton a with the momentum fraction x, in an interaction at the energy scale Q^2, is given by the parton density function $f_a(x, Q^2)$. $f_a(x, Q^2)$ as a function of Q^2 is described by the Dokshitzer-Gribov-Lipatov-Alterelli-Parisi evolution equations (11). As a function of x, for two different energy scales Q^2, the $f_a(x, Q^2)$ is shown in figure 2.3. As seen, a significant portion of the momentum of the proton is carried not only by the valence quarks but also by the gluons and the sea quarks. Moving from the scale $Q^2 = 10$ GeV^2 to the scale $Q^2 = 10^4$ GeV^2 a large difference in the $f_a(x, Q^2)$ can be observed. This is caused by the fact that at increasingly higher momentum transfers (i.e. $\lambda = \hbar/|Q| \ll d$, where λ is the wavelength of a virtual photon, $\hbar$ is the Planck constant and d is the size of the proton) the proton structure becomes increasingly more dominated by soft splittings of $g \to gg$ and $g \to q\overline{q}$. As shown in figure 2.3, at the values of x $< 10^{-2}$ to 10^{-3} these contributions can increase with the increasing Q^2 by orders of magnitude.

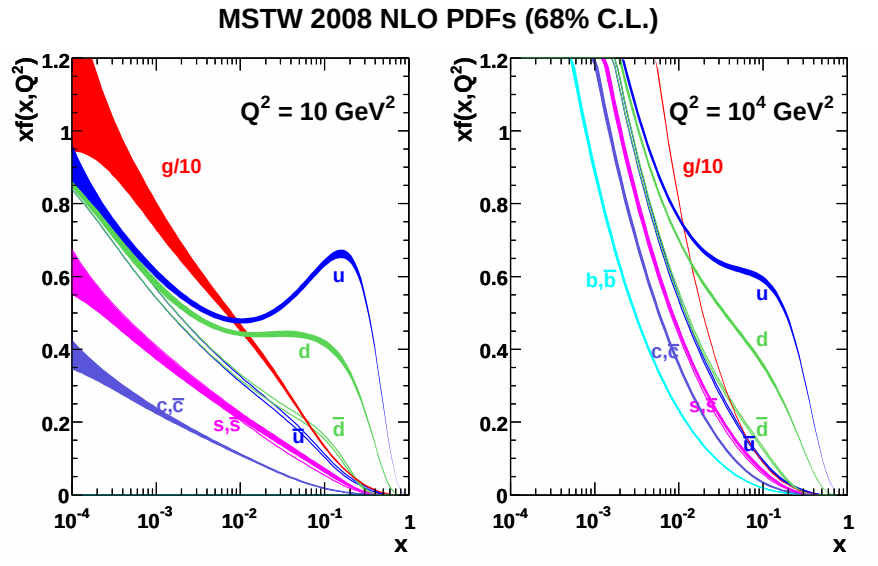

Figure 2.3: Distributions of x times the unpolarized parton distributions $f(x)$ for the valence quarks u (blue) and d (green), the sea quarks and the gluons (note that the gluon distributions is scaled by factor 1/10). The distributions to the left are for the scale $Q^2 = 10$ GeV^2 and to the right for $Q^2 = 10^4$ GeV^4. The distributions are drawn within the 68 % confidence level. The figures are taken from (12).

2.1.3 Resonance production in proton-proton collisions

The production cross section of a resonance "X" in proton-proton collision can be expressed as (4):

$$\sigma_{p_1p_2\to X} = \sum_{i,j} \int \mathrm{d}x_i \mathrm{d}x_j f_{i/p_1}(x_i, \mu_F^2) f_{j/p_2}(x_j, \mu_F^2) \hat{\sigma}_{ij\to X}(x_i x_j s, \mu_R^2, \mu_F^2), \tag{2.19}$$

where $\sum_{i,j}$ runs over all combinations of partons i, in the proton p_1, and j, in the proton p_2, x_i and x_j are the Bjorken variables, $\sqrt{s}$ is the center-of-mass energy of the collision, $f_{i/p_1}(x_i, \mu_F^2)$ and $f_{j/p_2}(x_j, \mu_F^2)$ are the parton density functions of the protons p_1 and p_2 for the factorization scale μ_F, which is an arbitrary energy scale that controls up to which scale the parton emission is handled by the parton density function, instead of the partonic cross section $\hat{\sigma}_{ij\to X}$. The renormalization scale μ_R is an arbitrary (unphysical) scale in which terms the renormalized coupling $\alpha_s(\mu_R^2)$ is expressed. To simplify the calculations in the perturbative QCD, μ_R is usually taken as $\mu_R \simeq Q$, with Q as the momentum transfer.

The lowest order W and Z boson production mechanisms in proton-proton collisions can be seen in figure 2.4 (a) for the W boson, and in figure 2.4 (b) for the Z boson.

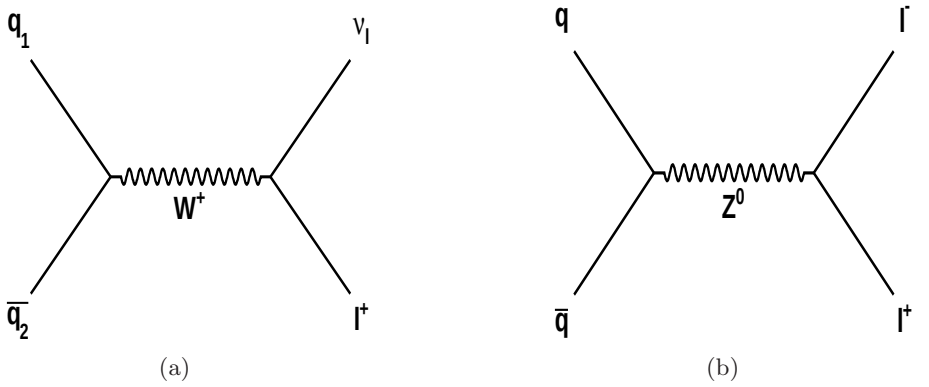

Figure 2.4: Leading order Feynman diagrams of the Standard Model W (a) and Z (b) boson production, and the decay into a lepton-antilepton pair.

If an interaction as shown in figure 2.4 takes place, the interacting protons lose in the interaction their partons, and the remnants of the protons are no longer color neutral and thus will hadronize and subsequently create jets, which will be collimated in

the directions of the initial proton remnants. In addition, the partons from the proton remnants can further interact with the partons from the other proton remnants, which leads to the creation of the so-called underlying events. A schematic view of a possible creation of the W boson in a proton-proton collision is shown in figure 2.5.

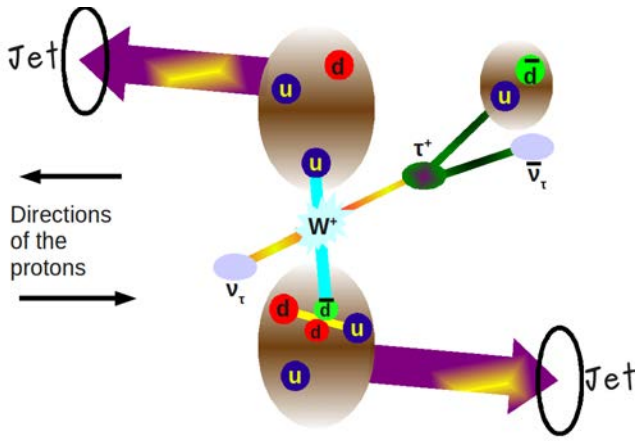

Figure 2.5: Schematic view of W^+ boson production in proton-proton collisions, with the W decaying into a tau lepton and tau neutrino, and with the following decay of the tau lepton. The yellow line between the quarks in the lower proton illustrates a gluon exchange which includes a quark loop.

The production of W and the Z bosons can be accompanied by the production of one or more partons. The partonic cross sections of such processes are then proportional to α_s^n, where n is the number of accompanying partons. Examples of diagrams of the W/Z boson production accompanied by the production of one parton is shown in figure 2.6, and of two partons in figure 2.7. The produced partons in figures 2.6 and 2.7 will subsequently hadronize and create jet(s) and thus the figures show the typical examples of the W/Z+jet(s) production processes.

The production cross sections of various processes in proton-proton (and proton-antiproton) collisions as a function of $\sqrt{s}$ is shown in figure 2.8. The total cross section is the sum of the cross sections of all processes that occurred due to the interaction of the colliding protons (proton-antiproton). In the figure we can see that the cross sections of e.g. Higgs boson production at $\sqrt{s} = 7$ TeV is roughly 10 orders of magnitude smaller than the total cross section, and e.g. the production of the Z boson is $\sim$6 orders of magnitude smaller than the total cross section. It therefore becomes clear, that in order

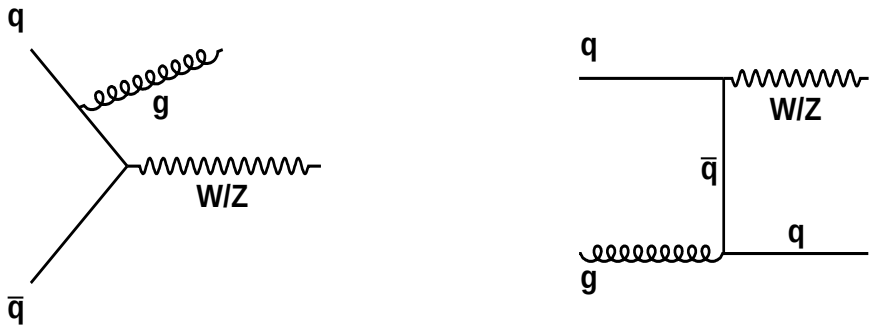

(a) (b)

Figure 2.6: Standard Model W or Z boson production with gluon initial state radiation (a) and vector boson production via quark gluon fusion (b).

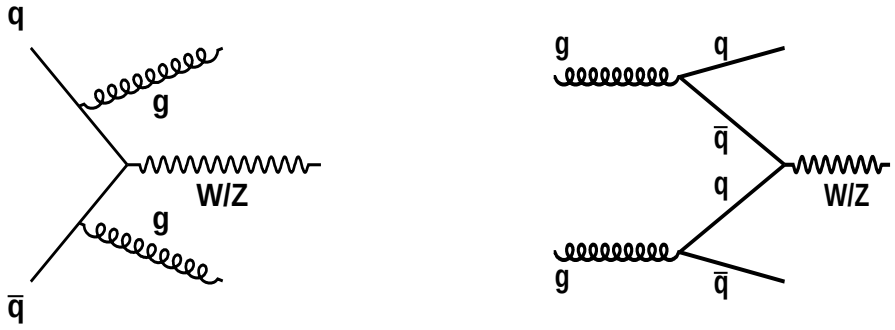

(a) (b)

Figure 2.7: Examples of Standard Model W or Z boson production with two accompanying partons. Gluon initial state radiation (a) and vector boson production via gluon-gluon fusion (b).

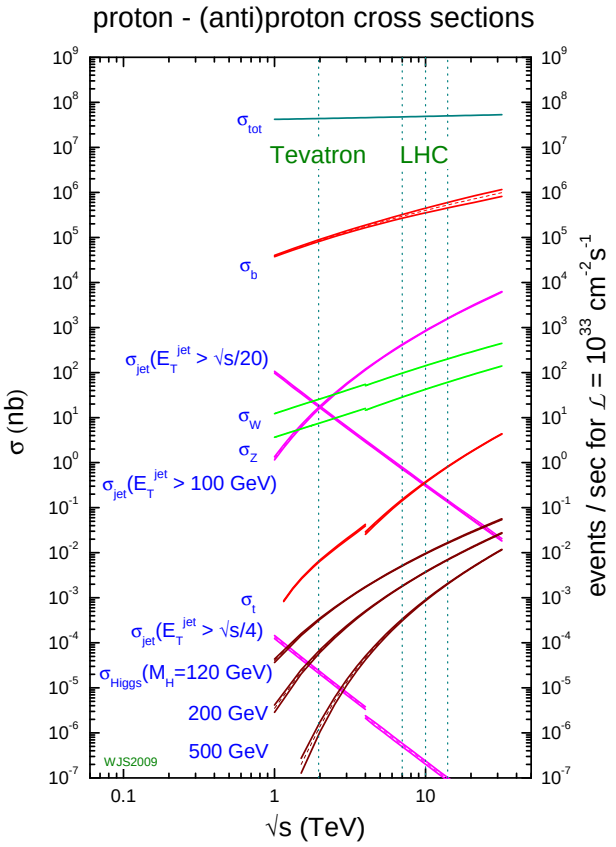

Figure 2.8: Cross sections of physics processes as functions of the center-of-mass energy $\sqrt{s}$. The vertical lines show the energies of the LHC and the Tevatron (which is a proton-antiproton collider). The gaps in the lines are due to the difference in cross sections for the proton-proton and for proton-antiproton collisions. (13).

to obtain statistically significant amount of events in which e.g. the Higgs boson could be produced, powerful accelerators that are able to achieve high luminosities at high center-of-mass energies, are needed. Such an accelerator will be described in chapter 3.

2.1.4 Status of the Standard Model

All experimental data we have are consistent with the Standard Model. Precision measurements of some Standard Model observables were done by various experiments (including CDF, DØ, LEP1, LEP2, BaBar, CLEO, Belle and others) and the results in comparison with the Standard Model predictions are shown in figure 2.9. The measurements included many Standard Model observables, and in all cases we saw

a good agreement in the measured values and the Standard Model fit to this data.

Figure 2.9: Comparison between the measurements of various Standard Model observables and the results from the global electroweak fit (15) (16).

Other confirmation of the Standard Model comes from measuring the inclusive jet production cross sections that are studied in hadron induced processes, in p-p, p-$\overline{p}$ and e-p collisions. The combined plot of comparisons of data and the theoretical predictions of the inclusive cross sections as functions of jet transverse momentum is shown in figure 2.10. In most cases the agreement of the theory and the data is within 1σ deviation.

Despite the success of the Standard Model a key part of the theory, the Higgs boson, hasn't been discovered yet. To preserve unitarity and to avoid divergences due to the scale dependent self-coupling of the Higgs field, it is required that the mass of the Higgs is smaller than $\sim$0.8 TeV/c^2 (14). The Higgs boson has been intensively searched for and in 2011 the LHC Experiments ATLAS and CMS announced an observation of

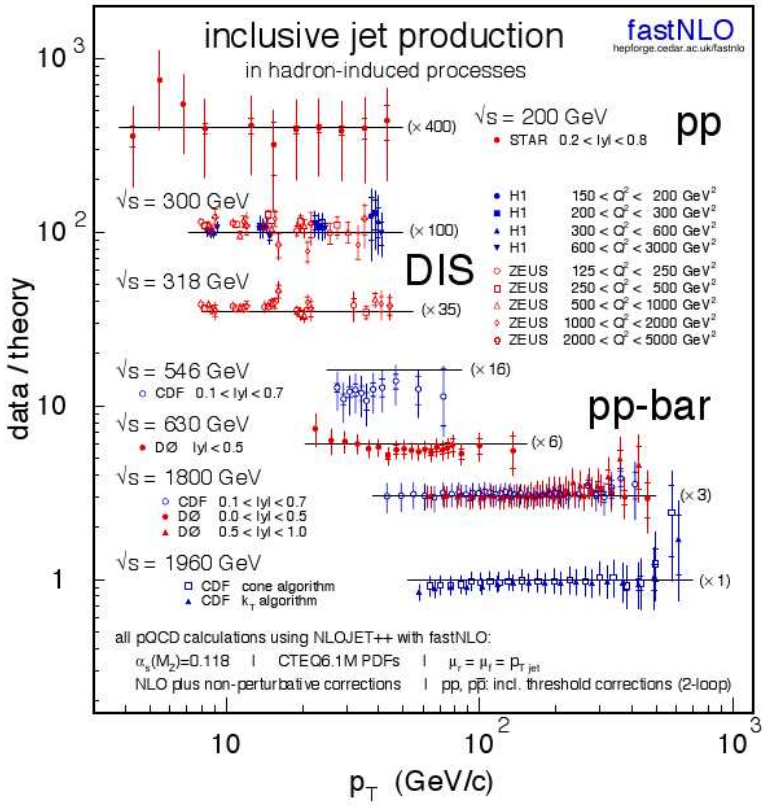

Figure 2.10: Data over theory ratios of the inclusive jet cross sections as functions of the transverse momentum of the jet, measured in different hadron-induced processes in various experiments. For a better readability of the plot, the ratios are scaled by arbitrary numbers indicated between the parentheses (17).

event excesses above their background-only hypotheses, with local significance of 3.5 standard deviations (σ) at $M_H \approx 126$ GeV in ATLAS (18), as shown in figure 2.11, and 3.1σ at $M_H \approx 124$ GeV in CMS (19). Yet, by the time of writing these lines, the significance of this signal was still not sufficient to claim a discovery of the Higgs boson.

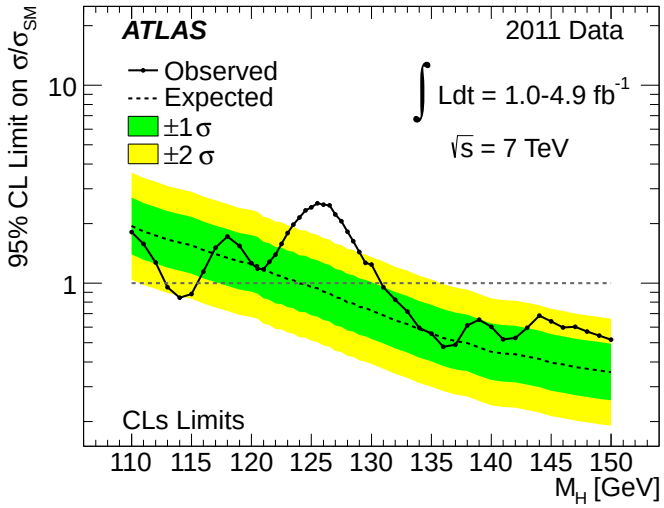

Figure 2.11: The combined 95% CL upper limits on the signal strength as a function of M_H; the solid curve indicates the observed limit and the dotted curve illustrates the median expected limit in the absence of a signal together with the 1σ (green) and 2σ (yellow) bands. These 95% CL limits use the profile likelihood technique and the CLs prescription (18).

2.1.5 Motivation of physics beyond the Standard Model

Although the Standard Model is a very successful theory, it does not describe everything in the nature. The Standard Model doesn't say anything about gravity, or phenomena such as dark matter and dark energy. Besides of this, the extrapolation of measurements of the $U(1)$, $SU(2)$ and $SU(3)$ coupling constants has shown that within the Standard Model the couplings of the fundamental forces don't cross at a common value at some common energy scale, as shown in figure 2.12 (20). This is not natural if we assume that all fundamental forces were unified in some early stage of the Universe. The inability of the Standard Model to explain these phenomena/problems leads us to the conclusion,

that there must be a more comprehensive theory beyond the Standard Model, that will be able to address these issues.

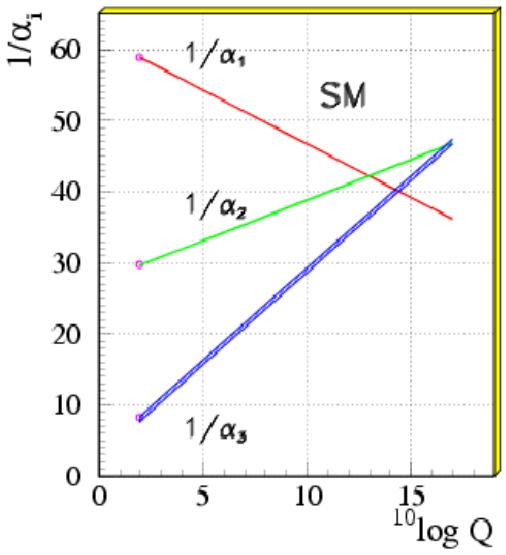

Figure 2.12: The inverted electromagnetic ($\alpha_1 = e^2/4\pi$), weak ($\alpha_2 = g^2/4\pi$) and strong ($\alpha_3 = g_s^2/4\pi$) coupling constants as a function of the logarithm of a respective energy scale Q (21).

The gravity is described by the General Relativity, which is, unlike the Standard Model, not a quantum theory. It is also unclear whether the gravitational force is a quantum force at all. A theory of quantum gravity hasn't been found yet, but a possible candidate is the Superstring theory. It is however still not clear, what observable predictions this theory provides.

At the electroweak scale ($\sim 10^2$ GeV), the gravitational force is negligible, but becomes significant for very large energy scales, such as the Planck scale (M_{Planck} $\sim 10^{19}$ GeV). It is not known why M_{Planck} is so much larger than the electroweak unification scale. This large difference in the fundamental scales is called the Hierarchy problem. A possible solution to the Hierarchy problem could be provided by models with large extra dimensions (such as the ADD model (22), or the Randall-Sundrum model (23)). These models define n extra dimensions (n=1 for the Randal-Sundrum model and $n \geq$2 for the ADD model), and the so-called "branes". While the fields of the Standard Model exist only on the brane, corresponding to our 4D space-time,

the gravity is distributed in the full (4+n)D space-time and therefore appears weaker in comparison to the fields, which are concentrated on the brane. Using a suitable parametrization of these models, the Planck energy scale on the brane can be reduced to $\sim \mathcal{O}$(TeV), which would provide a solution of the Hierarchy problem. Moreover, the Hierarchy problem has an affect on the theoretical prediction of the Higgs mass, M_H, which receives corrections from one-loop diagrams proportional to $\mathcal{O}(\Lambda)$, where Λ is the next higher scale in the theory (2). In case the scale $\Lambda = M_{Planck}$ the corrections to M_H would be unnaturally large, unless no unnatural fine-tunings are done.

A different approach to the solution of the Hierarchy problem could provide models within the Supersymmetry (SUSY) framework (24). SUSY introduces new "super-partners" to the Standard Model particles, whose contributions in the additional loop diagrams, particle by particle, cancel the divergent corrections to M_H. The spin of the SUSY superpartners is shifted by 1/2 w.r.t. their Standard Model partners. The SUSY models predict sleptons and squarks (SUSY partners to the leptons and quarks) with spin 0, and gluino, wino, photino, bino and charged and neutral higgsinos[1] with spin 1/2, which are the superpartners to the gauge fields. In some SUSY models the lightest SUSY particle is stable, massive and weakly interacting, and thus can provide a candidate particle for the Dark Matter. In addition, it has been shown that the minimal supersymmetric extension of the Standard Model leads to the unification of the strong and electroweak forces at the scale approximately 10^{16} GeV (20).

Other theories such as those based on the SO(10) symmetry (25) can also provide the unification of the fundamental forces of the Standard Model. These symmetries are broken at the GUT scale and can involve the existence of exotic particles such as leptoquarks. The leptoquarks are hypothetical particles that decay into leptons and quarks, and could be produced in processes such as $g + g \rightarrow LQ + \overline{LQ}$, or $q + \overline{q} \rightarrow LQ + \overline{LQ}$. The leptoquarks are distinguished as 1^{st}, 2^{nd} or 3^{rd} generation leptoquarks, and decay exclusively in 1^{st} (e.g. electron and down quark), 2^{nd} (e.g. muon and strange quark) or 3^{rd} (e.g. tau and bottom quark) leptons and quarks (4).

For every good physics model that aims to solve any of the mentioned fundamental problems it is important that it provides predictions that can be tested in experiments. Many theories predicting physics beyond Standard Model predict the existence of new

[1] The SUSY requires also at least 5 different higgs fields: h^0, A^0, $H^{\pm}$ and the Standard Model H^0, and for each of them their superpartners.

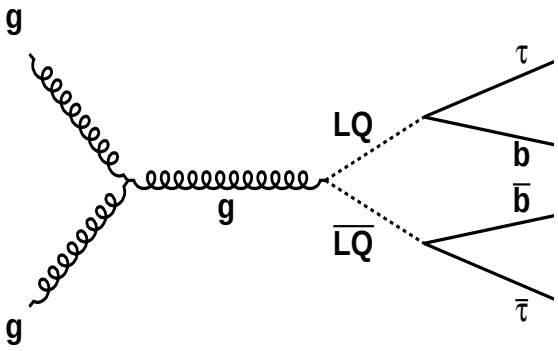

Figure 2.13: A diagram of the 3^{rd} generation leptoquark production with two τ's and two b quarks/jets in the final state.

particles that could be produced in high energy collisions. Most of these particles are short-lived and can be observed only through their decay products.

One of the promising signatures is the decay of an exotic particle that preferentially couples to the 3^{rd} generation lepton, the tau lepton. Besides of the advantage of the enhanced coupling to the tau lepton, in various SUSY models the mass of the 3^{rd} generation scalar quark (which decays into the 3^{rd} generation Standard Model particles) can be relatively light (26), which would favour the production of such particles in particle colliders even at relatively low center-of-mass energies. The tau lepton therefore plays an important role in the searches of the signs of physics beyond the Standard Model. The importance of studies that include the production of τ leptons has been acknowledged in many searches of possible exotic particles such as described in the studies (4), (26), (27), (28) or in the search of the mentioned third generation leptoquarks (29), whose possible production and decay scheme is illustrated in figure 2.13.

2.2 Tau lepton

The tau lepton, τ, was the first observed 3^{rd} generation particle. The τ was discovered at SLAC, in a series of experiments between 1974-1977 by Martin Lewis Perl[1] (30). The τ is the heaviest of the leptons, with the mass $m_\tau = 1.777$ GeV (4). It can be produced in the decays of e.g. the W and the Z bosons, and in case of the existence of the Higgs boson, also in the process of $H \rightarrow \tau^+\tau^-$, which has the second largest branching ratio of all Higgs boson decays in case $M_H < 120$ GeV.

[1]Nobel Prize in physics 1995

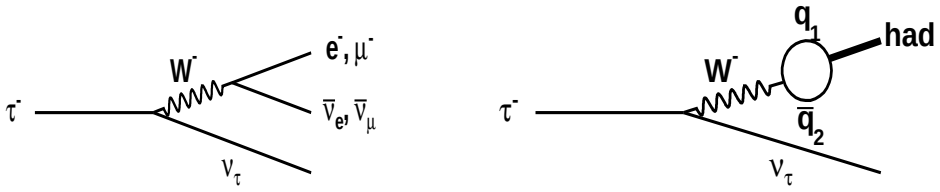

Figure 2.14: Diagrams of the leptonic decay (a) and the hadronic decay (b) of the τ lepton.

The τ is an unstable particle with a lifetime of 290.6 fs. It can decay into a lighter lepton (electron or muon) and two neutrinos[1], and with its mass it is the only lepton that is kinematically allowed to decay also into hadrons. We therefore distinguish leptonic and hadronic τ decays. The diagrams of the τ decays are shown in figure 2.14.

The hadronization of the quarks in the hadronic decays is dominated by resonance production (31), (32). A summary of the τ decay modes is shown in table 2.2. Without the radiative corrections, the expected branching ratios of both lepton decay channels would be 20 %. In the hadronic decay modes, the charged $\rho^{\pm}$ meson decays into a charged $\pi^{\pm}$ and one neutral π^0 which decays promptly to two γ's. The final states with the combination of three or more hadrons go through the creation and decay of the a_1 resonance. The $\pi^{\pm}$ and $K^{\pm}$ mesons have a lifetime ct (where c is the speed of light and t is the mean lifetime) of $\sim$10 m, and are therefore in detector physics considered as stable.

2.3 Monte Carlo models

In order to simulate physics processes that occur in the collisions of particles, Monte Carlo methods are used. This simulation is often done by using the so-called Monte Carlo generators. Based on theoretical models, in the simulation of proton-proton

[1]Due to the CP invariance and for simplicity reasons, τ^- will be considered in this thesis as identical to its anti-particle τ^+ as they have the same lifetime, same mass and the same decay modes (except the particles are replaced by their anti-particles). In the whole thesis under τ is meant both τ^+ and τ^-, and when discussing the τ decays the terminology of a τ^- decay is used. Also, to keep the terminology simple, neutrinos (ν's) will be in this thesis also identical to the anti-neutrinos ($\bar{\nu}$'s) and not distinguished by their types (electron, muon, tau), unless explicitly specified.

τ^- decay mode	BR %
$\tau^- \to e^- \bar{\nu}_e \nu_\tau$	17.85
$\tau^- \to \mu^- \bar{\nu}_\mu \nu_\tau$	17.36
$\tau^- \to \pi^- \nu_\tau$	10.91
$\tau^- \to K^- \nu_\tau$	0.67
$\tau^- \to \rho^- \nu_\tau$	25.95
$\tau^- \to K^{*-} \nu_\tau$	1.43
$\tau^- \to h^- 2\pi^0 \nu_\tau$	9.49
$\tau^- \to h^- 3\pi^0 \nu_\tau$	1.17
$\tau^- \to h^- h^- h^+ \nu_\tau$	9.80
$\tau^- \to h^- h^- h^+ \pi^0 \nu_\tau$	5.38

Table 2.2: Main branching fractions of the τ. The $h^\pm$ stands for $\pi^\pm$ or $K^\pm$ meson (4).

collisions, the Monte Carlo generators are used to describe hard and soft interactions of the colliding partons, production (and a possible decay) of the particles, and the hadronization of particles with color. In the scope of this work, the most interesting Monte Carlo generators are: `Pythia`, `Alpgen`, `Herwig`, `MC@NLO` and `Tauola`.

`Pythia` (33) is a general purpose generator, providing simulations of proton-proton (parton-parton) interactions at the lowest order, in Born-level approximation. Higher order processes are approximated by a parton shower approach, which parametrizes any "$2 \to n$" process into a "$2 \to 2 \oplus \mathrm{ISR} \oplus \mathrm{FSR}$" process, where ISR (FSR) stands for the initial (final) state radiation of the incoming (outgoing) partons. The hadronization of particles with a color charge is done in a phenomenological way, using the so-called Lund String Model. In the Lund String Model, the potential energy between two partons is represented by a color-string, and increases linearly with the distance of the two partons. If the potential energy stored in the color-string exceeds the energy needed to create a quark-antiquark pair, the color-string breaks, and a new quark-antiquark pair is created. Two new color-strings are then created between the newly created quark-antiquark and the initial partons. This continues until the energy stored in the color-string is not sufficient to create another on-mass-shell quark-antiquark pair. In the last step, the partons connected via a color-string are bound into colorless hadrons.

`Alpgen` (34) generator performs at the leading order the calculations of the exact matrix elements for a large set of parton-level processes, including final states of leptonic W and Z boson decays, accompanied with up to six jets. Therefore, in particular for a

production processes of W and Z boson in association with one or more jets, the `Alpgen` predictions are widely used. To provide the hadronization, `Alpgen` is interfaced with the `Herwig` (35) generator. The hadronization using `Herwig` is done by the so-called cluster hadronization model. In the cluster hadronization model, first the produced gluons are split in quark-antiquark pairs, and the neighbouring quark-antiquark pairs are combined into massive color singlet clusters. If allowed by the phase space, the clusters can decay into smaller clusters, or decay into hadrons by recombining with a new quark-antiquark pair created out of the vacuum.

`MC@NLO` (36) generator includes in the computation of hard partonic processes the full Next-to-Leading-Order QCD corrections. It is particularly useful when hard p_T QCD emissions need to be calculated exactly, in agreement with the result of the Next-to-Leading-Order matrix element. The `MC@NLO` generator is interfaced with `Herwig` to provide the hadronization of the partons.

`Tauola` (37) is used to simulate the decays of the τ's, taking into account the τ polarization, which is not included in the general purpose generators. It is interfaced with `Pythia`, `Alpgen` and `MC@NLO` in processes, which include the production of the τ's.

3

Experimental Situation

3.1 The Large Hadron Collider

The Large Hadron Collider (38), LHC, is currently the largest particle accelerator in the world. It is built at CERN, at the border between France and Switzerland, roughly 50-170 m under ground in the former LEP tunnel, 26.7 km long. It is a synchrotron based accelerator that has been designed to collide two oppositely rotating proton beams, at the centre of mass energy $\sqrt{s} = 14$ TeV. Although, in the initial face the LHC is operating at $\sqrt{s} = 7$ TeV. In addition, the LHC is capable to provide also heavy ion collisions (lead on lead collisions) at $\sqrt{s} = 2.76$ TeV per nucleon. A proton beam can consist of up to 2808 bunches, and each bunch can consist of up to 1.1×10^{11} protons. The designed bunch crossing rate is 40 MHz.

The acceleration of the protons is done in several steps. After injecting the protons from a linear accelerator (LINACS2) into the PS booster, they are injected into the Proton Synchrotron (PS). Here the protons are accelerated to the energies of 25 GeV. From PS the protons are redirected to the SPS, where they are accelerated to 450 GeV. The final acceleration is done by the LHC, to the final collision energy $\sqrt{s} = 7$ TeV. A schematic view of the LHC accelerator complex is illustrated in figure 3.1.

The LHC consists of 1232 dipole magnets with the length of 15 m, 392 quadrupole magnets with 5-7m length, and a variety of different other magnet types (sextupoles, octupoles) of various sizes. The schematic view of the dipole magnet is shown in figure 3.2.

The dipole magnets are designed to generate a magnetic field with the strength

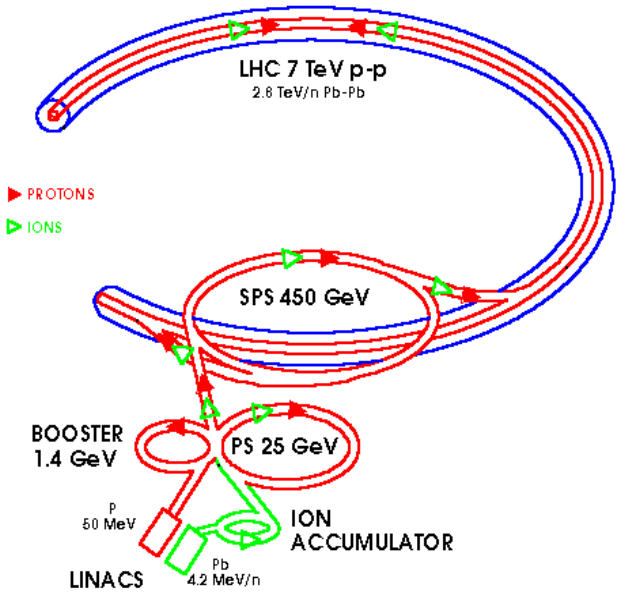

Figure 3.1: Schematic view of the LHC with the supporting SPS and PS accelerators (38).

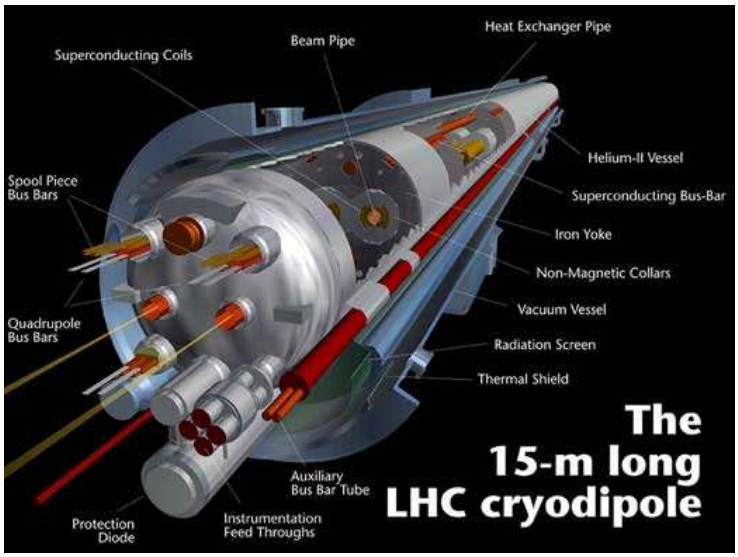

Figure 3.2: A schematic picture of one of the 1232 dipole magnets at LHC (39).

of 8.33 Tesla. To be able to achieve a magnetic field of this strength, a current of 11.8 kA is needed. Such a high current can be achieved by using superconducting materials in a cryogenic temperature environment. This is achieved by using liquid helium cooling at an operating temperature of 1.9 K. The energy stored in one dipole magnet under such conditions is roughly 8.1 MJ. This energy is large enough to destroy a magnet. Therefore a quenching protection system is used to redirect the energy from the magnets, in case of unexpected events connected with a quench of one or more magnets would occur.

To minimize the energy losses of the accelerated protons due to the interaction with gas in the beam pipe, high requirements on the vacuum in the beam pipes are requested. Therefore, the beam pipe is evacuated to a gas pressure of 10^{-10} to 10^{-11} mbar.

The collisions of the accelerated protons (ions) take place at four interaction points, where the beams cross. The four main experiments: **ALICE**, **ATLAS**, **CMS** and **LHCb**, are installed around these interaction points. While the ALICE experiment is specialized in heavy ion physics, and the LHCb is specialized in studying the physics of b-quark system, the general purpose experiments, that aim to explore a broad range of possibly physics outcomes from the LHC, are ATLAS and CMS.

The luminosity delivered to the experiments at the interaction points can be expressed as:

$$\mathcal{L} = \frac{N_b^2 n_b f_{Rev} \gamma_r}{4\pi \epsilon_n \beta^*} F, \tag{3.1}$$

where N_b is the number of particles per bunch, n_b the number of bunches in the beam, f_{Rev} the revolution frequency, γ_r the relativistic gamma factor, ϵ_n the normalized transverse beam emitance, β^* the beta function at the interaction point, and F the geometric luminosity reduction factor. During the 2011 running, the maximal instantaneous luminosity delivered by the LHC changed significantly. Figure 3.3 shows the maximal instantaneous luminosity of the LHC in the timescale of the 2011 data taking. Here we can see how the performance of the LHC improved, providing approximately factor 10 increase in the instantaneous luminosity since spring until summer 2011. The designed instantaneous luminosity is 10^{34} cm^{-2}s^{-1}.

The number of collisions is proportional to the luminosity integrated over time,

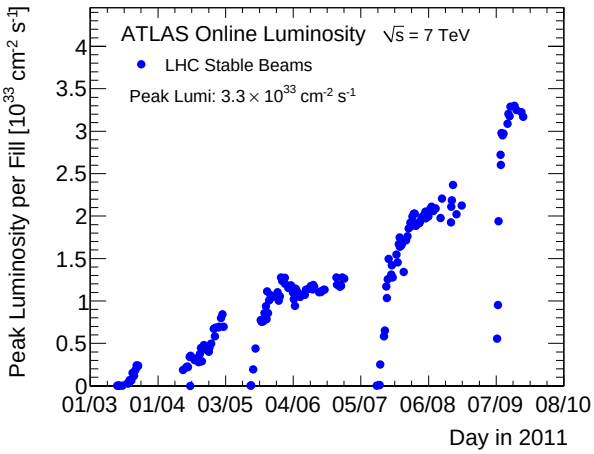

Figure 3.3: Maximal instantaneous luminosity during the 2011 data taking delivered to the ATLAS experiment (40).

$\mathcal{L}_{\text{int}}$. The integrated luminosity per single LHC run can be expressed as:

$$\mathcal{L}_{\text{int}} = \mathcal{L}_0 \tau_L [1 - e^{-T_{run}/\tau_L}], \tag{3.2}$$

where $\mathcal{L}_0$ is the initial maximal luminosity, T_{run} is the length of the run in hours, and τ_L is the luminosity lifetime. The luminosity lifetime based on calculations is $\tau_L = 14.9$ h (38), though in practice this number can fluctuate between $\tau_L = 5$ h to $\tau_L = 20$ h (41). The total integrated luminosity, which is the sum of the per-run integrated luminosities, in the period of the spring and summer 2011 LHC data taking, is shown in figure 3.4.

In proton-proton collisions at the LHC, an overwhelming majority of events is low p_{T} scattering of the colliding protons, referred to as the minimum bias events. In order to increase the LHC luminosity, proton beams are adjusted so that up to 25 proton-proton interactions per bunch crossing take place. Thus for every "interesting" collision in which a possible exotic particle is produced, we have up to 24 minimum bias events in the same bunch crossing. These events are the main part of the so-called pile-up. Besides of the minimum bias events, the contribution to the pile-up accounts also for the interaction of the protons with the residual gas in the beam pipe, and the background from the activated material around the interaction point. An event display

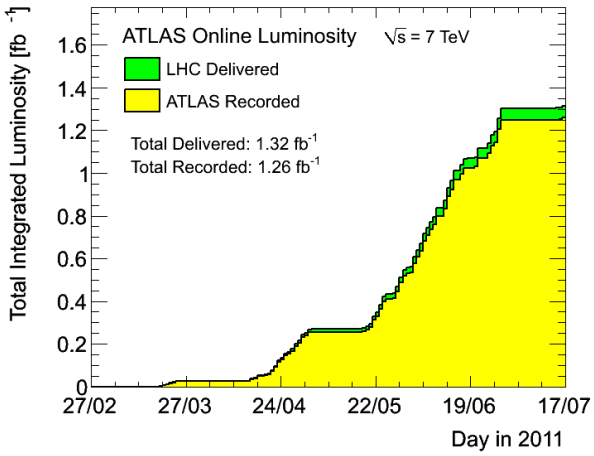

Figure 3.4: Total integrated luminosity since March 13 until July 17 2011 for the delivered luminosity by the LHC (green) and the recorded luminosity by the ATLAS detector (yellow) (40).

of a beam crossing with four minimum bias events, as seen by the ATLAS detector, can be seen in figure 3.5.

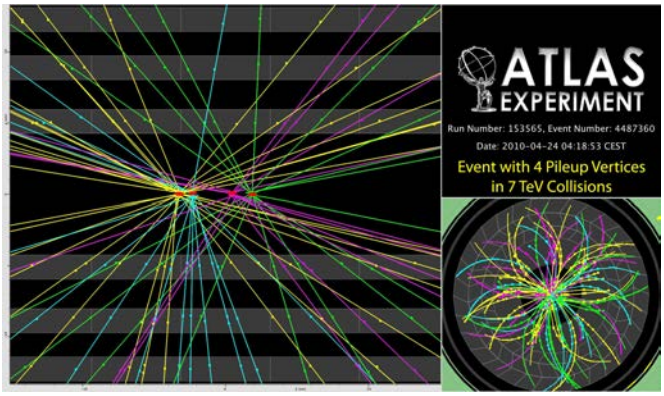

Figure 3.5: Real data event with four primary proton-proton collisions in the same beam crossing (42).

3.2 The ATLAS Detector

The ATLAS (A Toroidal LHC Apparatus) detector (43) is located at the Swiss-French border at the Meyrin site of the LHC, about 100m under ground. It has a cylindrical

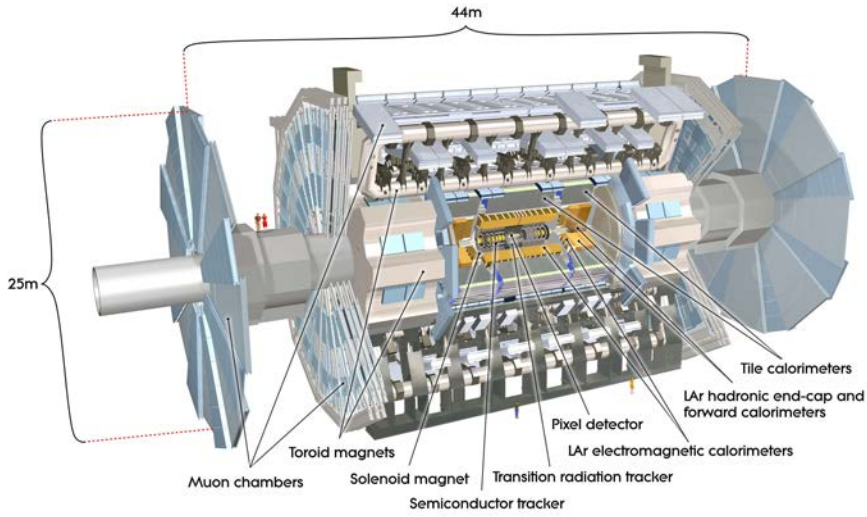

Figure 3.6: A picture of the ATLAS detector including an overview of the detector's sub parts.

shape with the height of 25 m and a length of 44 m, as seen from the figure 3.6. It consists of four major parts: Inner detector, Calorimeter, Muon spectrometer and a System of Magnets.

The ATLAS detector is designed to identify and precisely measure the momentum and the energy of all final state particles. Electrons and photons deposit their full energy early in the calorimeter, in what is referred to as the electromagnetic calorimeter, while the hadrons deposit most of their energy later, in what is referred to as the hadron calorimeter. Charged particles trajectories are measured by the inner detector, which is located inside of a strong magnetic field for a precise momentum measurement. Muons are highly penetrating. They are identified by their signal in the muon spectrometer, and their momenta is estimated by combining the information from the muon spectrometer and the inner detector. Neutrinos have a very low probability of interaction with matter and escape from the interaction point undetected. Their presence can be deduced from the im-balance in the energy of the particles in the plane transverse to the beam direction, and using the fact, that the ATLAS detector is almost hermetic. A schematic view of the signatures of the different final state particles in the ATLAS detector is shown in figure 3.7.

The ATLAS detector, in order to be sensitive in large variety of physics phenom-

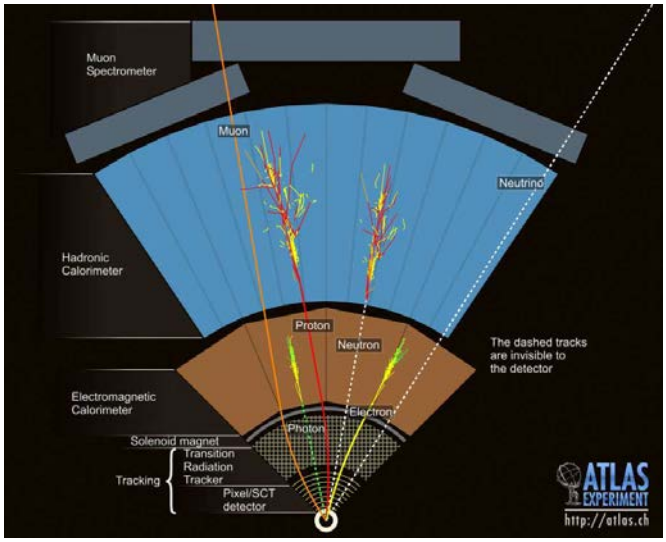

Figure 3.7: An intersection of the ATLAS detector with the typical signatures of different final state particles.

ena, has been designed to have high momentum and energy resolution. The required resolution of the ATLAS detector is shown in the table 3.1.

Subsystem	Required resolution
Inner detector	$\sigma_{p_T}/p_T = 0.05\% p_T \oplus 1\%$
EM Calorimeter	$\sigma_E/E = 10\%/\sqrt{E} \oplus 0.7\%$
Had Calorimeter (barrel, end cap)	$\sigma_E/E = 50\%/\sqrt{E} \oplus 3\%$
Had Calorimeter (forward)	$\sigma_E/E = 100\%/\sqrt{E} \oplus 10\%$
Muon Spectrometer	$\sigma_{p_T}/p_T = 10\%$ at $p_T = 1TeV$

Table 3.1: The required resolution of the ATLAS detector. The units of p_T and E are in GeV (43).

3.2.1 ATLAS coordinate system

The origin of the ATLAS coordinate system is at the nominal interaction point. The z axis is defined by the direction of the beam. The positive x axis points to the center of the LHC ring and the positive y axis is pointing upwards. In the cylindrical geometry of the ATLAS detector it useful to define the azimuthal angle $\phi = \texttt{arctan}(x/y)$, measured around the beam axis, and the polar angle θ measured from the beam axis,

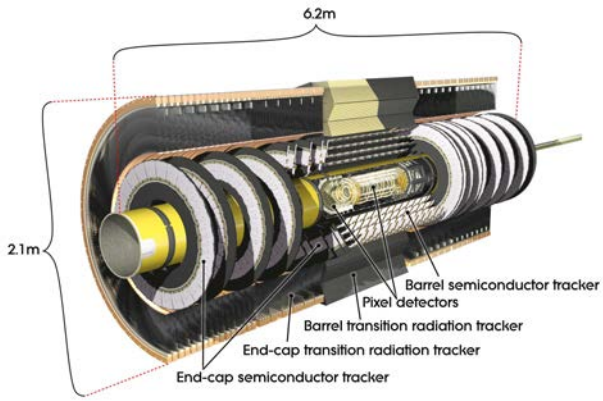

Figure 3.8: A view of the ATLAS inner detector.

as $\theta = \texttt{arccot}(z/\sqrt{x^2+y^2})$. It is also useful to define the pseudorapidity η, where $\eta = -\ln \texttt{tan}(\theta/2)$. In this work the coordinate system will be most often defined by the η, ϕ and z coordinates. In this system it is useful to define the distance ΔR, which is the distance in the pseudorapidity-azimuthal angle space, defined as $\Delta R = \sqrt{\eta^2 + \phi^2}$. The spatial coverage of the detector in ϕ is 2π, and in η is up to $|\eta| = 4.9$ in the forward calorimeter (43).

3.2.2 Inner detector

The inner detector (ID) is an important part of the ATLAS detector, specialized in the momentum measurement of charged particles (tracks), providing a good momentum resolution, pattern recognition and primary and secondary vertex measurement. The ID is the innermost part of the ATLAS detector. It is placed in a 2 Tesla magnetic field and consists of 3 sub parts: Pixel detector, SCT detector and Transition Radiation Tracker (TRT), as shown in figure 3.8.

The detector closest to the beam pipe is the high-resolution Pixel detector, followed by the SCT detector. Both detectors have an η coverage of $|\eta| < 2.5$. The outermost part is the TRT. The TRT provides an enhancement of the pattern recognition, and improves the momentum resolution over $|\eta| < 2.0$.

The Pixel detector and the SCT detector are high precision semiconductor detectors based on silicon technology. The TRT is composed of multiple straw detectors and uses

the fact that a relativistic charged particle, when passing from one medium to another with different dielectric permittivity, produces transition radiation.

The Pixel detector consist of 3 cylindrical layers in the barrel region and 6 layers in the end-cap region (three on both sides) as shown in Figure 3.9, with the first layer often referred to as the B-layer[1]. There are 1744 pixel sensors with the size 19×63 mm^2 in the detector. The minimal pixel size in the pixel sensors is $R - \phi \times z = 50{\times}400\ \mu\text{m}^2$, where R is the radius orthogonal to the beam axis. The pixel detector has approximately 80 million read-out channels.

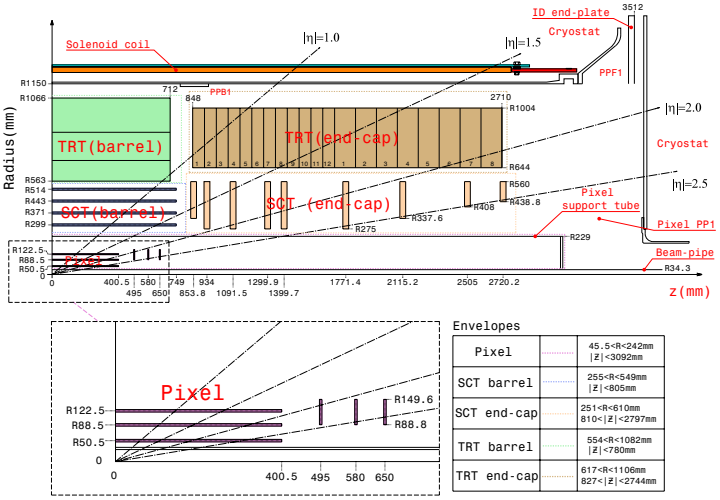

Figure 3.9: Scheme of the ATLAS inner detector with the description of the barrel and the end-cap regions of each inner detector subpart.

The SCT detector consists of 4088 modules with four coaxial double sided layers in the barrel region and 18 end-cap double sided layers (9 at each side). Every module consist of 2×768 active silicon strips with stereo rotation. In total there can be 8 measurements (hits) per one track in the SCT detector. The SCT contains over 6.2 million read-out channels.

The TRT consists of polyimide drift (straw) tubes of 4 mm diameter placed in 73 layers, interleaved by polypropylene fibers in the barrel region, and 320 straw planes (160 at each side) interleaved by polypropylene foils in the end-cap region. The 19 μm thick fibers and 15 μm thick foils provide the transition radiation.

[1] "B"-layer because of the importance of the first pixel layer in B tagging.

In the barrel region, the straw tubes with the length of 144 cm are parallel to the beam axis, while in the end-cap 37 cm long straws are grouped in disks orthogonal to the beam axis. The typical number of hits per track is 36. The TRT is designed to have a turn-on of the transition radiation for the Lorentz boost factor γ between 10^3 and 10^4. Due to the fact that electrons are much lighter than charged pions, at a given momentum, γ is higher for electrons than for the pions. This provides an effective separation between charged pions and electrons, for energy range 2-350 GeV(43). The number of TRT read-out channels is ∼350k.

3.2.3 Calorimeter

For measuring the energies of the final state particles, calorimeters are used. The ATLAS calorimeter is divided in two basic parts: Electromagnetic calorimeter (EM) and Hadron calorimeter (Had). The electromagnetic calorimeter is used to precisely measure the energies of electrons and photons, while the Hadronic calorimeter is used for measuring the energies of hadrons. A schematic view of the ATLAS calorimeter with all parts can be seen in the figure 3.10.

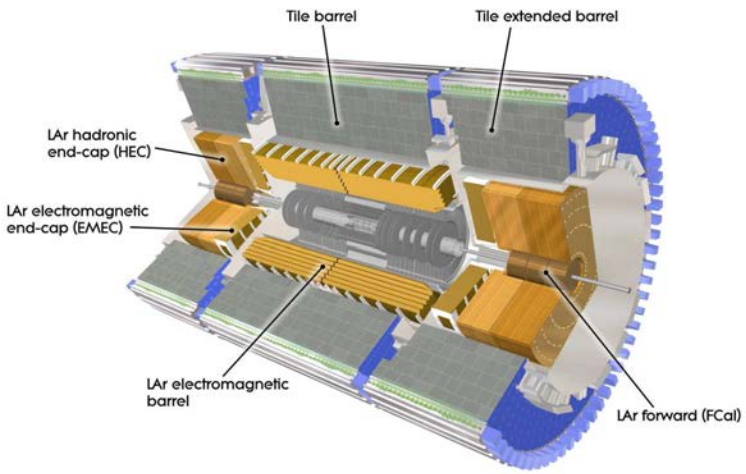

Figure 3.10: A schematic view of the ATLAS calorimeter.

The EM calorimeter is divided into a barrel part at $|\eta| < 1.475$, and an end-cap (EMEC) part at $1.375 < |\eta| < 3.2$. An important parameter for the calorimeter is its thickness. The total thickness of the EM calorimeter is greater than 22 radiation

lengths (X_0) in the barrel and greater than 24 X_0 in the end-cap. The active material of the EM calorimeter is liquid argon (LAr) with lead as the absorber. In the EM calorimeter, an accordion shaped geometry of the absorber, interleaved with red-out electronics has been chosen (see figure 3.11). The advantage of such accordion geometry is, that it provides a full coverage in ϕ and a fast read out (43).

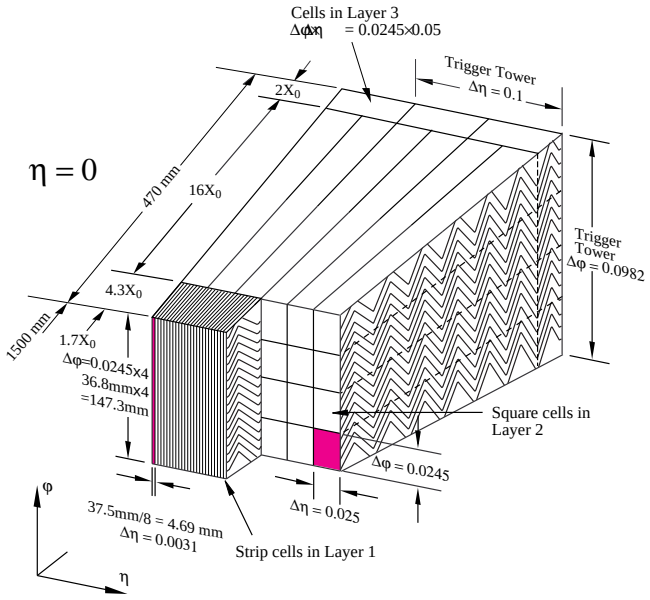

Figure 3.11: A schematic picture of the LAr calorimeter with the cell geometry.

A presampler in $|\eta| < 1.8$ is used to correct radiation losses of particles, caused by material in front of the EM calorimeter.

The fine granularity of the EM calorimeter allows precision measurements of electrons and photons. The first layer of the barrel calorimeter (the strip layer) with the thickness of 4.3 X_0 is arranged in very fine readout strips in η, which provide a good separation of photon pairs from π^0 decays and isolated photons. The granularity in most of the barrel region is $\Delta\eta \times \Delta\phi = 0.025/8{\times}0.1$ and in the end-cap region varies between $\Delta\eta \times \Delta\phi = 0.025/8{\times}0.1$ up to $\Delta\eta \times \Delta\phi = 0.1{\times}0.1$.

The second layer has the highest thickness, 16 X_0, and absorbs the largest fraction of the electromagnetic energy. It has the granularity $\Delta\eta \times \Delta\phi = 0.025{\times}0.025$ in most of the barrel region and between $0.025{\times}0.025$ and $0.1{\times}0.1$ in the end-cap region. This allows a precise measurement of the shower shape of the energy deposit, and thus

differentiate between energy deposits of electromagnetic and hadronic origin.

The third EM calorimeter layer has the function of an additional absorber of the electromagnetic energy, that has passed through the first two layers. Depending on η it is between 2 X_0 and 10 X_0 thick, it has the granularity of $\Delta\eta \times \Delta\phi = 0.050 \times 0.025$, and covers the η region of $|\eta| < 2.5$.

The Had calorimeter is divided in the Tile calorimeter (central region $|\eta| < 1.7$), hadronic end-cap calorimeters (HEC, $1.5 < |\eta| < 3.2$) and forward calorimeters (FCal, $3.1 < |\eta| < 4.9$). While in the Tile calorimeter scintillating tiles and high purity steel as an absorber are used, in HEC and FCal, liquid argon is used as the active medium, and Copper (HEC and FCal1) and Tungsten (FCal2, FCal3) are used as absorbers.

The Tile calorimeter is additionally divided in one central barrel $|\eta| < 1.0$ and two extended barrel sections in $0.8 < |\eta| < 1.7$. It consist of 3 layers and the total detector thickness at the outer edge of the tile region is 9.7 interaction lengths. Figure 3.12 shows a schematic intersection of the Tile calorimeter. On the picture we can see how the scintillating tiles are integrated together with the absorbers and the photomultipliers.

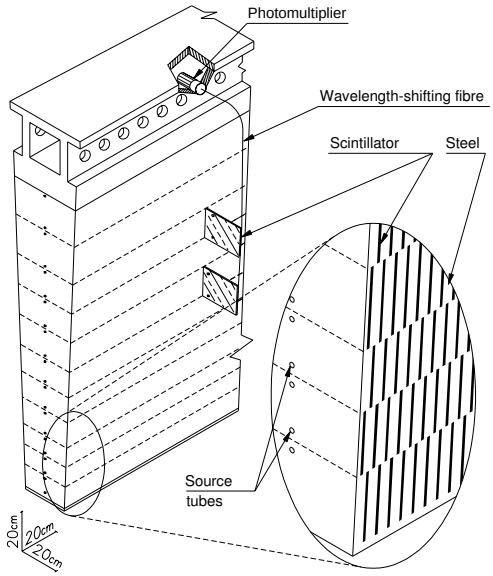

Figure 3.12: Scheme of the mechanical assembly of the Tile calorimeter (43).

The HEC consist of two copper wheels in each end-cap. The front wheels consist of 24 copper plates, each 24 mm thick, and one 12.5 mm thick front plate. The second

wheel consists of sixteen 50 mm thick plates, with one 25 mm front plate. The active medium is being shared with EMEC and FCal.

The FCal consists of three parts, FCal1, FCal2 and FCal3, and is used to increase the $|\eta|$ coverage, to be able to provide a good missing transverse energy measurement. Unlike the Fcal2 and FCal3, the first module is meant as a part of the electromagnetic calorimeter. The choice of tungsten in FCal2 and FCal3 modules as absorbers is in order to limit the longitudinal and transverse spread of hadronic showers (44). The depth of the whole FCal is around 10 interaction lengths.

The granularity of the Had calorimeter is optimised to satisfy the physics requirements for the reconstruction of jets and missing transverse energy. In HEC it is $\Delta\eta\times\Delta\phi$ = 0.1×0.1 in $1.5 < |\eta| < 2.5$ and 0.2×0.2 in the region $2.5 < |\eta| < 3.2$. In the Tile calorimeter, the granularity is $\Delta\eta \times \Delta\phi = 0.1\times0.1$ except the last layer, for which it is 0.2×0.1. In the FCAL, the granularity is given in $\Delta x \times \Delta y$ (cm) and varies between 3.0 cm × 2.6 cm to 5.4 cm × 4.7 cm.

3.2.4 Muon System

The muon system (43) is a crucial component of the ATLAS detector, that is used to identify and measure the momentum of muons. It is divided in four different tracking chambers: Monitored drift tubes (MDT), Cathode strip chambers (CSC), Resistive plate chambers (RPC) and Thin gap chambers (TGC).

The MDT covers a region of $|\eta| < 2.7$ and consists of high precision drift chambers. In the barrel region ($|\eta| < 1.05$) it consists of three cylindrical layers around the beam axis. In the end-cap and forward region at $1.05 < |\eta| < 2.7$ of two wheels perpendicular to the z axis. In total, the MDT is made of 1088 drift chambers. It has 339k read out channels. The operating gas in the MDT tubes is Ar/CO_2 (93/7) with a small fraction ($<$ 1000 ppm) of H_2O, the wire potential is 3080 V and the maximum drift time is about 700 ns.

Due to high rates in the end-cap region at $2 < |\eta| < 2.7$, the MDT is replaced by the fast CSC muon system. The CSC system is made of 32 chambers (16 on each side of the detector). Each chamber is a system of multiwire proportional chambers with a resolution of around 60 μm. The features of the CSC system are high track, time and double track resolutions, high rate capability (up to 1000 Hz/cm^2) and low neutron

sensitivity. The operating gas is Ar/CO_2 (80/20) and the operating voltage is 1900 V. The electron drift time is less than 40 ns.

The RPC and TGC are used by the trigger system for their high operational speed. The RPC is made of 544 chambers, covering the region of $|\eta| < 1.05$. A chamber is made of two plate detectors. The plate detectors consist of two resistive plates with an electric field of 4.9 kV/mm in the gap between the plates. The operating gas is $C_2H_2F_6$/Iso-C_4H_{10}/SF_6 (94.7/5/0.3). The rate capability is around 1 kHz/cm^2. The TGC covers a region of $1.05 < |\eta| < 2.4$, consist of 3588 chambers, and besides the trigger function it complements the MDT in the azimuthal angle measurement. The TGC's are multiwire proportional chambers using as operating gas a mixture of CO_2 and n-pentane (55/45), with a wire potential of 2900 $\pm$ 100 V. The operational speed of the TGC's is around 25 ns.

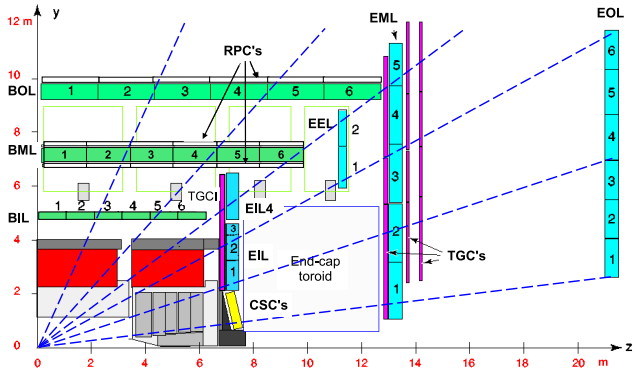

Figure 3.13: The ATLAS Muon system (43).

3.2.5 System of Magnets

An important part of the ATLAS tracking and muon system is the system of magnets (43). It consists of four superconducting magnets, one solenoid magnet which surrounds the inner detector, and three toroid magnets which are crucial for the muon spectrometry. The solenoid provides an axial magnetic field of 2 T, while the toroid magnets, consisting of one barrel toroid ($|\eta| < 1.4$) and two end-cap toroids ($1.6 < |\eta| < 2.7$), provide a magnetic field of 0.5-1 T. The ATLAS magnetic system provides the magnetic field over the volume of approximately 12,000 m^3.

The geometry of the ATLAS magnetic system is shown in figure 3.14. Each of the toroid magnets is composed of eight toroid coils encased in vacuum vessels.

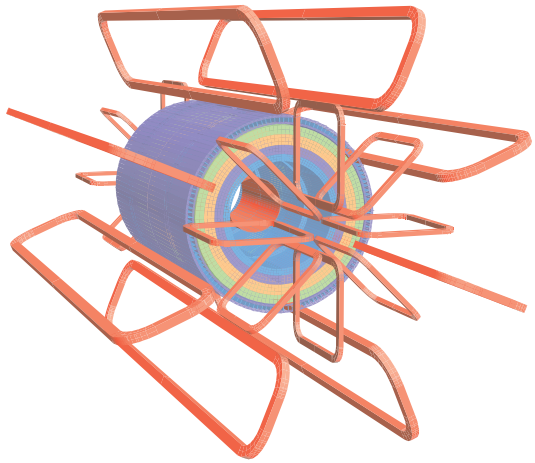

Figure 3.14: The scheme of the system of magnets. The solenoid magnet in the middle is surrounded by two toroid end-cap magnets and the toroid magnet in the barrel region (43).

3.2.6 Trigger System

The majority of events in proton-proton collisions at the LHC are minimum bias and QCD multijet events. The data size of one ATLAS event is ∼1.3 MB. With the rate 40 MHz, in case of storing every single event, we would expect a constant data flow of ∼52 TB/s. A data flow of this amount is impossible to manipulate. For the purpose of reducing the amount of data, a sophisticated trigger system has been developed. The trigger system is specialized to select only the events that are potentially interesting for a further analysis.

The ATLAS trigger is a three level trigger system. It is designed to reduce the initial 40 MHz rate to 200 Hz, which can be saved for the later analysis. Effectively it means to decrease the data flow from ∼52 TB/s to less than 1 GB/s.

The first level trigger (L1) is a hardware based trigger system, consisting of electronics and purpose-built processors located close to the detector. The goal is to reduce the initial 40 MHz rate to approximately 75 kHz. Signatures from electrons, high p_{T} jets, hadronic taus, muons or missing energy are searched, since these signatures are of

main interest for physics analyses in ATLAS. Based on the reduced granularity information from the detector and predefined thresholds, object selection at L1 is applied. Based on the object multiplicity, the L1 decision is then reached. If an object in the event will pass this selection, the event is allowed to pass to the higher trigger level for a further evaluation.

Level 2 (L2) trigger is a part of the Higher Level Trigger (HLT). It is a software based trigger that defines sophisticated calorimeter, track, and muon based variables within the so-called Regions-of-Interest (RoI's). The RoI's are regions of the detector where the L1 trigger has identified the trigger objects, whose position in η and ϕ is being passed to the L2 trigger. These variables are defined to be sensitive to the signatures of the various final state particles (e.g. the shape of the calorimeter shower). At L2, full granularity of the calorimeter and muon chamber data is used, as well as the data from the inner detector. The decision is reached by applying thresholds, which are defined based on Monte Carlo simulation (or data, if available). The fact, that only the data within the RoI is used for providing the L2 decision reduces the amount of data significantly, roughly to $\sim$10's kB (1-2% of the full event size), and thus reduces the processing time. The rate reduction provided at L2 is roughly by a factor of 15.

At EF, the same reconstruction algorithms as in offline are used. Selection variables, calorimeter and track based, are defined at EF similarly to L2, but with more precise information on e.g. the number of inner detector hits, or the primary vertex position. The final state particles at the EF are reconstructed within the RoI with the possible access to the full event read out if needed, which allows us to provide a decision based on the properties of the event. The thresholds applied at EF are tuned using Monte Carlo simulation (or data, if available), and specified by the physics purpose of the trigger. If an event has passed the so-called trigger chain, consisting of the sequence of L1, L2 and EF requirements, it is stored at the storage element and reconstructed. The various trigger items are distinguished in the notation, as for example: EF_TAU29_MEDIUM (tau trigger with a requirement on the tau energy of 29 GeV at EF, and "medium" tau identification requirements - see chapter 3.3.4, and given L1 and L2 requirements), EF_MU15 (muon trigger with a requirement on the muon transverse momentum at EF of $\sim$15 GeV, and given L1 and L2 requirements), etc.

All trigger items share the bandwidth at every trigger level. It is therefore important when designing a trigger item, to make sure, that the rate of any single trigger item

will not be that large, that the sum of the rates of all items would not exceed the total bandwidth at every trigger level. For this reason a trigger management has been established that decides on which trigger items (and when) can be deployed. The rate of a single item is dependent on the applied cuts and can be also controlled by prescales. The prescale is an integer "n", which decides, that only every "n-th" event in which a particular trigger has fired will pass to the next trigger level. The case n=1 means that no prescales are applied, or simply referred to as "unprescaled". The prescales can be applied at any of the three levels L1, L2 and EF. The final prescale is then calculated by multiplying all prescales at every trigger level.

3.2.6.1 Tau trigger

The tau trigger aims to provide an online selection of narrow and isolated jets with low track multiplicity, which, combined, is the typical signature of hadronically decaying taus.

The **L1 tau trigger** is using the so-called trigger towers with the size $\Delta\eta \times \Delta\phi$ = 0.1×0.1, composed of calorimeter cells in the EM and Had calorimeter, with the coverage of up to $|\eta| < 2.5$. Tau candidate at L1 is selected in the RoI composed of 4×4 trigger towers, divided into 2×2 towers of the central core and the isolation ring of 12 towers surrounding the core, as shown in figure 3.15. The energy of the L1 tau candidate is calculated from the two most energetic neighbouring towers in the core in the EM calorimeter, and from the full core in the Had calorimeter. The position of the L1 tau is defined by the center of the RoI.

The rates of the L1 tau trigger items are controlled by the thresholds on the transverse energy, E_{T}, of the L1 tau candidate, or prescales. The trigger items are at L1 defined by the energy thresholds, such as L1_TAU6, L1_TAU8, L1_TAU11 and L1_TAU50, where the number in the trigger name corresponds to the minimal required L1 tau E_{T} in GeV. The rates of the L1 tau items deployed in 2011, as a function of the instantaneous luminosity, are shown in figure 3.16.

The rate reduction provided by the **L2 tau trigger** is obtained by cutting on defined variables that are sensitive to the specific characteristics of taus. The position of the L2 tau is obtained by refining the position of the L1 tau, using the seconds layer of the calorimeter. The selection variables at L2 are defined in the RoI of the size $\Delta\eta \times \Delta\phi$ =0.6×0.6 around the L2 tau direction.

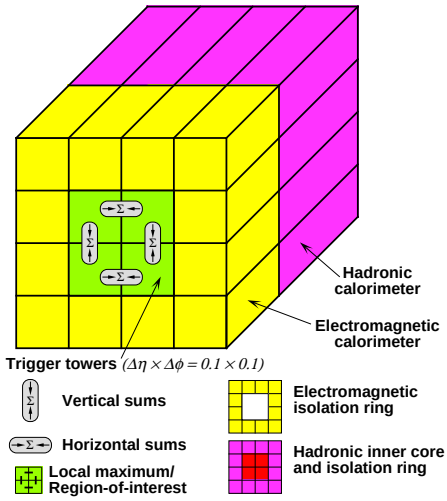

Figure 3.15: Schematic view of the EM and Had trigger towers showing the isolation and the core region (40).

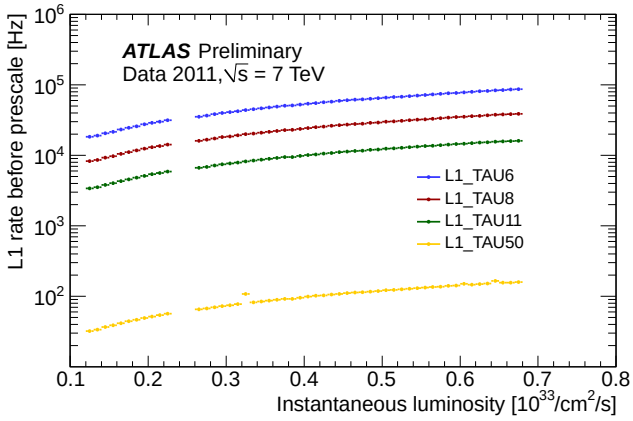

Figure 3.16: L1 rates before prescale versus the instantaneous luminosity measured by ATLAS for four different L1 tau items (45).

One of the variables, that can provide a good selection of narrow jets is the L2 electromagnetic radius, R_{EM}. It is an energy weighted radius, calculated from cells in the EM calorimeter:

$$R_{\mathrm{EM}} = \frac{\sum_{\mathrm{cell}} E_{\mathrm{cell}} \Delta R_{\mathrm{cell}}}{\sum_{\mathrm{cell}} E_{\mathrm{cell}}}, \tag{3.3}$$

where ΔR_{cell} is the distance of the EM calorimeter cell (with the energy E_{cell}) to the

direction of the L2 tau candidate. The distribution of R_{EM} at L2, for the QCD dijet events estimated from data, and for taus obtained from the Monte Carlo simulation, is shown in figure 3.17. Another possibility to reduce the rate at L2 is to apply a

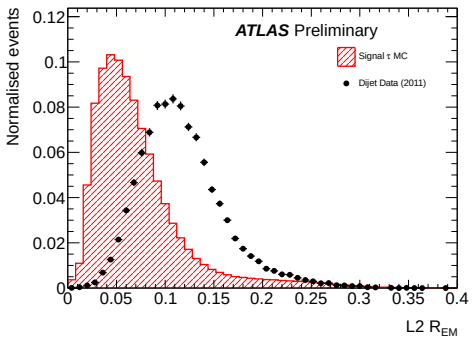

Figure 3.17: The distributions of the electromagnetic radius, R_{EM} at L2. The hatched histogram represents the signal taus from Monte Carlo, while the black points represent the QCD dijets (45).

cut on the E_{T} of the L2 tau candidate, which is calculated from all calorimeter cells within the L2 RoI, with an applied suppression of the electronic and pile-up noise. The tracking information at L2 is exploited by defining the ratio $p_{\mathrm{T}}^{\mathrm{iso}}/p_{\mathrm{T}}^{\mathrm{core}}$, where $p_{\mathrm{T}}^{\mathrm{core}}$ is the scalar sum of the momenta of all L2 tracks in the "core" region, $\Delta R < 0.1$, around the direction of the L2 tau, and $p_{\mathrm{T}}^{\mathrm{iso}}$ is the sum of the scalar momenta of all tracks in the isolation ring, $0.1 < \Delta R < 0.3$, centered around the L2 tau direction. This variable is sensitive to the isolation of the true taus. Tracks at L2 are reconstructed by the so-called IDScan algorithm, which takes as an input the information from the Pixel and SCT detectors to provide a fast reconstruction of the inner detector tracks (46).

At the **EF level**, similarly as at L2, a range of selection variables sensitive to the signatures of the taus is defined, and selection cuts are applied. The EF tau is reconstructed in the same way as in offline[1], with the restriction on the RoI, which at the EF is defined as the rectangular region $\Delta\eta \times \Delta\phi$ =0.8×0.8 around the position of the L2 tau candidate.

[1] As the EF uses the same reconstruction methods as used in offline, and in order not to mention the same information twice, in the discussion about the EF tau trigger it is assumed, that the reader understands the offline tau reconstruction and the association of the tracks to the offline taus, which will be discussed in the later section 3.3.4.

The selection variables that help to provide rate reduction at the EF are the electromagnetic radius R_{EM}, track average distance R_{track} and tau E_{T} over the leading track $p_{\mathrm{T}}^{\mathrm{leadTrk}}$, $f_{p_{\mathrm{T}}^{\mathrm{leadTrk}}}^{E_{\mathrm{T}}}$, defined as:

$$
\begin{aligned}
R_{\mathrm{EM}} &= \frac{\sum_{\Delta R<0.4} E_{\mathrm{cell}} \Delta R_{\mathrm{cell}}}{\sum_{\Delta R<0.4} E_{\mathrm{cell}}}, \\
R_{\mathrm{track}} &= \frac{\sum_t p_{\mathrm{T}}^t \Delta R_t}{\sum_t p_{\mathrm{T}}^t}, \\
f_{p_{\mathrm{T}}^{\mathrm{leadTrk}}}^{E_{\mathrm{T}}^{\tau}} &= \frac{E_{\mathrm{T}}}{p_{\mathrm{T}}^{\mathrm{leadTrack}}},
\end{aligned}
\tag{3.4}
$$

where $\sum_{\Delta R<0.4}$ runs over all EM calorimeter cells with the energies E_{cell} in the cone $\Delta R < 0.4$ around the EF tau direction, and $\sum_t$ runs over all tracks with the transverse momentum p_{T}^t, associated to the EF tau. The cuts on the selection variables are parametrized as a function of the transverse momentum of the EF tau, and depending on its track multiplicity, the selection is optimized separately for taus with one track, and with more than one track, associated to the EF tau.

The full tau trigger chain (L1-EF) consists of dedicated items at L1, L2 and EF. For example, the trigger chain TAU16_LOOSE consists of L1_TAU6, L2_TAU16_LOOSE and EF_TAU16_LOOSE items, and the TAU29_MEDIUM consists of L1_TAU11, L2_TAU29_MEDIUM and EF_TAU29_MEDIUM items, where the numbers in the names of the items represent the respective E_{T} cut on the trigger tau at every trigger level. The LOOSE and MEDIUM selection criteria in the names of the items reflect the tightness of the cuts on the variables defined in the equation 3.4. Sometimes, for practical reasons (and it will be case from now until the rest of this thesis), we write EF_TAU16_LOOSE and EF_TAU29_MEDIUM for the full trigger chain, accounting also for L1 and L2[1].

To keep the rates of the tau trigger items acceptable at every trigger level, we can either tighten the tau trigger thresholds, or apply the prescales, or use it in the combination with various other trigger items. The later gives rise to the combined trigger chains tau+X, where X can be another tau, missing transverse energy, muon, electron or a jet trigger chain. The total rate of all single tau trigger chains, together with the combined tau+X trigger chains, that were deployed during the 2011 data taking, was roughly 50-60 Hz. The rates of some single, or combined, tau trigger chains

[1]To name the whole chain by its last item is a practical way of write down the whole chain, since in this way we are certain what is the last item of the trigger chain.

that consist of at least one tau trigger chain, are shown as a function of instantaneous luminosity in figure 3.18.

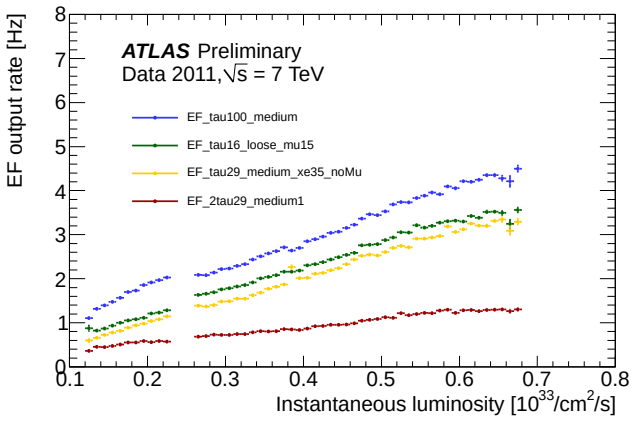

Figure 3.18: Trigger rate as a function of instantaneous luminosity for the EF_TAU100_MEDIUM, EF_TAU16_LOOSE_MU15, EF_TAU29_MEDIUM_XE35NOMU and EF_2TAU29_MEDIUM1 triggers.

During most of the 2011 data taking until the end of August 2011, the combined triggers EF_TAU16_LOOSE_MU15 and EF_TAU29_MEDIUM_XE35NOMU were the lowest (loosest cuts) unprescaled combined triggers for the tau+muon and tau+missing E_{T} signatures. These triggers will play an important role in the analysis presented in this work.

3.2.7 Simulation of the ATLAS detector

The detector response of ATLAS is simulated by the `GEANT4` framework (47). The `GEANT4` simulation of the ATLAS detector takes as an input the information about particles obtained from a Monte Carlo generator, and based on a detailed information of all detector subparts, it simulates the interactions of the particles with the traversed material of the detector. The process which starts by generating events using Monte Carlo generators, and using `GEANT4` to simulate the detector response of ATLAS, will be referred to as the Monte Carlo simulation. In the later steps, these simulated events can be reconstructed using the same reconstruction algorithms as used for real data events, which allows a direct comparison of real data and Monte Carlo.

3.3 Offline reconstruction

After it was saved to the mass storage, the raw detector response is being reconstructed. Starting from the energy deposits in the calorimeter cells, and from hits in the inner detector and in the muon spectrometer, algorithms run the reconstruction of calorimeter clusters and tracks. From this, based on the properties of the tracks and clusters, we can reconstruct the candidates for the physics objects such as electrons, muons, taus, jets, or derived objects such as missing energy. In the following sections, the reconstruction of the objects which are most interesting in the scope of this thesis will be presented.

3.3.1 Track reconstruction

The reconstruction of the tracks is based on the information provided by the inner detector (43) (50). There are two different approaches how to reconstruct tracks in ATLAS.

The default starts from creating a three dimensional representation of silicon (Pixel and SCT) detector measurements (hits), the so-called space-points. Track seeds are built from the combination of space-points in the Pixel detector and in the first layer of the SCT. These seeds are extended through the whole SCT to form the track candidates. In order to avoid cases when two track candidates share the same track segments, the so-called "ambiguity solving" is applied. This provides scores to different track candidates based on the number of hits associated to the track, and selects track candidates with the highest scores. The selected tracks are then extrapolated to the outer part of the inner detector to associate the drift circle information from the TRT and resolve left-right ambiguities. The extended tracks are then refitted, including the full information from the inner detector.

The complementary track finding method is useful in cases when a track candidate doesn't have a silicon hit, e.g. K_s decays deep in the inner detector, or photon conversions. This method therefore starts from the TRT with track segments that are identified using Hough transform mechanism, and are then followed back into the silicon detectors to find track segments that have been missed in the default method.

Once the the track is reconstructed, we can estimate the momentum p of the track from a known curvature of the track in the inner detector.

At the post-processing stage, based on the knowledge about the reconstructed tracks, a vertex finder algorithm is used, to reconstruct the primary vertices. The details of the primary vertex reconstruction can be found in the reference (51).

3.3.2 Reconstruction of calorimeter clusters

The main purpose of the reconstruction of the calorimeter clusters (43) is to group together all calorimeter cells that can be associated to one incoming particle, such as an electron, or a hadron. The clusters reconstructed with the "topological" algorithm are the so-called topological clusters, or topo-clusters. The topo-clusters represent a three-dimensional energy deposit in the calorimeter.

The reconstruction of the topo-clusters starts from a so-called "seed cell". A seed cell is a calorimeter cell with energy exceeding a threshold of 4σ above the noise level, where the noise level is the RMS of the electronic noise and the pile up noise. All neighbouring cells are collected around the seed cell. If a neighbouring cell has the energy exceeding 2σ above the noise level, this cell is the so-called secondary seed and its neighbours are also collected. Finally, all surrounding cells above a very low threshold, typically set to 0σ, are added if no more secondary seeds are among the direct neighbours.

In case of two or more particles being close to each other, this procedure will cause non-isolated clusters with two or more local maxima. In such case, the cluster splitting along the signal valleys between the maxima is applied.

The energy of the topo-cluster is equal to the sum of the energies of the associated cells. The mass of the topo-cluster is zero, and the direction of the topo-cluster is a unit vector originating from the center of the ATLAS coordinate system to the barycenter computed from the energy weighted η and ϕ of all associated cells (48).

The ATLAS calorimeter is calibrated at the electromagnetic scale and is defined to reproduce correctly the energy of the electrons. However, the calorimeter response of the electrons and hadrons is different. Therefore, the energy response of the hadrons in the calorimeter is corrected at the level of topo-clusters, using the so-called Local Hadronic Calibration (LC). The LC is obtained by using Monte Carlo simulation of charged pions, and uses the simulation of the ATLAS detector. For further information on the LC, the reader can consult the reference (49).

3.3.3 Jet reconstruction

The purpose of the jet reconstruction is to group together all final state particles produced during the hadronization of a parton. For the jet reconstruction, jet clustering algorithms are used. The algorithms can use as an input any objects having a four-momentum representation. These can be calorimeter cells, calorimeter clusters, inner detector tracks, and others. The input objects can also be stable Monte Carlo truth particles from the generator, and in this case, the created jets will be called the "truth jets". At the detector level, the jets are most commonly built from the topo-clusters (in this section, for simplicity, only clusters).

The current standard jet clustering algorithm used in ATLAS is the anti-k_t algorithm. The advantage of the anti-k_t algorithm over other commonly used algorithms is that it is both infrared safe (soft emissions doesn't affect the jets) and collinear safe (collinear splitting doesn't affect the jets) (52).

Using the clusters as the input to the anti-k_t algorithm we build jets by using two functions:

$$d_{ij} = min(k_{t,i}^{-2}, k_{t,j}^{-2}) \frac{\Delta R_{ij}^2}{R^2}, \tag{3.5}$$

$$d_a = k_{t,a}^{-2}, \tag{3.6}$$

where the $k_{t,a}$ is the transverse momentum of the cluster a, ΔR_{ij} is the distance in ΔR between clusters i and j and R is a parameter that controls the size of the jet. In ATLAS, for most analyses including the analysis presented in this work, it is $R = 0.4$. From this, the algorithm obtains its name, the anti-k_t04 algorithm. The function d_{ij} represents a measure of distance between clusters i and j. The anti-k_t algorithm runs over in the following steps:

- For all clusters in the event define d_a according to the equation 3.6.
- For every combination of the clusters i and j in the event define d_{ij} from the equation 3.5.
- Compare d_a and d_{ij}, and find the smallest of all.
- If d_a is the smallest, call cluster a a jet, and remove it from the event clusters.

- If d_{ij} is the smallest, combine the clusters i and j into a new cluster.
- Repeat until no clusters are left in the list.

After the jet is created, the four-momentum of the the jet is calculated as the vector sum of the four-momenta of the associated clusters (53).

The difference between the anti-k_t and the k_t algorithms lies in the exponent over the $k_{t,i}$ ($k_{t,j}$), in the equations 3.5 and 3.6. For anti-k_t, the exponent is -2, for k_t it is (+)2. While with anti-k_t, the algorithm starts from the hardest cluster, with k_t it is from the softest cluster. The anti-k_t algorithm creates rather circular hard jets, which correspond more to the quantitative properties of jets than the k_t algorithm, which creates jets with a more complicated structure. The comparison of jets created by the anti-k_t and the k_t algorithms is shown in figure 3.19 (52).

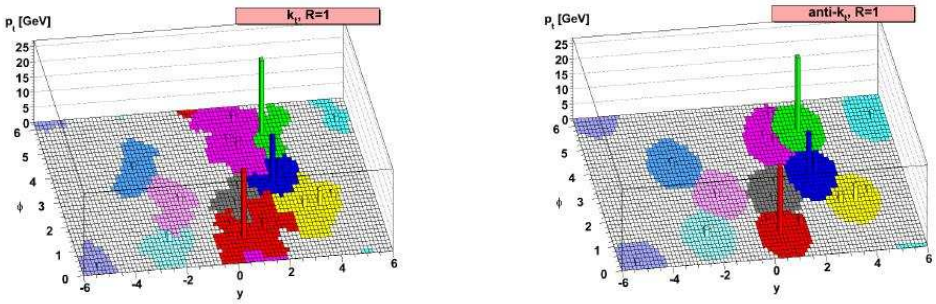

(a) (b)

Figure 3.19: The k_t algorithm (a) and the anti-k_t algorithm (b) comparison. The colored objects are the reconstructed jets (52).

3.3.4 Tau reconstruction

The reconstruction of the taus concerns only the hadronicaly decaying taus[1]. The reconstruction of the taus starts from anti-k_t04 jets, which have $|\eta| < 2.5$, and the transverse momentum $p_{\mathrm{T}} > 10$ GeV (54). The four-momentum of the reconstructed

[1]Later in this thesis, the hadronicaly decaying taus can be labeled as τ_{had} mainly in the cases when it is important to emphasize the decay channel of the tau, such as in the case of $Z \rightarrow \tau\tau \rightarrow \mu\tau_{\mathrm{had}}$ decays, where one tau decays into a muon and the other decays hadronicaly. Moreover, unless the decay channel (into an electron or a muon) is explicitly specified, tau, τ, or τ_{had} will be from now on equivalent and will refer to the hadronicaly decaying tau.

tau candidate is defined in terms of η, ϕ and the transverse momentum p_{T}. The η and ϕ of the reconstructed tau are taken from the sum of the four-vectors of the topo-clusters, associated to the seed jet. The mass of the reconstructed tau is defined to be zero. Therefore $p_{\mathrm{T}} = E_{\mathrm{T}}$, where $E_{\mathrm{T}} = E\sin(\theta)$ is the transverse energy of the tau. The energy E is calculated from the topo-clusters in the cone $\Delta R < 0.2$, around the tau direction. Using Monte Carlo simulation, the energy of the reconstructed tau is corrected to the "tau scale", which on average restores the tau energy to its true value (54).

Depending on the final state charged particle multiplicity, hadronic decays are characterized as either one-prongs (one charged particle, 76.5% of all hadronic decays) or three-prongs (three charged particles, 23.5% of all hadronic decays). Reconstructed tracks are associated to the tau candidates if they are in the cone $\Delta R < 0.2$ around the direction of the reconstructed tau, and satisfy the following conditions:

- $p_{\mathrm{T}}^{\mathrm{track}} > 1$ GeV
- Number of B layer hits ≥ 1
- Number of pixel hits ≥ 2
- Number of pixel+SCT hits ≥ 7
- $|d_0| < 1$ mm
- $|z_0 \sin(\theta_{\mathrm{track}})| < 1.5$ mm

The parameter d_0 is the distances of the closest approach of the track to the primary vertex in the transverse plane, and z_0 is the longitudinal distance of closest approach. However, for identification (which is done in a later step) tracks up to $\Delta R < 0.4$ (around the reconstructed tau) are used for calculating the identification variables. These tracks must also pass the previous track criteria.

3.3.5 Tau identification

In order to distinguish taus from the overwhelming amount of QCD jets, tau identification must be applied (54). The tau identification uses variables that are sensitive to the typical signatures of the tau jets: calorimeter and tracking isolation, narrowness and

low track multiplicity. There are three main tau identification (ID) methods available: *i*) a cut based ID, *ii*) a Likelihood based ID, *iii*) a Boosted decision trees (BDT) ID.

Each method uses a slightly different set of identification variables in identify taus. Many of the selection variables are correlated, and it is not the goal of this section to explain all of them, but rather introduce the selection variables, and explain on some the differences between the taus and the QCD jets, or electrons respectively. The selection variables used for the identification are the following:

Calorimeter (Cal) Radius:

$$R_{\mathrm{Cal}} = \frac{\sum_{i\in all}^{\Delta R_i<0.4} E_{\mathrm{T}}^{i} \Delta R_i}{\sum_{i\in all}^{\Delta R_i<0.4} E_{\mathrm{T}}^{i}}, \tag{3.7}$$

where ΔR_i is the distance of the cell i, with energy E_{T}^{i}, in all layers of the ATLAS calorimeter, to the reconstructed tau. This variable uses the fact that a tau jet is narrower than the typical QCD jet and deposits most its energy in a relatively small cone. It is therefore likelier that the taus will have smaller R_{Cal} than the typical QCD jets. This can be seen in figure 3.20, where R_{Cal} of the reconstructed taus from the Monte Carlo simulation is compared to the R_{Cal} of the QCD jets for 1-prong tau candidates.

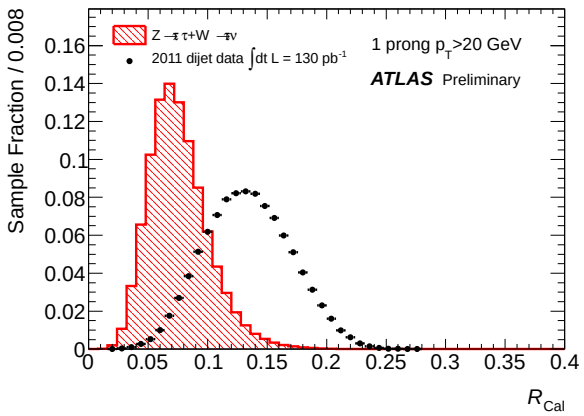

Figure 3.20: The R_{Cal} distribution of the reconstructed taus from Monte Carlo simulation and for QCD dijets from real data (54).

Track Radius:

$$R_{\text{track}} = \frac{\sum_t^{\Delta R_t<0.4} p_{\text{T}}^t \Delta R_t}{\sum_t^{\Delta R_t<0.4} p_{\text{T}}^t}, \tag{3.8}$$

where t runs over all tracks within the distance $\Delta R_t < 0.4$ from the tau direction and p_{T}^t is the transverse momentum of the track. The usage of R_{track} is similarly motivated as R_{Cal}. Here is it also the feature of the tau being narrower than the typical QCD jet which is exploited.

Core energy fraction:

$$f_{\text{core}} = \frac{\sum_{j\in\text{all}}^{\Delta R_j<0.1} E_{\text{T}}^j}{\sum_{j\in\text{all}}^{\Delta R_j<0.4} E_{\text{T}}^j}, \tag{3.9}$$

where E_{T}^j is the transverse energy of the calorimeter cell j in all calorimeter layers and ΔR_j is the distance in ΔR of the cell j to the tau direction. This variable exploits the fact that the taus have the energy concentrated in a small cone close to the direction of the tau, while the QCD jets are more spread within $\Delta R < 0.4$.

Electromagnetic fraction:

$$f_{\text{EM}} = \frac{\sum_{i\in\text{EM 0--2}}^{\Delta R_i<0.4} E_{\text{T}}^i}{\sum_{j\in\text{all}}^{\Delta R_j<0.4} E_{\text{T}}^j}. \tag{3.10}$$

This variable is sensitive to the π^0 content in the taus which, mainly in the case of one-prong tau decays, can carry a significant fraction of the total energy of the tau. The comparison of f_{EM} for the taus and the QCD jets, for one-prong and three-prong tau candidates, is shown in figure 3.21

Cluster mass (m_{cluster}) and **Track mass** (m_{track}): Invariant masses calculated from the vector sum of the clusters associated to the reconstructed tau, and the tracks respectively, in the cone $\Delta R < 0.4$ around the tau direction. Both variables use the fact, that in the QCD jets, the associated clusters and tracks are wider spread than in the taus and thus the invariant masses for the QCD jets will be higher than for the taus. The variables m_{cluster} and m_{track} for the taus are limited by its physical mass, but there is no direct limitation for the masses of the QCD jets.

Number of isolation tracks ($N_{\text{track}}^{\text{iso}}$): Number of tracks in the isolation annulus $0.2 < \Delta R < 0.4$. Unlike than for real taus, for QCD jets, the tracks are not located in a narrow cone around the reconstructed tau axis, but are wide, exceeding the cone

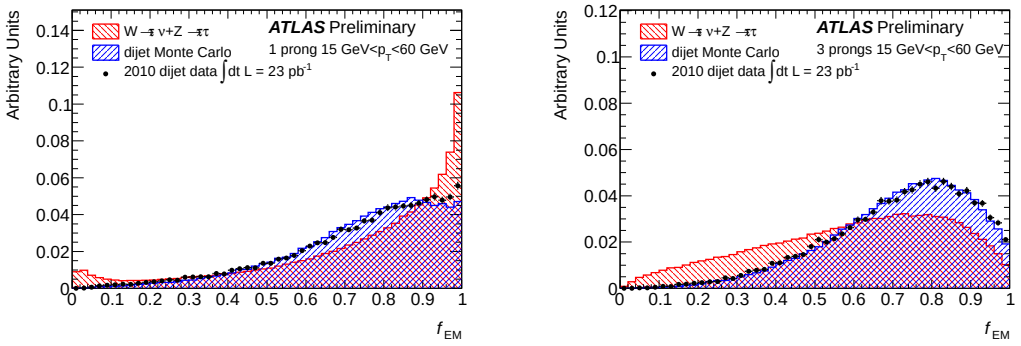

(a) (b)

Figure 3.21: The electromagnetic fraction in signal Monte Carlo and in QCD dijet data and Monte Carlo, for one-prong (a) and three-prong (b) tau candidates (55).

$\Delta R = 0.2$. In figure 3.22 is the comparison of $N^{\text{iso}}_{\text{track}}$ for QCD jets and taus from Monte Carlo simulation.

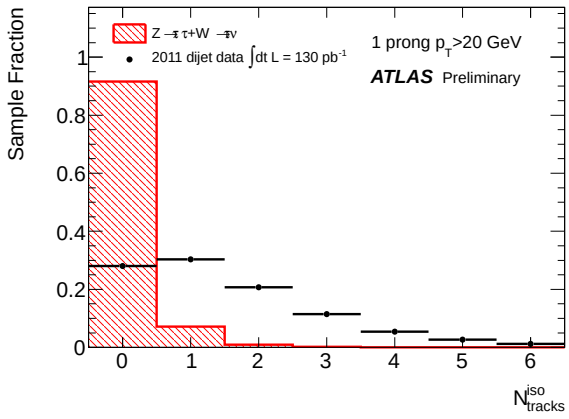

Figure 3.22: Number of isolation tracks in signal, and in QCD background extracted from real data (54).

Transverse flight path significance:

$$S_{\text{T}}^{\text{flight}} = \frac{L_{\text{T}}^{\text{flight}}}{\delta L_{\text{T}}^{\text{flight}}}, \tag{3.11}$$

where $L_{\text{T}}^{\text{flight}}$ is the distance between the primary and the secondary vertex calculated

for multiprong taus and $\delta L_{\mathrm{T}}^{\mathrm{flight}}$ is the uncertainty on $L_{\mathrm{T}}^{\mathrm{flight}}$. The tracks used for the secondary vertex fit are the tracks associated to the tau candidates, but also tracks with $p_{\mathrm{T}} > 6$ GeV within $\Delta R < 0.2$ of the jet seed, and satisfying $|d_0| < 2$ mm and $|z_0 \sin(\theta)| < 10$ mm.

Leading track IP significance:

$$S_{\mathrm{leadTrk}} = \frac{d_0}{\delta d_0}, \tag{3.12}$$

where d_0 is the distance of the closest approach of the leading tau track to the reconstructed primary vertex in the transverse plane, and δd_0 is its estimated uncertainty.

Maximum Δ R (ΔR_{max}): The maximal ΔR between an associated core track and the tau candidate axis.

First 3 leading clusters energy ratio (f^3_{leadClus}): The ratio of the energy of the three clusters with the highest energy, over the total energy of all clusters.

Ring isolation:

$$f_{\mathrm{iso}} = \frac{\sum_{i \in EM\ 0-2}^{0.1<\Delta R_i<0.2} E_{T,i}}{\sum_{j \in EM\ 0-2}^{\Delta R_j<0.4} E_{T,j}}, , \tag{3.13}$$

where i runs over cells in the first three layers of the EM calorimeter in the annulus $0.1 < \Delta R < 0.2$, around the tau candidate axis, and j runs over EM cells in $R_j < 0.4$ wide cone.

Hadronic radius (R_{Had}):

$$R_{\mathrm{Had}} = \frac{\sum_{i \in \mathrm{Had,EM3}}^{\Delta R_i<0.4} E^i_{\mathrm{T}} \Delta R_i}{\sum_{i \in \mathrm{Had,EM3}}^{\Delta R_i<0.4} E^i_{\mathrm{T}}}, \tag{3.14}$$

where i runs over cells associated to the tau candidate in the hadronic and layer 3 of the EM calorimeter.

TRT HT fraction:

$$f_{\mathrm{TRT}} = \frac{N^{\mathrm{leadtrack}}_{\mathrm{TRTHigh}}}{N^{\mathrm{leadtrack}}_{\mathrm{TRTLow}}}, \tag{3.15}$$

where $N^{\mathrm{leadtrack}}_{\mathrm{TRTHigh}}$ is the number of high threshold TRT hits of the leading track and $N^{\mathrm{leadtrack}}_{\mathrm{TRTLow}}$ the number of low threshold TRT hits. This cut is effective to distinguish one-prong taus and electrons, since the probability of high threshold TRT hits is higher for electrons than for pions. The f_{TRT} for tau candidates from $Z \to \tau\tau$ and $Z \to ee$ Monte Carlo is shown in figure 3.23.

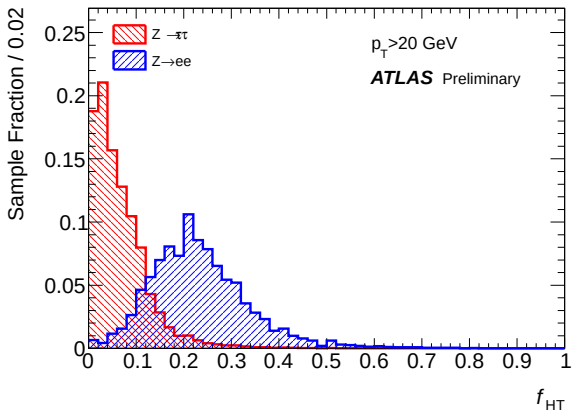

Figure 3.23: TRT HT fraction for tau candidates in $Z \rightarrow ee$ and $Z \rightarrow \tau\tau$ Monte Carlo (54).

Leading track momentum fraction:

$$f_{\text{track}} = \frac{p_{\text{T}}^{\text{leadtrack}}}{p_{\text{T}}^{\tau}}, \tag{3.16}$$

where $p_{\text{T}}^{\text{leadtrack}}$ is the transverse momentum of the leading track, and p_{T}^{τ} the transverse momentum of the reconstructed tau. This is another variable effective against electrons, since for electrons the $p_{\text{T}}^{\text{leadtrack}}$ will be roughly equal to the full reconstructed fake-tau p_{T}, while for the one-prong taus the f_{track} will be lower, due to the fraction of neutral energy in taus, which is not accounted in $p_{\text{T}}^{\text{leadtrack}}$.

Hadronic track fraction ($f_{\text{Had}}^{\text{leadtrack}}$):

$$f_{\text{Had}}^{\text{leadtrack}} = \frac{\sum_{j \in \text{Had}}^{\Delta R_j < 0.4} E_{T,j}}{p_{\text{T}}^{\text{leadtrack}}}, \tag{3.17}$$

where j runs over the cells in the hadronic calorimeter. This variable provides a strong rejection of electrons, and uses the fact, that electrons can deposit only a small fraction of their total energy in the hadronic calorimeter. The comparison of $f_{\text{Had}}^{\text{leadtrack}}$ between $Z \rightarrow ee$ and $Z \rightarrow \tau\tau$ is shown in figure 3.24.

Maximum strip $\mathbf{E}_T$ ($E_{\text{T,max}}^{\text{strip}}$): The maximum transverse energy deposited in a cell in the pre-sampler layer of the EM calorimeter, which is not associated with that of the leading track. This variable is also used mainly to reject electrons.

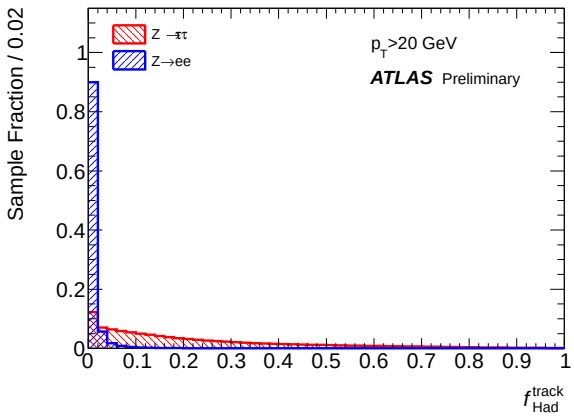

Figure 3.24: Hadronic fraction of tau candidates in $Z \rightarrow ee$ and $Z \rightarrow \tau\tau$ Monte Carlo (54).

The importance to veto electrons that can fake true hadronically decaying taus has been recognized and further studied in (28), (54).

3.3.5.1 Boosted decision trees as a method of the tau ID

Since the tau identification uses the BDT method, in this section, a brief explanation of the basic concept of the BDT is shown. For a more detailed description of the BDT, the reader can consult (56).

For the BDT based tau ID and the BDT based electron veto, the combination of the variables mentioned in the section 3.3.5 is used. The concept of the BDT is to create a tree-like structure of nodes, where each node represents a data sample with different compositions of signal and background. This is schematically illustrated in the figure 3.25.

This tree like structure is created during the so-called training of a decision tree, which is a process, in which the cut criteria for every node are decided. The training of a decision tree is done by using a training sample. The training sample is composed of signal (in the case of the tau ID it is the taus from the $Z \rightarrow \tau\tau$ Monte Carlo) and background (QCD background, or $Z \rightarrow ee$ for the BDT electron veto).

At the root node, the variable and the cut that gives the largest separation of signal and background is identified. The training sample is then divided into a signal-like and a background-like subsamples, and for each subsample a new node is created. Using the

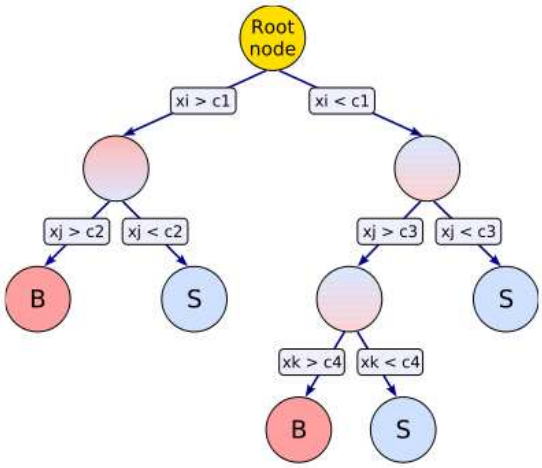

Figure 3.25: A simplified scheme of the BDT based selection (56).

same recipe as used for the initial root node, for both subsamples, again, the variable with the highest separation is chosen, and a cut is defined. This scheme continues until a stopping condition is satisfied, which is in the case of BDT based tau ID the minimum number of tau candidates contained within a node (55). The boosting is a procedure of giving larger weights to the signal events that end up in the background node and vice versa. The initial training sample is then reweighted using these weights, and the decision tree is rebuilt with such "new" reweighted training sample.

The advantage of using BDT instead of a simple cut based selection is, that the signal can end up selected, even if it fails one of the signal selection cuts, which leads to a higher signal efficiency.

3.3.5.2 BDT tau ID

The BDT tau ID is separately tuned for the one-prong and three-prong taus. The list of variables used in the BDT tau ID is shown in table 3.2. The Jet BDT is used to separate QCD jets from taus, and electron BDT is used to separate electrons from taus.

The BDT tau ID takes the variables from the table 3.2 as an input, and the scores BDTJetScore and BDTEleScore are returned as the output. These scores represent a multidimensional projection of the variables into a one dimensional space, which is meant to optimize the separation between taus and jets (BDTJetScore), or electrons

Track multiplicity	Variables
Jet BDT 1 prong	R_{Cal}, R_{track}, f_{track}, f_{core}, $N^{\mathrm{iso}}_{\mathrm{track}}$, $f^{3}_{\mathrm{leadClus}}$, m_{cluster}, S_{leadTrk}
Jet BDT 3 prong	R_{Cal}, R_{track}, f_{track}, f_{core}, $N^{\mathrm{iso}}_{\mathrm{track}}$, $f^{3}_{\mathrm{leadClus}}$, m_{cluster}, m_{track}, $S_{\mathrm{T}}^{\mathrm{flight}}$, S_{leadTrk}, ΔR_{max}
Electron BDT 1 prong	R_{track}, f_{track}, f_{core}, f_{iso}, f_{EM}, $f^{\mathrm{Trk}}_{\mathrm{had}}$, f_{TRT}, $E^{\mathrm{strip}}_{\mathrm{T,max}}$, R_{Had}

Table 3.2: Variables used in the BDT tau ID (54).

(BDTEleScore) respectively. The tightness of the tau identification is specified by cutting on these scores. The scores are calculated by using a dedicated package, provided by the ATLAS tau working group. The tightness of the identification efficiency is given with respect to the true taus, in the combined $Z \to \tau\tau$ and $W \to \tau\nu$ Monte Carlo samples. Three working points are defined: "loose" with ∼70% signal efficiency, "medium" with ∼50% signal efficiency, and "tight" with ∼30% signal efficiency. The distributions of BDTJetScore for one-prong and multi-prong taus, for signal and QCD background, is shown in figure 3.26, and the distributions of BDTEleScore is shown in figure 3.27, for signal and $Z \to ee$ background.

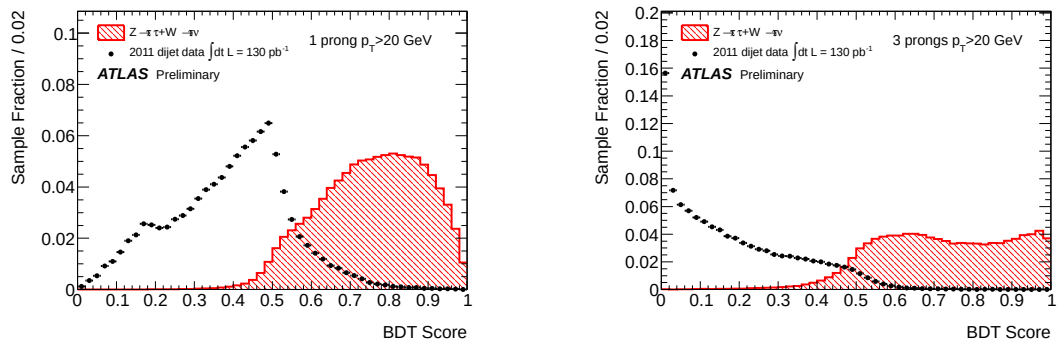

(a) (b)

Figure 3.26: BDTJetScore for signal and QCD dijet background obtained from real data. On (a) is the distribution for 1-prong, and on (b) is the distribution for 3-prong tau candidates (54).

In order to prove that the Monte Carlo provides precise estimates of the tau identification efficiency in data, an analysis which used the same selection in data and in Monte Carlo has been carried out. This analysis has been done on 2010 data, and included the selection of $W \to \tau\nu$ events, for which two different approaches have been

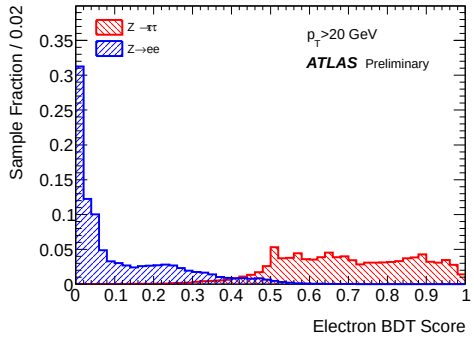

Figure 3.27: BDTEleScore for signal and background Monte Carlo samples (54).

used:

- Tag-and-probe method, which used the missing E_{T} (and other signatures unrelated to the tau ID) for tagging the real $W \rightarrow \tau\nu$ events in data, while measuring the tau ID efficiency of the taus.
- Cross section method, which selects the $W \rightarrow \tau\nu$ events without including the tau ID, and uses the knowledge of the cross sections of the signal and background to measure the deviation of the Monte Carlo from the data after applying the tau ID.

For a more comprehensive description of this measurement the reader should consult the reference (57). The BDT tau ID scale factors for different tau ID methods are shown in figure 3.28. The scale factors represent a measure of mismodeling of the taus in Monte Carlo and provide us a number (or a function), which the Monte Carlo has to be scaled with, in order to get the same tau ID efficiency as in real data. The comparison of real data and Monte Carlo has shown no significant disagreement in the tau ID efficiencies, which would exceed the statistical and systematic uncertainties of the measurements.

Figure 3.29 shows the inverse background efficiency as a function of the signal efficiency for one-prong and multi-prong tau candidates, for the three tau ID methods, for two different p_{T} bins of the taus. The signal efficiency is defined as:

$$\epsilon_{\mathrm{sig}}^{\mathrm{Nprong}} = \frac{\#\text{ of reconstructed Nprong tau candidates, passing the ID}}{\#\text{ of simulated true hadronic Nprong taus}}, \tag{3.18}$$

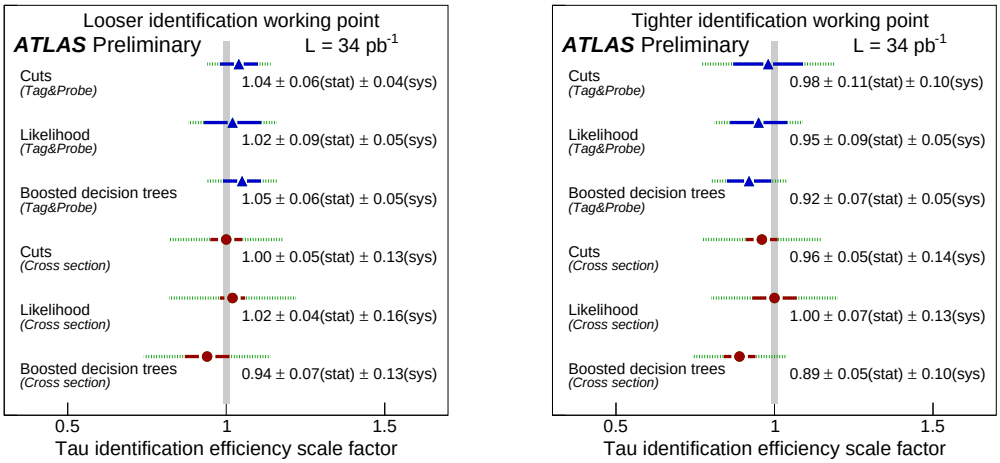

Figure 3.28: Tau identification scale factors for looser tau identification (a) and tighter tau identification (b), for different tau ID methods, and for different ways of estimating the tau ID efficiency from real data (57).

where the reconstructed tau candidates are truth-matched within $\Delta R < 0.2$ to the true visible tau, with $\left|\eta^{\text{Vis}}\right| < 2.5$ and $E_{\text{T}}^{\text{Vis}} > 10$ GeV. The visible tau consist of the vector sum of the visible tau decay products (i.e. excluding the neutrino) at the generator level. The background efficiency is defined as:

$$\epsilon_{\text{bckg}}^{\text{Nprong}} = \frac{\#\text{ of reconstructed Nprong tau candidates, passing the ID}}{\#\text{ of reconstructed Nprong tau candidates}}. \tag{3.19}$$

From the figures 3.29 it is clear that for both one-prong and three-prong taus the BDT ID is the most efficient in terms of signal efficiency vs. background rejection, and therefore it has been decided that the BDT tau ID will be used for the tau identification in this work.

3.3.6 Electron reconstruction and identification

Electrons are reconstructed (59) from clusters with energy above 2.5 GeV in the middle layer of the electromagnetic calorimeter, which are associated to a track in the inner detector. The track matching is done within $\Delta\eta \times \Delta\phi = 0.05 \times 0.1$ with respect to the position of the cluster.

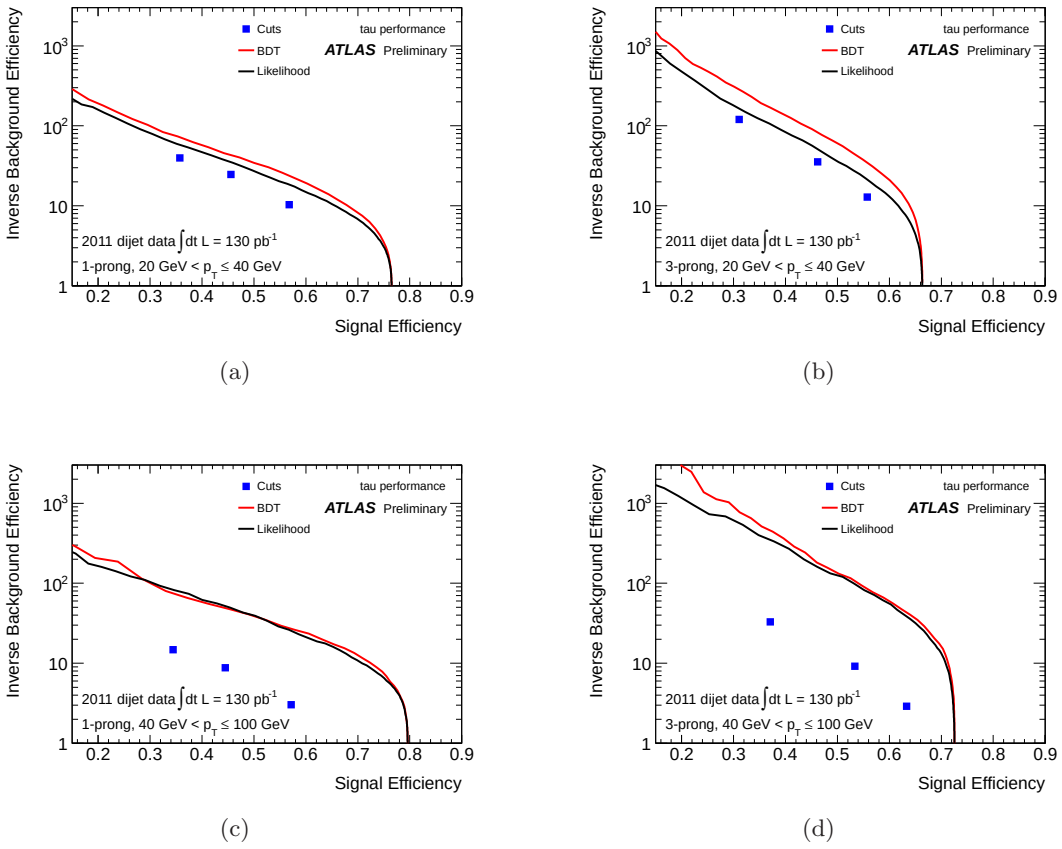

Figure 3.29: Signal efficiency vs. the inverted QCD background efficiency for the three different tau ID methods, for one prong (left) and three prong (right), and two different p_{T} ranges of the reconstructed tau. (54).

The energy of the electron is calculated as a weighted average of the cluster energy and the track momentum. The η and ϕ coordinates of the electron are taken from the associated track, unless the track has no silicon hits, in that case η and ϕ of the cluster are taken.

The identification of electrons is cut based, and uses tracking and calorimeter based variables. Three reference sets of cuts are used: loose, medium and tight. The identification efficiencies have been optimized (59) on $Z \rightarrow ee$ Monte Carlo, with (94.32±0.03)% efficiency for the loose selection, (90.00±0.03)% efficiency for the medium selection, and (71.59±0.03)% efficiency for the tight selection, for electrons with $E_{\mathrm{T}} > 20$ GeV. The estimated jet rejection for loose selection is by a factor of 1065 ± 5, for medium 6840 ± 70 and for tight $(1.39 \pm 0.06) \cdot 10^5$.

3.3.7 Muon reconstruction

The typical signature of a muon is a track traversing through the whole ATLAS detector (60). Depending on the reconstruction approach, the reconstructed muons are divided in three different classes: Stand-alone muons, Combined muons and Segment tagged muons.

Stand-alone muons are reconstructed using only the muon spectrometer. The flight direction is estimated by extrapolating the track from the muon spectrometer to the beam axis. The parametrized expected energy loss in the calorimeters is taken into account.

Combined muons are reconstructed from the inner detector tracks and the muon spectrometer tracks independently, and combined in the later step, accounting for the parametrized expected energy loss in the calorimeter.

Segment tagged muons are reconstructed from an inner detector track extrapolated to the muon spectrometer, which can be associated with a straight track segment in the precision muon chamber. The straight track segment is formed when combining the hits in the MDT layers that are close enough to be approximately on a line (i.e. the curvature of the muon in the magnetic field is negligible at this distance).

While the segment tagged muons are mainly used for low p_{T} muon studies, the highest purity muon candidates are the combined muons.

For the combined muons, to combine tracks in the inner detector and the muon spectrometer, two different algorithms are used. Those are the so-called Staco and

MuID algorithms. While the Staco algorithm starts from hits in the outer part of the muon spectrometer and reconstructs the muon track iteratively, adding middle and inner parts of the spectrometer layers until the full track is reconstructed, the MuID uses a Hough transform of the phase space, and the maxima in the Hough space is selected as a muon track.

A comparison between Staco and MuID algorithms is shown in figures 3.30 (a) and (b). In the direct comparison it is visible, that the performance of the MuID algorithm is slightly better than of the Staco algorithm. MuID has higher selection efficiency and flatter efficiency as a function of η than Staco. Also, the agreement of data and Monte Carlo is slightly better for the MuID algorithm.

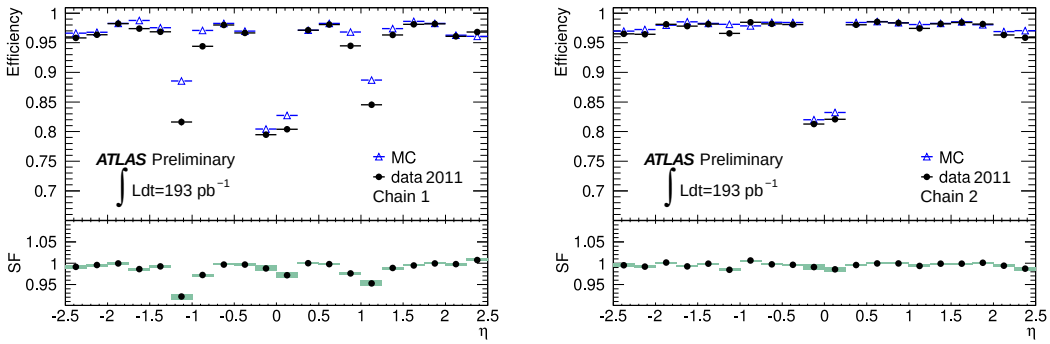

(a) (b)

Figure 3.30: Staco (a) and MuID (b) efficiency plots in Monte Carlo and in data, using the tag and probe method in $Z \to \mu\mu$ events. The drops in the efficiencies at $\eta \sim 0$ and $|\eta| \sim 1.2$ (only for Staco) are due to uninstrumented areas left for service work at $\eta \sim 0$, and due to the presence of only one muon chamber at $|\eta| \sim 1.2$, that makes it impossible to provide stand-alone measurement of muon tracks.

The total selection efficiency for the staco algorithm is $92.8 \pm 0.2\%$ and for MuID it is $95.8 \pm 0.1\%$. The efficiencies were obtained by using the tag and probe method in the real $Z \to \mu\mu$ events after background subtraction.

Thanks to its good performance, the Combined muons reconstructed with the MuID algorithm will be used in the current work.

3.3.8 Missing transverse energy reconstruction

The reconstruction of the missing transverse energy (61) relies on the fact, that the ATLAS detector is very hermetic. The transverse energy/transverse momentum in the

final state must be therefore in balance, and any violation of this balance must be explained by either the energy/momentum resolution of the detector, or the "missing" energy response from a weakly interacting final state particle, such as the neutrino. The missing transverse energy is reconstructed by including the contributions from energy deposits in the calorimeters $E_{\mathrm{x,y}}^{\mathrm{missCalo}}$ and the muons reconstructed in the muon spectrometer $E_{\mathrm{x,y}}^{\mathrm{miss}\mu}$, where x and y are the coordinates of the transverse plane to the beam axis.

The $E_{\mathrm{x,y}}^{\mathrm{missCalo}}$ components are calculated from the energies of the calorimeter cells associated to each physics object. The cells in the topo-clusters, which are not associated to any of the physics objects, are also taken into account. The calorimeter cells are calibrated to the energy scales of the reconstructed physics objects to which they are associated to. Therefore, $E_{\mathrm{x,y}}^{\mathrm{missCalo}}$ can be expressed as:

$$E_{\mathrm{x,y}}^{\mathrm{missCalo}} = E_{\mathrm{x,y}}^{\mathrm{Miss,e}} + E_{\mathrm{x,y}}^{\mathrm{Miss},\gamma} + E_{\mathrm{x,y}}^{\mathrm{Miss},\tau} + E_{\mathrm{x,y}}^{\mathrm{Miss,jet}} + E_{\mathrm{x,y}}^{\mathrm{Miss,softjet}} + E_{\mathrm{x,y}}^{\mathrm{Miss,calo}\mu} + E_{\mathrm{x,y}}^{\mathrm{CellOut}}, \tag{3.20}$$

where $E_{\mathrm{x,y}}^{\mathrm{Miss,e}}$ to $E_{\mathrm{x,y}}^{\mathrm{Miss,calo}\mu}$ are the negative sums of the calibrated calorimeter cells associated to the reconstructed electron ($E_{\mathrm{x,y}}^{\mathrm{Miss,e}}$), photon ($E_{\mathrm{x,y}}^{\mathrm{Miss},\gamma}$), tau ($E_{\mathrm{x,y}}^{\mathrm{Miss},\tau}$), a jet with $p_{\mathrm{T}} > 20$ GeV ($E_{\mathrm{x,y}}^{\mathrm{Miss,jet}}$), a "soft" jet with 7 GeV $< p_{\mathrm{T}} <$ 20 GeV ($E_{\mathrm{x,y}}^{\mathrm{Miss,softjet}}$), and the contribution corresponding to the energy loss of the μ in the calorimeter ($E_{\mathrm{x,y}}^{\mathrm{Miss,calo}\mu}$). The $E_{\mathrm{x,y}}^{\mathrm{CellOut}}$ is corresponding to the negative sum of cell energies in topo-clusters which were not associated to any of the physics objects.

The x and y components of $E^{\mathrm{Miss,Object}}$ in equation 3.20 are expressed as:

$$E_{\mathrm{x}}^{\mathrm{Miss,Object}} = -\sum_{i=1}^{N_{cell}} E_i \sin\theta_i \cos\phi_i, \tag{3.21}$$

$$E_{\mathrm{y}}^{\mathrm{Miss,Object}} = -\sum_{i=1}^{N_{cell}} E_i \sin\theta_i \sin\phi_i, \tag{3.22}$$

where E_i, θ_i and ϕ_i are the energy, polar and azimuthal angle of the calorimeter cell associated to the objects.

The $E_{\mathrm{x,y}}^{\mathrm{miss}\mu}$ components are calculated from the muon momenta:

$$E_{\mathrm{x,y}}^{\mathrm{miss}\mu} = -\sum_{i=1}^{Nmuons} p_{\mathrm{x,y}}^{\mu} \tag{3.23}$$

The energy from the muons is covered in the region of $|\eta| < 2.7$. For $|\eta| < 2.5$ combined muons are used, and for $2.5 < |\eta| < 2.7$ stand alone muons are required due to the limited coverage of the inner detector in $|\eta| > 2.5$.

In the 2010 data, a good understanding of $E_{\mathrm{T}}^{\mathrm{Miss}}$ in the $Z \to ll$ and $W \to l\nu$ ($l = e, \mu$) events has been achieved, as demonstrated in Ref. (61). As an example, figure 3.31 shows a good agreement for the low values of $E_{\mathrm{T}}^{\mathrm{Miss}}$ in data and in Monte Carlo in the $Z \to ee$ events.

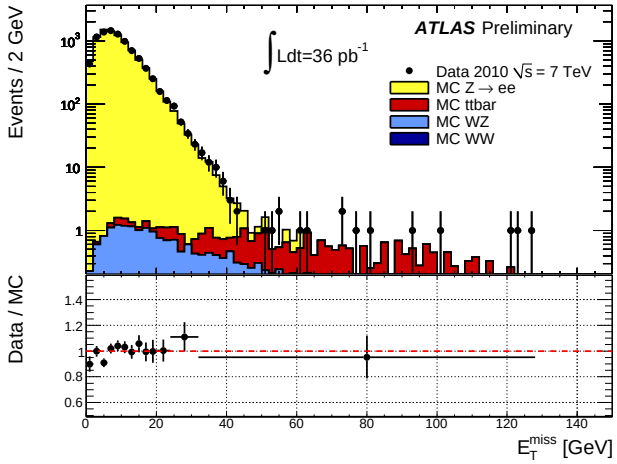

Figure 3.31: The distribution of $E_{\mathrm{T}}^{\mathrm{Miss}}$ in the selected $Z \to ee$ events in data and in Monte Carlo in the ATLAS detector, measured on the data collected in the full 2010 data taking. The lower plot shows the ratio of the data and the Monte Carlo distribution(61).

4

W+jet cross section, Z+jet cross section and the R_{JET} measurement in the tau decay channel with 2011 ATLAS data

The ATLAS measurements, $W \to \tau\nu$ observation (62), $W \to \tau\nu$ cross section measurement (63), $Z \to \tau\tau$ observation (64), and $Z \to \tau\tau$ cross section measurement (65), were done using 2010 data with the integrated luminosity of $\mathcal{L}_{\mathrm{int}} \simeq 33$ pb^{-1}. However, measurements of these signatures accompanied by one or more jets have not been carried out so far.

The cross section measurements of the $W(\to \tau\nu)$+jet and the $Z(\to \tau\tau)$+jet processes, $\sigma_{\mathrm{W+jet}}$ and $\sigma_{\mathrm{Z+jet}}$, are of high importance in the searches of any exotic resonance which decays into tau lepton(s) and jet(s), and thus are the main scope of this work. In addition to the $\sigma_{\mathrm{W+jet}}$ and $\sigma_{\mathrm{Z+jet}}$ measurements, the ratio R_{JET}, which is defined as:

$$R_{\mathrm{JET}} = \frac{\sigma_{\mathrm{W+jet}}}{\sigma_{\mathrm{Z+jet}}}, \tag{4.1}$$

will be estimated. The main goal of the R_{JET} measurement is to achieve a higher sensitivity to new physics than in the single $\sigma_{\mathrm{W+jet}}$ and $\sigma_{\mathrm{Z+jet}}$ measurements. This is achieved by canceling in the ratio those contributions to the total systematic uncertainty which are common for both $\sigma_{\mathrm{W+jet}}$ and $\sigma_{\mathrm{Z+jet}}$ measurements. An R_{JET} measurement has been performed by the ATLAS experiment using the 2010 data for the cases only

where the W and Z bosons decayed into electrons or muons, accompanied with exactly one jet (67).

In this work, the separate measurements of $\sigma_{\mathrm{W+jet}}$ and $\sigma_{\mathrm{Z+jet}}$ in the tau decay channel will be estimated, and finally, the results will be combined to estimate the R_{JET} ratio.

4.1 Cross section analysis methods

In order to improve the purity of the signal events in data, selection cuts in both $W(\rightarrow \tau\nu)$+jet and $Z(\rightarrow \tau\tau)$+jet analyses must be applied. Some selection criteria are common for both W+jet and Z+jet analyses. Therefore, first the common selection, and later the selection which specifies either the W+jet analysis, or the Z+jet analysis, will be described.

4.1.1 Data and Monte Carlo samples

Real data used in this work was collected by ATLAS from March 13 to April 29 2011. Only the data taken under stable beam conditions, when all sub-parts of the detector were fully operational, and which was triggered by the EF_TAU29_MEDIUM_XE35NOMU trigger for the $W(\rightarrow \tau\nu)$+jet analysis, and EF_TAU16_LOOSE_MU15 trigger for the $Z(\rightarrow \tau\tau)$+jet analysis, was considered. The amount of data taken under these conditions corresponds to the integrated luminosity of $\mathcal{L}_{\mathrm{int}} = 161\ \mathrm{pb}^{-1}$. This data is compared to signal and electroweak background Monte Carlo and QCD background estimated using data driven methods. The list of the Monte Carlo samples used in this work is shown in table 4.1. All Monte Carlo samples were produced by the ATLAS Collaboration. All γ^*/Z samples include a mass cut of $M_{\gamma^*/Z}$ = 66-116 GeV. The cross section values (68) in table 4.1 are based on the NNLO predictions, obtained by using the FEWZ simulation code (69). The reference signal Monte Carlo is chosen to be the Alpgen Monte Carlo due to the reasons discussed in the section 2.3.

The PDF's used in the Monte Carlo generators were MRST LO* (70) in Pythia6, CTEQ6.6 (71) in MC@NLO, and CTEQ6ll (72) in Alpgen.

MC sample	Generator	Events	Cross Section [nb]
$W \to \tau\nu$ (incl.)	Pythia6	1997438	10.46 ± 0.52
$W \to e\nu$ (incl.)	Pythia6	3594567	10.46 ± 0.52
$W \to \mu\nu$ (incl.)	Pythia6	6965567	10.46 ± 0.52
$\gamma^*/Z \to \tau\tau$ (incl.)	Pythia6	1668044	0.99 ± 0.05
$\gamma^*/Z \to ee$ (incl.)	Pythia6	1668044	0.99 ± 0.05
$\gamma^*/Z \to \mu\mu$ (incl.)	Pythia6	4969134	0.99 ± 0.05
$t\bar{t}$ (at least 1 lept.)	MC@NLO	7809494	0.089 ± 0.005
$t\bar{t}$ (full had.)	MC@NLO	1049008	0.071 ± 0.004
$W(\to \tau\nu)$+0Partons	Alpgen	3259564	8.31 ± 0.38
$W(\to \tau\nu)$+1Parton	Alpgen	2496467	1.56 ± 0.04
$W(\to \tau\nu)$+2Partons	Alpgen	3764804	0.45 ± 0.02
$W(\to \tau\nu)$+3Partons	Alpgen	1008514	0.122 ± 0.004
$W(\to \tau\nu)$+4Partons	Alpgen	248864	0.030 ± 0.001
$\gamma^*/Z(\to \tau\tau)$+0Partons	Alpgen	6608784	0.80 ± 0.01
$\gamma^*/Z(\to \tau\tau)$+1Parton	Alpgen	1302677	0.161 ± 0.005
$\gamma^*/Z(\to \tau\tau)$+2Partons	Alpgen	373869	0.048 ± 0.001
$\gamma^*/Z(\to \tau\tau)$+3Partons	Alpgen	109947	0.0135 ± 0.0002
$\gamma^*/Z(\to \tau\tau)$+4Partons	Alpgen	29977	0.00034 ± 0.00005

Table 4.1: Monte Carlo samples used in this analysis. Every generator uses Tauola package to simulate the decay of the taus. Every sample is produced with an average of 8 pileup interactions per event.

Since the number of the average pile-up events, differs in Monte Carlo and in real data, the events in Monte Carlo are reweighted in order to obtain similar pile-up conditions. To do this, the average number of interactions per bunch crossing, $\langle\mu\rangle$, is introduced. In data it is estimated as the number of counted events per a time period of one lumiblock, which takes approximately one minute, over the total number of bunch crossings in the lumiblock. The distribution of $\langle\mu\rangle$ in real data is shown in figure 4.1. The Monte Carlo events are then reweighted, so that on average, the distribution of the number of interactions per Monte Carlo event, μ^{MC}, corresponds to the distribution of $\langle\mu\rangle$ in data. The distributions of μ^{MC} before and after the reweighting is shown in figure 4.2.

In every event it is required to have at least 1 primary vertex, with at least four associated tracks. It is applied as a prevention against non-collision background, such as cosmic muon events. Using the Monte Carlo, this requirement is estimated to have only a small impact on the signal efficiency since it rejects around 0.8 % of the signal

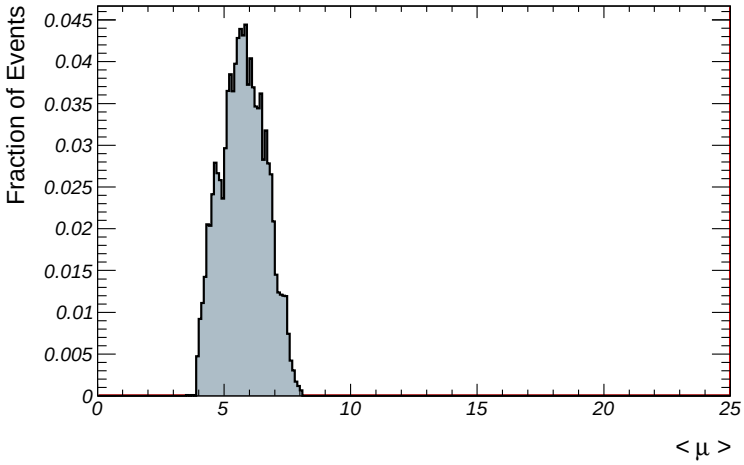

Figure 4.1: The distribution of the average number of interactions per bunch crossing, $\langle\mu\rangle$, obtained from data events, triggered by the EF_TAU29_MEDIUM_XE35NOMU trigger.

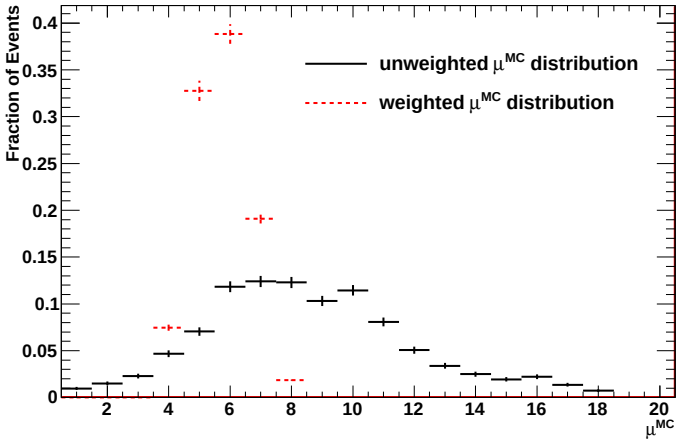

Figure 4.2: μ^{MC} distributions in Pythia $W \to \tau\nu$ Monte Carlo, in the events triggered by the EF_TAU29_MEDIUM_XE35NOMU trigger, before (full, black), and after (dashed, red) the pile-up reweighting.

events in both $W(\rightarrow \tau\nu)$+jet and $Z(\rightarrow \tau\tau)$+jet analyses. Later on, it is referred to as the **vertex requirement**.

Some features of the data are hard to simulate in Monte Carlo. Among them are rare detector problems that can show up as large energy deposits in a single, or a cluster of, calorimeter cell(s), the so-called hot towers. Hot towers are not directly related to the collisions, but can be caused by discharges in the electronics, or by cosmic muon background (73). The presence of hot towers in the events can corrupt e.g. the measured $E_{\mathrm{T}}^{\mathrm{Miss}}$ in the event, or can produce fake jets. In order to avoid this, the so-called **Jet Cleaning** is applied, where events containing fake jets are excluded. The Jet Cleaning rejects approximately 0.2% of the data, and is not assumed to have an effect on the efficiency of the signal. After considering these detector problems, the data can be described accurately by the Monte Carlo (73), and object distributions, such as jet p_{T} (see figure 4.3), show a good agreement between data and Monte Carlo.

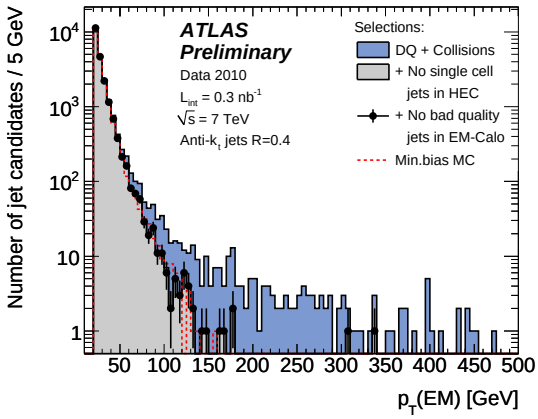

Figure 4.3: Inclusive anti-$k_{\mathrm{t}}04$ jet p_{T} distribution at the EM scale before and after the cleaning cuts. The minimum bias Monte Carlo is scaled to the number of jets in the data (73).

4.1.1.1 QCD background

Due to a limited statistics of QCD background Monte Carlo, the QCD background needs to be estimated using data driven methods. A widely used method for the QCD background estimation in a data-driven way is the so-called **ABCD** method. Two variables, X and Y, which are assumed to be uncorrelated and which can separate the

QCD multijet background from the signal, are used. Applying the combinations of the cuts X $> X_I$ and Y $> Y_I$, the signal region A is defined, while all other combinations define a QCD enhanced and signal suppressed control regions B, C and D, as illustrated in figure 4.4. The number of the QCD background events in the signal region A, N^A_{QCD},

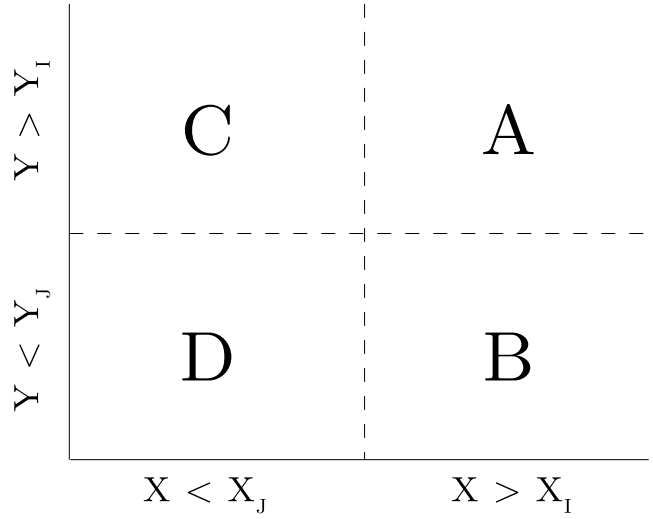

Figure 4.4: A schematic description of the A, B, C, and D control regions. The control region A is referred to as the signal control region, while the QCD background enhanced regions are B, C and D. The variables X and Y are two independent variables with high separation power between the signal and the QCD background.

can be expressed using the number of the background events N^B_{QCD}, N^C_{QCD}, and N^D_{QCD}, in the background control regions as:

$$N^A_{\mathrm{QCD}} = N^B_{\mathrm{QCD}} \frac{N^C_{\mathrm{QCD}}}{N^D_{\mathrm{QCD}}}. \tag{4.2}$$

In order to correct for the non-QCD contributions in the regions B, C and D, these contributions are subtracted. The number of QCD background events in the regions B, C and D is expressed as:

$$N^i_{\mathrm{QCD}} = N^i_{\mathrm{Data}} - N^i_{\mathrm{EWbckg}} - N^i_{\mathrm{signal}}, i = B, C, D, \tag{4.3}$$

where the N^i_{Data} is the number of data events in the control region i, N^i_{EWbckg} is the electroweak background, and N^i_{signal} is the number of the signal events in the background control regions. Both N^i_{signal} and N^i_{EWbckg} are estimated from the Monte

Carlo.

4.1.2 Common selection in the tau decay channel

The selected taus from the $W(\rightarrow \tau\nu)$+jet events are required to decay hadronicaly since this decay mode has the largest branching ratio. The hadronic decay of the tau is also chosen due to the backgrounds from either $W(\rightarrow e\nu)$ or $W(\rightarrow \mu\nu)$ events, which would be dominant if making this analysis in the lepton decay mode of the taus.

The $Z(\rightarrow \tau\tau)$+jet analysis is carried out for the $\tau\tau \rightarrow \mu\tau_{\text{had}}$ final state, due to a clean signature and a relatively high branching fraction[1].

In the $W(\rightarrow \tau\nu)$+jet analysis, the event signature will contain one hadronicaly decaying tau, missing transverse energy and at least one jet. In the $Z(\rightarrow \tau\tau)$+jet analysis, the final state contains one hadronicaly decaying tau, one muon and at least one jet. The common selection of both analyses therefore includes the selection of the tau and the jet, and will be different in the muon and missing transverse energy selection.

The **tau selection** in both $W(\rightarrow \tau\nu)$+jet and $Z(\rightarrow \tau\tau)$+jet analyses uses reconstructed tau candidates with $|\eta| < 2.47$ (tau candidates from the transition region $1.37 < |\eta| < 1.52$, between the barrel and the end-cap calorimeter, are ignored) and transverse momentum $p_{\text{T}} > 20$ GeV. For the tau identification, medium BDT ID is used, which includes medium BDT jet score (BDTJetScore > 0.67 for one-prong, and BDTJetScore > 0.55 for multi-prong), and medium BDT electron veto (BDTEleScore > 0.51). It is required to have exactly one selected tau in the event.

The selected tau has to have either **one or three associated tracks**. Also, the selected tau has to be **trigger matched** to the corresponding EF tau trigger object, for which ΔR between the trigger tau and the selected tau is smaller than 0.4.

The **jet selection** starts from all jets in the event reconstructed by the anti$-k_{\text{t}}04$ algorithm. Every jet is required to have $p_{\text{T}} > 30$ GeV, and $|\eta| < 2.8$. The jet has to be isolated from the selected tau by requiring $\Delta R^{\text{jet},\tau} > 0.6$. At least one jet is required in every event.

[1] In the inclusive $Z \rightarrow \tau\tau$ cross section measurement (65), the $\tau_\mu\tau_{\text{had}}$ channel had the highest acceptance, and the lowest relative statistical uncertainty.

4.1.3 Object and Event Selection in the W+jet analysis

In order to select the $W(\rightarrow \tau\nu)$+jet events and keeping the background small, additional selection cuts to the common selection cuts are applied. The background processes found to give non-negligible contributions were: QCD multijet background, $Z \rightarrow \tau\tau$, $W \rightarrow e\nu$, $W \rightarrow \mu\nu$ and $t\bar{t}$ events, where all can include additional jets in the final state. The additional selection cuts are:

Trigger: A crucial part of the event preselection provides already the trigger. The EF_TAU29_MEDIUM_XE35_NOMU trigger requires to have a medium EF tau candidate with a transverse momentum of at least 29 GeV, and a missing energy at EF of at least 35 GeV. This was the lowest unprescaled trigger during the data taking, sensitive to the given event signature.

Transverse Momentum of the Tau: In order to reduce the trigger bias on the selected tau coming from the tau trigger requirement EF_TAU29_MEDIUM, a cut on the transverse momentum of the selected tau, $p_{\mathrm{T}}^{\tau} > 35$ GeV, is applied. This threshold roughly corresponds to the end of the trigger turn-on region, as shown in figure 4.5, that shows the trigger efficiency of the EF_TAU29_MEDIUM trigger as a function of the offline tau p_{T}.

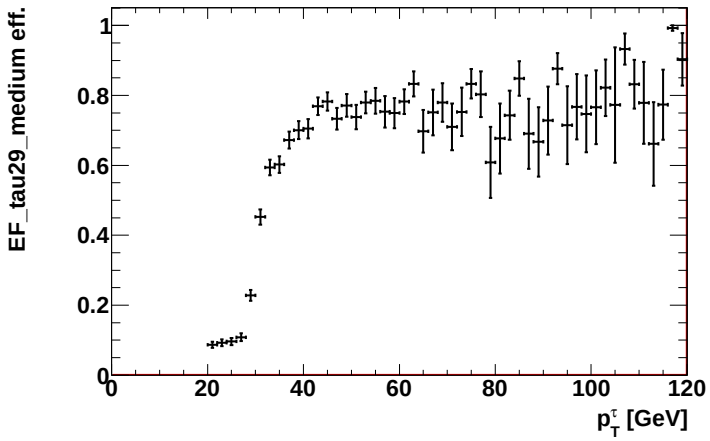

Figure 4.5: EF_TAU29_MEDIUM efficiency curve as a function of the selected tau transverse momentum. The efficiency curve is done using the $W \rightarrow \tau\nu$ Alpgen Monte Carlo. Full offline selection as described in table 4.2 is applied, but as the trigger, only the EF_XE35_NOMU trigger is applied.

Angular separation An effective method how to reject the QCD background is to cut on the ϕ angle between the selected tau and the missing transverse energy, $\Delta\phi^{\tau}_{E_{\mathrm{T}}^{\mathrm{Miss}}}$:

$$\Delta\phi^{\tau}_{E_{\mathrm{T}}^{\mathrm{Miss}}} = \phi^{\tau} - \phi_{E_{\mathrm{T}}^{\mathrm{Miss}}}, \tag{4.4}$$

where ϕ^{τ} is the ϕ coordinate of the selected tau, and $\phi_{E_{\mathrm{T}}^{\mathrm{Miss}}}$ is the ϕ coordinate of the missing transverse energy. The $\left|\Delta\phi^{\tau}_{E_{\mathrm{T}}^{\mathrm{Miss}}}\right|$ distribution for the signal and the QCD background is shown in figure 4.6.

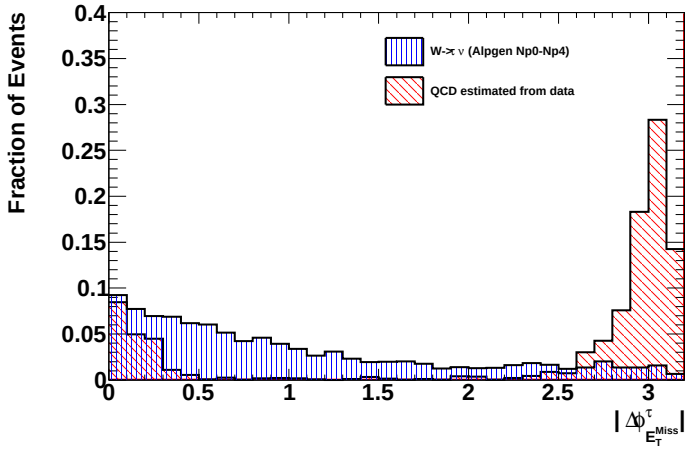

Figure 4.6: $\left|\Delta\phi^{\tau}_{E_{\mathrm{T}}^{\mathrm{Miss}}}\right|$ distribution for the QCD background and signal Monte Carlo after the full selection described in table 4.2 (the $\Delta\phi^{\tau}_{E_{\mathrm{T}}^{\mathrm{Miss}}}$ cut is not applied). The QCD background shape is extracted from data by defining a QCD background enhanced region by applying a "looser" tau ID, as explained in the later section 4.1.3.1.

Figure 4.6 shows that in the QCD background events, the $E_{\mathrm{T}}^{\mathrm{Miss}}$ points likely either in the same or in the exact opposite direction as the selected (fake) tau. Since the QCD dijet events consist of two back-to-back QCD jets, the $E_{\mathrm{T}}^{\mathrm{Miss}}$ occurs due to a measured im-balance in the energies of the two QCD jets. To reject most of the QCD background events, a symmetric cut, $0.3 < \left|\Delta\phi^{\tau}_{E_{\mathrm{T}}^{\mathrm{Miss}}}\right| < \pi - 0.3$, is applied.

Lepton Veto: In order to suppress the electroweak background from $W \to \mu\nu$ and $W \to e\nu$ decays, events with a light lepton, a combined muon or a medium electron, with p_{T} greater than 15 GeV are rejected. The p_{T} distribution of the hardest light lepton, for signal, $W \to \mu\nu$, and $W \to e\nu$ events, is shown shown in figure 4.7. Applying

this cut, a rejection of ∼60-80% of events with true electrons or muons is observed, while having an effect of less than 5% on the signal.

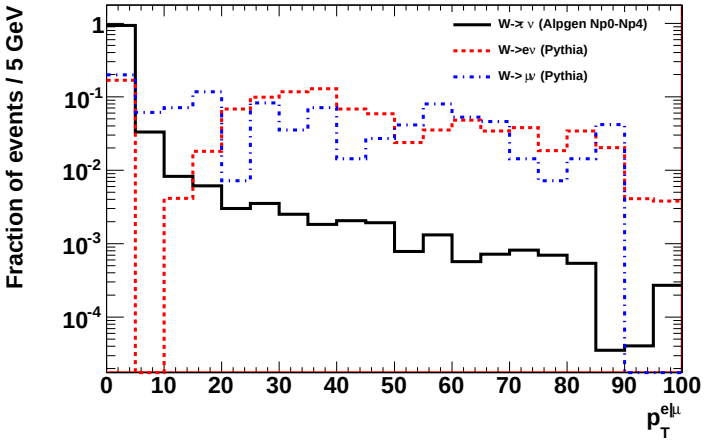

Figure 4.7: Transverse momentum of the selected leading light lepton (combined muon or medium electron), after the offline selection from table 4.2, except the cuts on $S_{E_{\mathrm{T}}^{\mathrm{Miss}}}$, Angular separation and Lepton veto.

Missing Transverse Energy Significance: A cut on the Missing Transverse Energy Significance, $S_{E_{\mathrm{T}}^{\mathrm{Miss}}}$, is applied, to separate the signal from the QCD background. Even in events with no true $E_{\mathrm{T}}^{\mathrm{Miss}}$, uncertainties can give rise to a non-zero $E_{\mathrm{T}}^{\mathrm{Miss}}$ in the events, as it can be seen e.g. in figure 3.31, where a non-zero $E_{\mathrm{T}}^{\mathrm{Miss}}$ in $Z \rightarrow ee$ events can be observed. Therefore, $S_{E_{\mathrm{T}}^{\mathrm{Miss}}}$ is defined as the ratio of $E_{\mathrm{T}}^{\mathrm{Miss}}$ (in GeV) and its resolution, which to a good approximation scales as $a \times \sqrt{\sum E_{\mathrm{T}}[GeV]}$, where the scaling parameter a was estimated as $a = 0.5[\sqrt{GeV}]$ (74):

$$S_{E_{\mathrm{T}}^{\mathrm{Miss}}} = \frac{E_{\mathrm{T}}^{\mathrm{Miss}}}{0.5[\sqrt{GeV}]\sqrt{\sum E_{\mathrm{T}}}}. \tag{4.5}$$

Figure 4.8 shows, the comparison of $E_{\mathrm{T}}^{\mathrm{Miss}}$ and $\sqrt{\sum E_{\mathrm{T}}}$ in a correlation plot for the QCD background and the $W(\rightarrow \tau\nu)$+jet events. A cut of $S_{E_{\mathrm{T}}^{\mathrm{Miss}}} > 6$ is chosen in order to have an acceptable signal efficiency and high QCD background rejection. The $S_{E_{\mathrm{T}}^{\mathrm{Miss}}}$ distribution for signal and QCD background is shown in figure 4.9.

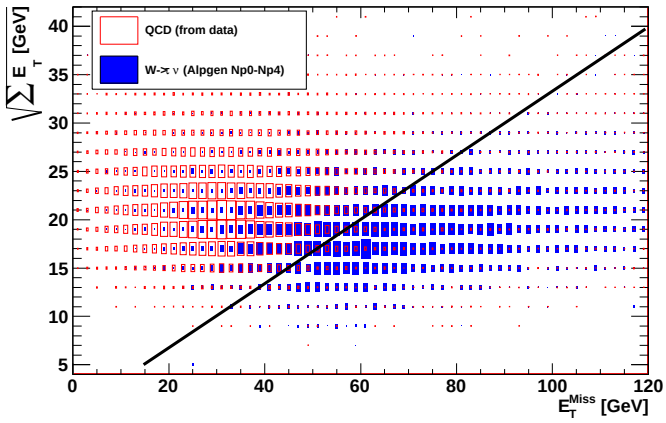

Figure 4.8: A correlation plot of $E_{\mathrm{T}}^{\mathrm{Miss}}$ and $\sqrt{\sum E_{\mathrm{T}}}$, in the W($\rightarrow \tau\nu$)+jet analysis, after the trigger requirement, tau selection (including the tau track multiplicity and p_{T} requirements) and the jet selection, as defined in table 4.2. The event selection in this figure does not include the cut on the angular separation, lepton veto and $S_{E_{\mathrm{T}}^{\mathrm{Miss}}}$. The blue boxes represent the signal, while the red boxes represent the QCD background. The QCD background is obtained from data, by using a looser requirement on the tau ID, as described in the later section 4.1.3.1. The black line shows the cut on $S_{E_{\mathrm{T}}^{\mathrm{Miss}}}$.

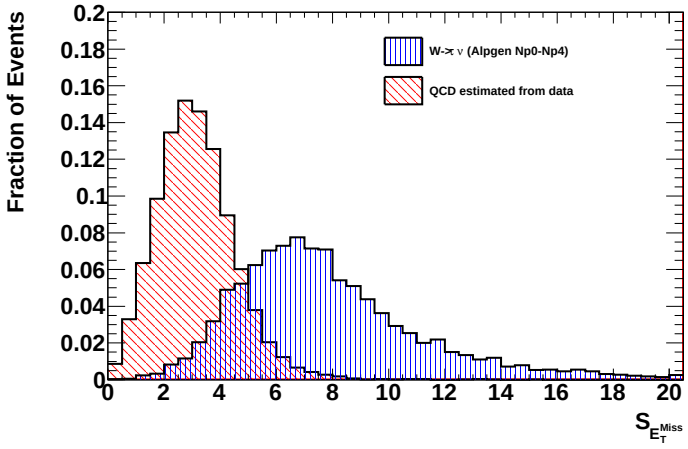

Figure 4.9: The $S_{E_{\mathrm{T}}^{\mathrm{Miss}}}$ distribution for the selected signal and the QCD background. The selection of the tau (including the tau track multiplicity and p_{T} requirements) and the jet, as described in table 4.2, is applied. The cut on angular separation, lepton veto and $S_{E_{\mathrm{T}}^{\mathrm{Miss}}}$ itself is not applied. The QCD distribution is taken from data, by defining a QCD enhanced region, by using a looser requirement on the tau ID, as described in the section 4.1.3.1.

4.1.3.1 Selected events in the $W(\rightarrow \tau\nu)$+jet analysis

The full selection used in the $W(\rightarrow \tau\nu)$+jet analysis is summarized in table 4.2. Applying the selection from table 4.2, the number of the passed data events, the number of the signal events estimated from the Alpgen Monte Carlo, the number of the passed EW background events estimated from Pythia and MC@NLO Monte Carlo, the number of estimated QCD background events, and the total background, for the integrated luminosity $\mathcal{L}_{\mathrm{int}} = 161\ \mathrm{pb}^{-1}$, is summarized in table 4.3, in the column denoted as region A.

Trigger
EF_TAU29_MEDIUM_XE35_NOMU
Vertex
Jet Cleaning
Tau Selection
$p_{\mathrm{T}} > 20$ GeV
$\lvert\eta\rvert < 2.47$, not considering taus from $1.37 < \lvert\eta\rvert < 1.52$
BDT medium
Exactly one selected tau
Trigger Matched Tau
$\Delta R^{\tau_{\mathrm{OL}},\tau_{\mathrm{EF}}} < 0.4$
Transverse Momentum of the Tau
$p_{\mathrm{T}} > 35$ GeV
Tau Number of Tracks 1 or 3
Selected Jet
$p_{\mathrm{T}} > 30$ GeV
$\lvert\eta\rvert < 2.8$
$\Delta R^{\tau,\mathrm{jet}} > 0.6$
At least one selected jet
Angular separation
$0.3 < \left\lvert\Delta\phi^{\tau}_{E_{\mathrm{T}}^{\mathrm{Miss}}}\right\rvert < \pi - 0.3$
Lepton Veto
Missing Transverse Energy Significance
$S_{E_{\mathrm{T}}^{\mathrm{Miss}}} > 6$

Table 4.2: Summary of all the cuts used in the $W(\rightarrow \tau\nu)$+jet analysis.

The QCD background was estimated using the ABCD method. The background control regions were defined by cutting on the $S_{E_{\mathrm{T}}^{\mathrm{Miss}}}$ variable, and the BDTJetScore of the preselected tau. The regions A, B, C, and D were defined as:

- **A** - All selection cuts as described in table 4.2 were applied

- **B** - The selection cuts as described in table 4.2 were applied, but the tau selection criteria was changed, and a "looser" tau selection, $0.15 < \text{BDTJetScore} < 0.45$, was applied.
- **C** - The selection cuts as described in table 4.2 were applied, but the $S_{E_{\mathrm{T}}^{\mathrm{Miss}}}$ cut was changed, and $2 < S_{E_{\mathrm{T}}^{\mathrm{Miss}}} < 4.5$ was applied.
- **D** - The selection cuts as described in table 4.2 were applied, but with the requirement on the "looser" tau selection, and $2 < S_{E_{\mathrm{T}}^{\mathrm{Miss}}} < 4.5$.

This definition of the control regions has been chosen in order to decrease the contamination of the QCD background by the signal, in the QCD background enhanced regions B and C. The comparison of the BDT jet score and the $S_{E_{\mathrm{T}}^{\mathrm{Miss}}}$ distributions, for the QCD background in the control regions B and D, and C and D, is shown in figure 4.10. The comparison shows, that for the QCD background, the shape of the BDT jet score distribution is not affected by the definition of the $S_{E_{\mathrm{T}}^{\mathrm{Miss}}}$ cut, and at the same time, the shape of $S_{E_{\mathrm{T}}^{\mathrm{Miss}}}$ is not affected by the definition of the cut on the BDT jet score. Thus, these two variables are assumed in this work as uncorrelated.

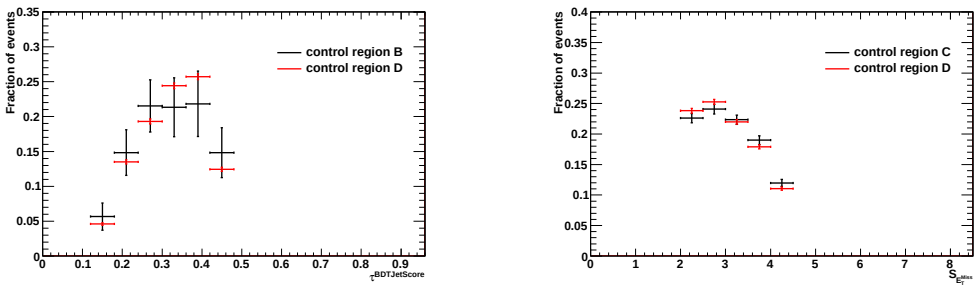

(a) (b)

Figure 4.10: The comparison of the BDT jet score (a) and $S_{E_{\mathrm{T}}^{\mathrm{Miss}}}$ (b) distributions in data in the QCD background enhanced regions. The EW and signal contamination is subtracted by using the Monte Carlo simulation.

The numbers of measured data events, estimated signal events, EW background events, and QCD background events, in the background dominated regions B, C and D, is shown in table 4.3. The number of the QCD background events in regions B, C and D is calculated using the equation 4.3. The uncertainties on the numbers of

selected signal and EW background events arise due to the limitations in the statistics of the Monte Carlo samples. The uncertainty on the QCD background estimation, as well as the uncertainty on the total background, combines the statistical uncertainty from data and the uncertainty from the limited statistics of Monte Carlo.

Sample	region A	region B	region C	region D
Data	649	451	4091	15589
Signal	491.8 ± 5.5(MC)	90.1 ± 3.6(MC)	86.5 ± 2.9(MC)	10.9 ± 0.6(MC)
QCD	67.7 ± 5.9(stat.)	265.1 ± 22.9(stat.)	3972.9 ± 64.0(stat.)	15547.4 ± 124(stat.)
$W \to e\nu$	10.4± 1.7(MC)	63.9 ± 7.4(MC)	5.7 ± 1.2(MC)	16.6 ± 2.6(MC)
$W \to \mu\nu$	7.6 ± 1.1(MC)	12.5 ± 1.9(MC)	2.0 ± 0.7(MC)	2.1 ± 0.6(MC)
$Z \to \tau\tau$	34.4 ± 2.0(MC)	3.9 ± 0.8(MC)	10.7 ± 1.0(MC)	——
$t\bar{t}$	49.5 ± 0.3(MC)	15.1 ± 0.9(MC)	13.0 ± 0.6(MC)	9.6 ± 0.3(MC)
Total background	169.8 ± 6.5(stat.)	9.4 ± 4.1(stat.)	1278.4 ± 35.8(stat.)	1232.4 ± 35.1(stat.)

Table 4.3: Number of measured events in data, signal and background Monte Carlo events, and QCD background events. The uncertainties (MC) on the numbers of events estimated using Monte Carlo arise due to the limited statistics of the Monte Carlo, whereas the uncertainties labeled as (stat.) cover both statistical uncertainties from data and from Monte Carlo.

4.1.3.2 Comparison of data and the predicted signal+background in the W+jet analysis

The comparison of the Monte Carlo predicted signal, EW background and the estimated QCD background, with data is shown in figures 4.11 to 4.14, for the most important signatures of the selected $W(\to \tau\nu)$+jet events. All distributions of the estimated signal and background are normalized to the numbers in table 4.3. The shapes of the QCD background distributions are taken either from region B or region C (subtracting the signal and EW background), dependent whether there was an observed correlation of the plotted variables with either $S_{E_{\mathrm{T}}^{\mathrm{Miss}}}$ or tau BDT jet score in the QCD background events.

In figure 4.11 are the p_{T} and η distributions of the selected tau. The shape of the Monte Carlo distributions agrees well with the data distributions, showing a good understanding of modeling of the tau properties in Monte Carlo. In both Monte Carlo and data, drops in the bins between $|\eta| = 1.4$ to 1.8 are observed. These efficiency drops are expected, and are caused by the selection requirement on the taus to be outside of the η region $1.37 < |\eta| < 1.52$.

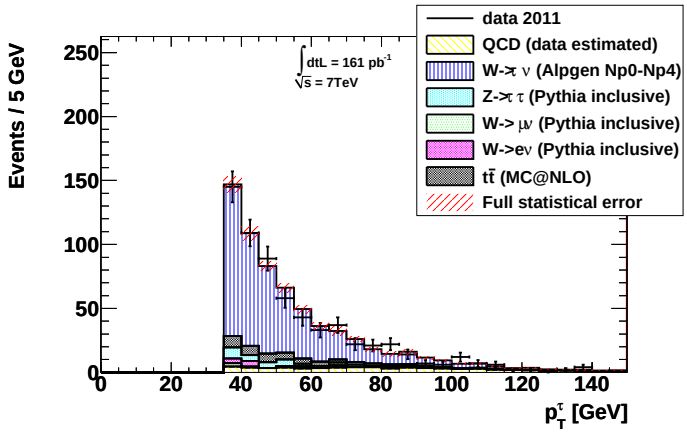

(a)

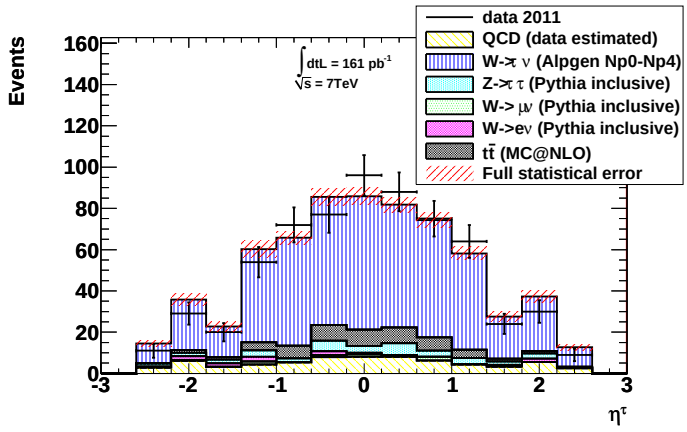

(b)

Figure 4.11: Distributions of the p_{T} (a) and η (b) of the selected tau, in the selected $W(\rightarrow \tau\nu)$+jet signal and background events, and in data, after the full $W(\rightarrow \tau\nu)$+jet selection described in table 4.2. The shape of the QCD background is taken from the control region C.

In figure 4.12 are the distributions of $E_{\mathrm{T}}^{\mathrm{Miss}}$ (a), $\sum E_{\mathrm{T}}$ (b) and $S_{E_{\mathrm{T}}^{\mathrm{Miss}}}$ (c). The cut on $E_{\mathrm{T}}^{\mathrm{Miss}}$ is fully dependent on the cut at the trigger level, coming from the requirement EF_xe35noMu. A fairly good agreement between data and signal+background prediction is observed in all distributions. In both $E_{\mathrm{T}}^{\mathrm{Miss}}$ and $\sum E_{\mathrm{T}}$ distributions a small difference between data and Monte Carlo is observed. However, no such difference appears in the $S_{E_{\mathrm{T}}^{\mathrm{Miss}}}$ distribution where a good agreement of data and Monte Carlo is observed for $S_{E_{\mathrm{T}}^{\mathrm{Miss}}} > 6$. To make sure that there is no unknown systematic effect affecting this analysis, which could be causing a small difference between data and Monte Carlo in the $E_{\mathrm{T}}^{\mathrm{Miss}}$ and the $\sum E_{\mathrm{T}}$ distributions similar to the observed one, data and Monte Carlo has been compared also for $S_{E_{\mathrm{T}}^{\mathrm{Miss}}} < 6$. This comparison is further described in the sections dedicated to the estimation of the systematic uncertainties.

Figure 4.13 shows the distributions of the angular separation, $\Delta\phi^{\tau}_{E_{\mathrm{T}}^{\mathrm{Miss}}}$ (a), and the transverse mass, M_{T}, calculated as $M_{\mathrm{T}} = \sqrt{2p_{\mathrm{T}}^{\tau}E_{\mathrm{T}}^{\mathrm{Miss}}(1-\cos\left(\Delta\phi^{\tau}_{E_{\mathrm{T}}^{\mathrm{Miss}}}\right))}$ (b). A very good agreement between data and the expected signal+background can be seen in both distributions. Figure 4.13 (a) shows that the majority of the QCD background lies in $\left|\Delta\phi^{\tau}_{E_{\mathrm{T}}^{\mathrm{Miss}}}\right| > 2.6$ rad. From the definition of M_{T} this also explains, why the majority of the QCD background in the M_{T} distribution is at rather high values, at $M_{\mathrm{T}} > 120$ GeV. The good agreement of data and the estimated QCD background (together with the Monte Carlo predicted signal and the EW background) in parts of the distributions where the QCD background is dominating (i.e. where $\left|\Delta\phi^{\tau}_{E_{\mathrm{T}}^{\mathrm{Miss}}}\right| > 2.6$ rad, and $M_{\mathrm{T}} > 120$ GeV), illustrates a good understanding of the QCD background in this analysis.

In figure 4.14 are the distributions of the p_{T}, track multiplicity and η of the leading jet in the selected $W(\rightarrow \tau\nu)$+jet events. A good agreement between data and the expected signal+background is observed.

4.1.4 Object and Event selection in the Z+jet analysis

The $Z(\rightarrow \tau\tau)$+jet selection is fully summarized in table 4.4. In order to reduce the background, which consists of $W \rightarrow \tau\nu$, $W \rightarrow \mu\nu$, $Z \rightarrow \mu\mu$, $t\bar{t}$ and QCD multijet background, the following cuts, in addition to the common selection, are applied:

Trigger: The trigger used for the $Z(\rightarrow \tau\tau)$+jet analysis is the combined trigger EF_tau16_loose_mu15. The trigger requires at EF a trigger tau with "loose" trigger identification requirements and $p_{\mathrm{T}} > 16$ GeV, and a trigger muon with $p_{\mathrm{T}} > 15$ GeV.

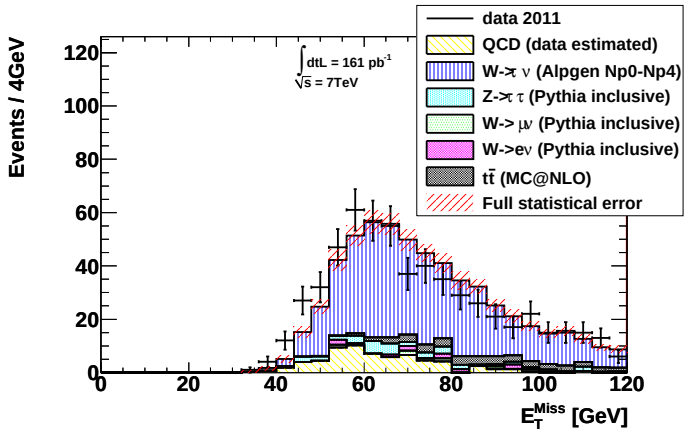

(a)

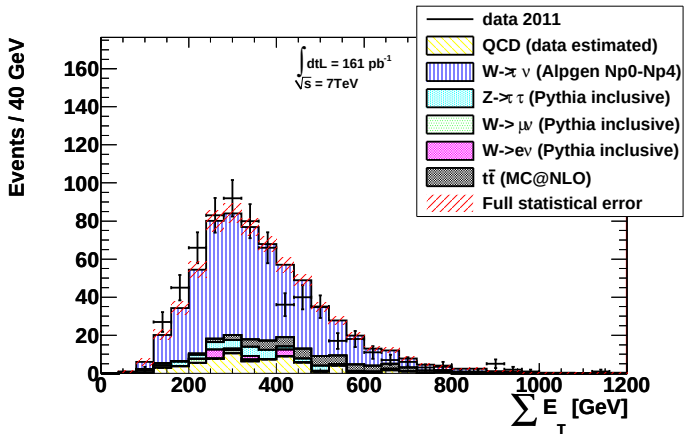

(b)

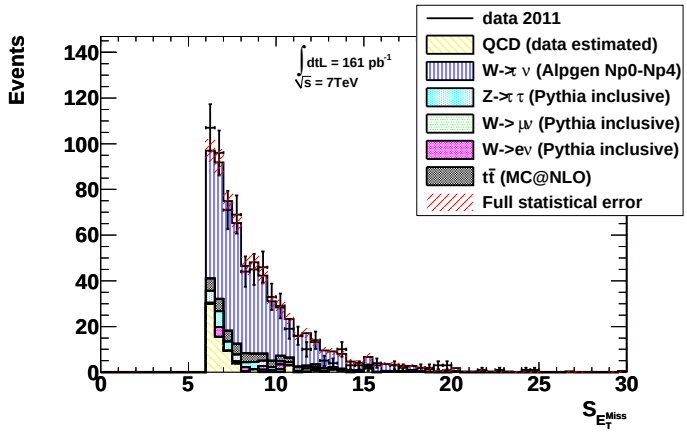

(c)

Figure 4.12: Distributions of $E_{\mathrm{T}}^{\mathrm{Miss}}$ (a), $\sum E_{\mathrm{T}}$ (b) and $S_{E_{\mathrm{T}}^{\mathrm{Miss}}}$ (c) in the selected $W(\rightarrow \tau\nu)$+jet signal and background events, and in data, after the full selection from table 4.2. The shape of the QCD background is taken from the control region B.

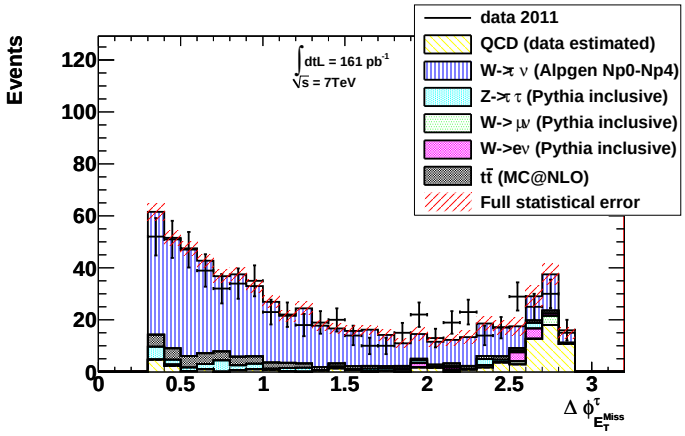

(a)

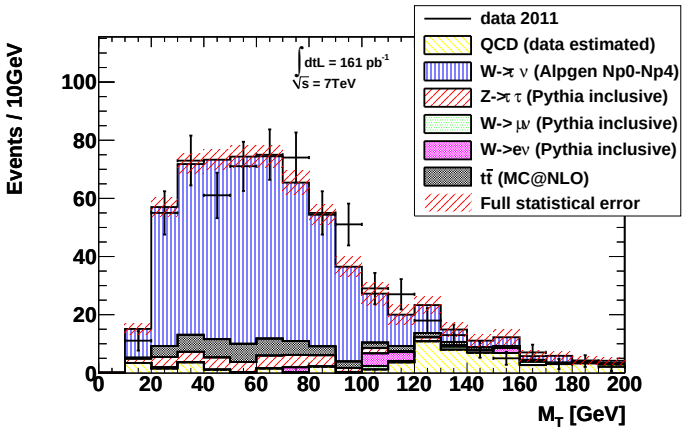

(b)

Figure 4.13: Distributions of $\left|\Delta\phi^{\tau}_{E_{\mathrm{T}}^{\mathrm{Miss}}}\right|$ (a) and M_{T} (b) in the selected $W(\rightarrow \tau\nu)$+jet signal and background events, and in data, after the full selection from table 4.2. The shape of the QCD background is taken from the control region B.

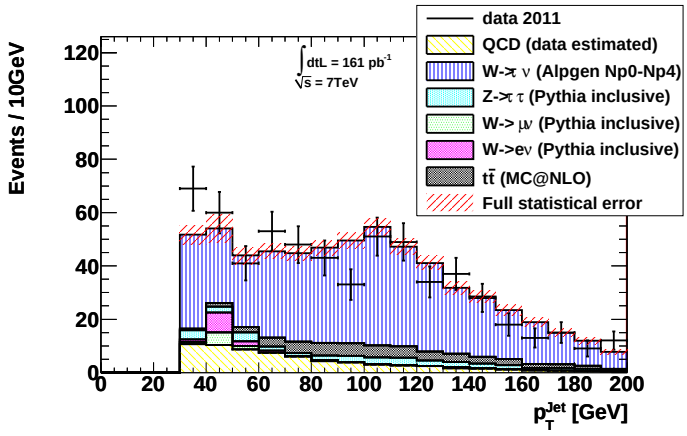

(a)

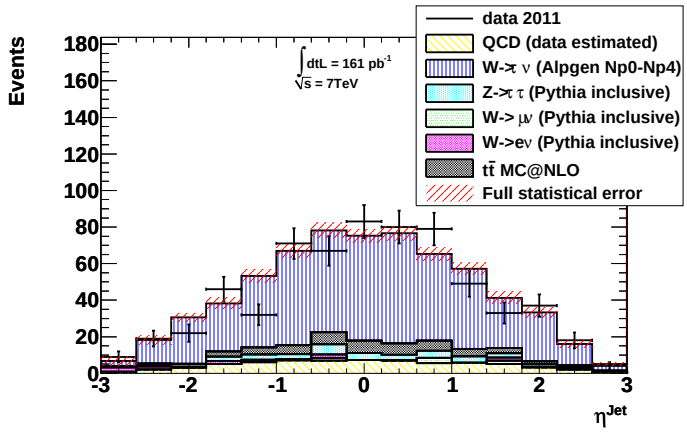

(b)

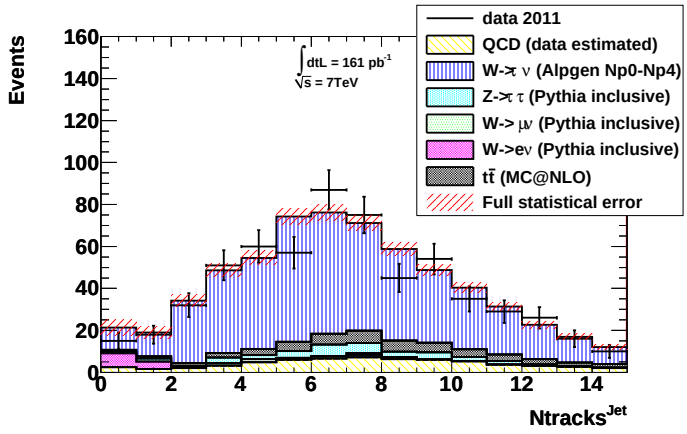

(c)

Figure 4.14: p_{T} (a), η (b), and track multiplicity (c) of the leading jet in the selected $W(\rightarrow \tau\nu)$+jet signal and background events, and in data, after the full selection described in table 4.2. The shape of the QCD background is taken from the control region C.

During the data taking, the EF_TAU16_LOOSE_MU15 trigger was the lowest unprescaled tau+mu trigger.

Muon Selection: The muons are selected from the combined MuID muon candidates. The muons are required to have p_{T} greater than 15 GeV. The inner detector track, which is associated to the muon spectrometer muon, is required to have at least one B layer hit, number of pixel hits at least two, number of SCT hits larger than five, and the longitudinal impact parameter, $|z_0|$, and the transverse impact parameter, $|d_0|$, smaller than 10 mm. Also, at least five hits are required in the TRT. This selection follows as similarly as possible the muon selection recommendation for the ATLAS detector described in (60).

Muon Isolation: To suppress muons appearing as a part of the QCD jets (mainly from semileptonic decays of c and b quarks), the selected muons are required to be isolated. The requirement on the muon isolation provides the strongest single contribution to the suppression of the QCD background. The variables $p_{\mathrm{T}}^{\mathrm{Cone40}}/p_{\mathrm{T}}^{\mu}$ and $E_{\mathrm{T}}^{\mathrm{Cone40}}/p_{\mathrm{T}}^{\mu}$ are used to require the isolation of the muon. $p_{\mathrm{T}}^{\mathrm{Cone40}}$ represents the sum of the transverse momenta of all charged particles in an isolation cone of $0.05 < \Delta R < 0.4$, centered around the selected muon direction. The ratio $p_{\mathrm{T}}^{\mathrm{Cone40}}/p_{\mathrm{T}}^{\mu}$, where p_{T}^{μ} is the transverse momentum of the selected muon, is required to be smaller than 0.05. $E_{\mathrm{T}}^{\mathrm{Cone40}}$ is the energy measured by the calorimeter in the isolation cone $0.05 < \Delta R < 0.4$, around the direction of the selected muon extrapolated from the inner detector to the calorimeter. $E_{\mathrm{T}}^{\mathrm{Cone40}}/p_{\mathrm{T}}^{\mu}$ smaller than 0.1 is required.

The distributions of $E_{\mathrm{T}}^{\mathrm{Cone40}}/p_{\mathrm{T}}^{\mu}$ and $p_{\mathrm{T}}^{\mathrm{Cone40}}/p_{\mathrm{T}}^{\mu}$ for signal Monte Carlo and QCD background are shown in figure 4.15 (a) and (b). The QCD shapes are taken from data, from a background dominated region, which is defined by requiring the cuts from table 4.4, but replacing the regular tau identification by a looser tau identification: 0.15 < BDTJetScore < 0.45. The shapes of the QCD distributions are taken from data, and the signal and EW background contaminations, estimated from Monte Carlo, are subtracted.

Both isolation cuts need to be applied because they complement each other. This is visible from figure 4.15 (c) which shows the correlation of $E_{\mathrm{T}}^{\mathrm{Cone40}}/p_{\mathrm{T}}^{\mu}$ and $p_{\mathrm{T}}^{\mathrm{Cone40}}/p_{\mathrm{T}}^{\mu}$ in the QCD background events.

Opposite sign charge: The QCD background can be further reduced by the requirement on the opposite sign charge between the selected muon and the selected

tau. While in $Z \rightarrow \tau\tau \rightarrow \tau_{\text{had}}\mu$ events, the charge of the muon and the tau have an opposite sign, figure 4.16 shows that the distribution of the charge product in the QCD background events is symmetric. The shape of the QCD dijet distribution in figure 4.16 is obtained from data by requiring the analysis cuts summarized in table 4.4, but without the requirement on the track multiplicity of the tau, without the requirement on the opposite sign charge, and with an inverted muon isolation requirement.

Dilepton Veto: A veto on two or more light leptons in the event is applied. This requirement minimizes mainly the background from the $Z(\rightarrow \mu\mu)$+jets events. Both muons and electrons are considered for the dilepton veto. The muon selection for the dilepton veto is looser than the selection of the signal muon described above. For the dilepton veto it is enough, that, in the event, there is at least one combined MuID muon with p_{T} above 15 GeV. Similarly for the electron selection, an electron is selected for the dilepton veto already in the case if it is a medium electron with p_{T} greater than 15 GeV. The dilepton veto has no effect on the signal, and additionally to the other cuts in table 4.4, it rejects approximately 30% of the $Z(\rightarrow \mu\mu)$ events.

Direction of $E_{\text{T}}^{\text{Miss}}$: This cut is applied in order to suppress the background from the $W(\rightarrow \mu\nu)$+jet and $W(\rightarrow \tau\nu)$+jet events. In the $Z(\rightarrow \tau\tau)$+jet events, the true $E_{\text{T}}^{\text{Miss}}$ comes from the neutrinos produced in the decays of the taus. Therefore, for the signal, $E_{\text{T}}^{\text{Miss}}$ will be aligned with the tau decay products and point in the inside of the angle between the selected tau and the selected muon, as illustrated in the picture 4.17 (a). In the $W(\rightarrow \mu\nu)$+jet and $W(\rightarrow \tau\nu)$+jet events, the neutrino from the W decay, and thus $E_{\text{T}}^{\text{Miss}}$, is pointing in the opposite direction of the muon (in the W rest frame) and thus in the outside of the azimuthal angle between the selected muon and the selected (fake) tau, as illustrated in the picture 4.17 (b). Therefore, a variable which is specifically sensitive to the direction of $E_{\text{T}}^{\text{Miss}}$ w.r.t. the directions of the selected tau and the selected muon is defined:

$$\sum \cos(\Delta\phi) = \cos(\phi^{\mu} - \phi^{E_{\text{T}}^{\text{Miss}}}) + \cos(\phi^{\tau} - \phi^{E_{\text{T}}^{\text{Miss}}}) \tag{4.6}$$

In the $Z(\rightarrow \tau\tau)$+jet events, the $\sum\cos(\Delta\phi)$ value is likelier to be positive, while in the W+jet background events, the value is likelier to be negative. This can be seen in figure 4.18 that compares the distribution of $\sum\cos(\Delta\phi)$ for the signal and the W+jet

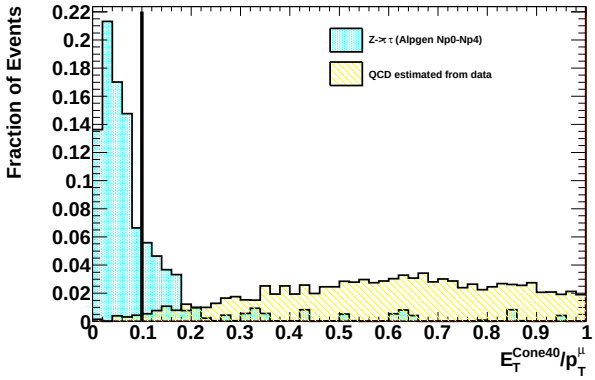

(a)

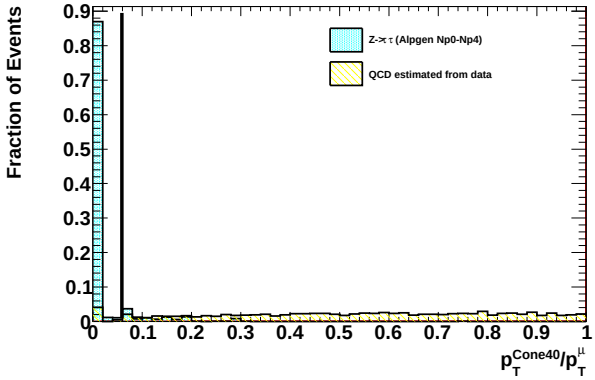

(b)

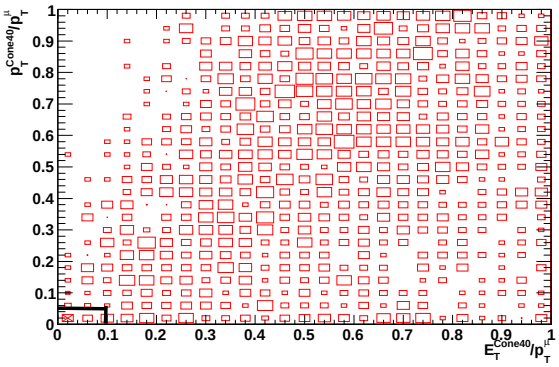

(c)

Figure 4.15: $E_{\mathrm{T}}^{\mathrm{Cone40}}/p_{\mathrm{T}}^{\mu}$ (a) and $p_{\mathrm{T}}^{\mathrm{Cone40}}/p_{\mathrm{T}}^{\mu}$ (b) of the selected muon for the signal and the QCD background obtained from data, by defining a QCD enhanced control region. The selection of the events includes the selection summarized in table 4.4, except the isolation itself, and applying a looser tau ID requirement. The black vertical lines indicate the cuts. The plot (c) shows the correlation of the isolation variables for the QCD background only, and the black box indicates the cuts.

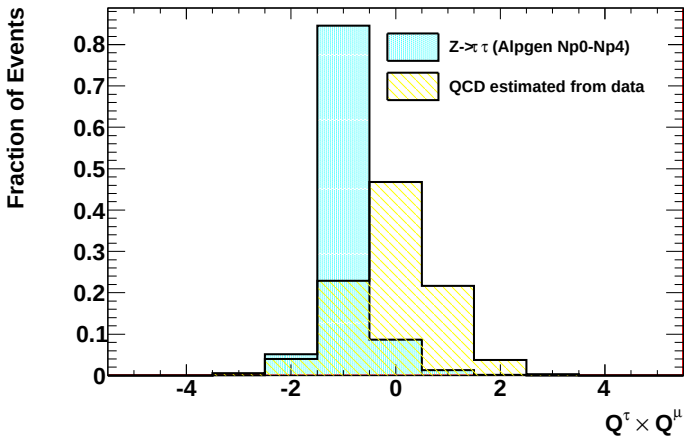

Figure 4.16: Distribution of the charge product of the selected muon and the selected tau in signal Monte Carlo and QCD background estimated from data. For the signal, all cuts from table 4.4 are applied, except the cuts on the opposite sign charge and the selected tau track multiplicity.

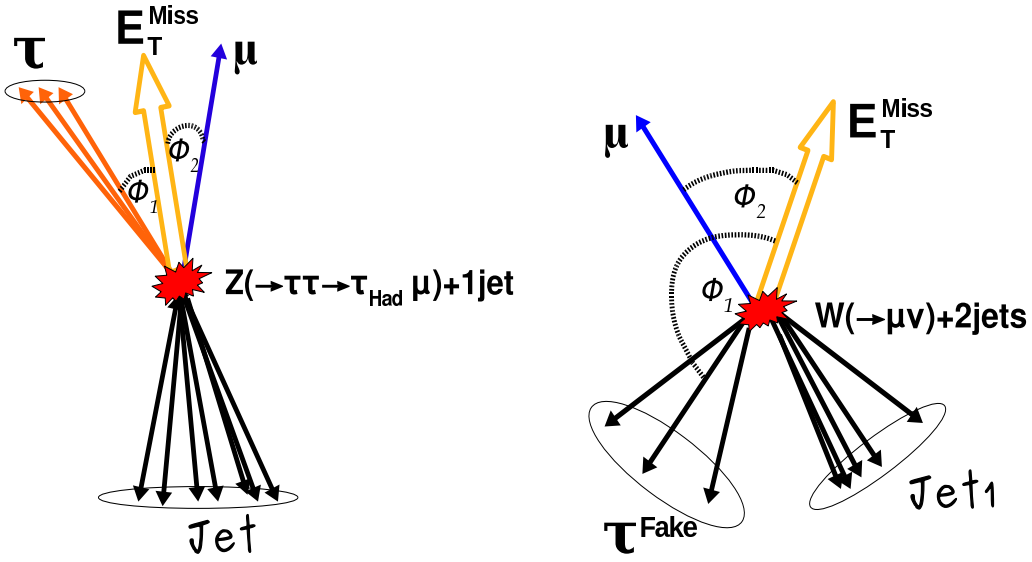

Figure 4.17: An illustration of a $Z(\rightarrow \tau\tau)$+jet event (a) and a $W(\rightarrow \mu\nu)$+2jets event (b), in the azimuthal plane. $\phi_1 = \phi^{\tau} - \phi^{E_T^{Miss}}$, and $\phi_2 = \phi^{\mu} - \phi^{E_T^{Miss}}$.

Monte Carlo. In order to minimize the rejection of the signal, a relatively loose cut of $\sum\cos(\Delta\phi) > -0.4$ has been applied.

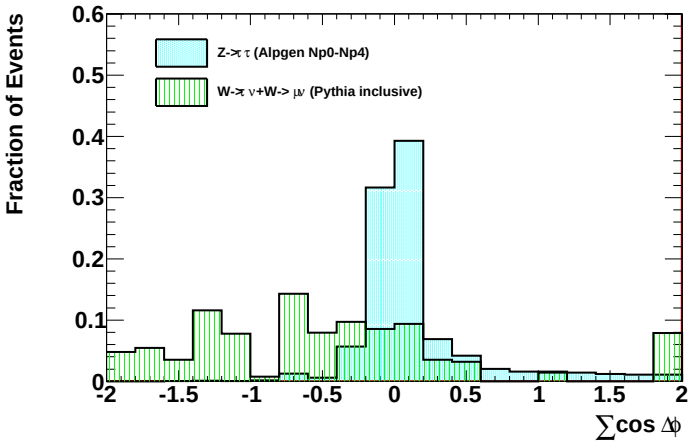

Figure 4.18: $\sum\cos(\Delta\phi)$ distribution for the signal and for the combined $W(\rightarrow \mu\nu)$ + $W(\rightarrow \tau\nu)$ Monte Carlo. The selection from table 4.4 is applied, except the current cut and the cut on the transverse mass. The high fluctuation of the background distribution is caused by the limited statistics in the Monte Carlo sample.

Transverse Mass: To provide an additional suppression of the $W(\rightarrow \mu\nu)$+jet events, an upper cut on the transverse mass, $M_{\mathrm{T}} < 50$ GeV, is applied. M_{T} is calculated as:

$$M_{\mathrm{T}} = \sqrt{2E_{\mathrm{T}}^{\mathrm{Miss}} p_{\mathrm{T}}^{\mu}(1-\cos(\Delta\phi^{\mu,E_{\mathrm{T}}^{\mathrm{Miss}}}))}, \tag{4.7}$$

where $E_{\mathrm{T}}^{\mathrm{Miss}}$ is the missing transverse energy, p_{T}^{μ} is the transverse momentum of the selected muon and $\phi^{\mu,E_{\mathrm{T}}^{\mathrm{Miss}}}$ is the azimuthal angle between $E_{\mathrm{T}}^{\mathrm{Miss}}$ and the muon. The M_{T} distribution after the selection (without applying the W suppression cuts), for signal and for W background Monte Carlo is shown in figure 4.19.

Applying the two W background suppression cuts, direction of $E_{\mathrm{T}}^{\mathrm{Miss}}$ cut and the transverse mass cut, an approximately 70-80% rejection of the W+jet events is achieved, while affecting the signal by only around 15%.

Visible Mass: A cut on the invariant mass of the visible decay products of the Z boson, M_{Vis}, is applied: 35 GeV $< M_{\mathrm{Vis}} <$ 75 GeV. Figure 4.20 shows the distribution of M_{Vis} for the signal and the combined EW background (including $t\bar{t}$). This cut

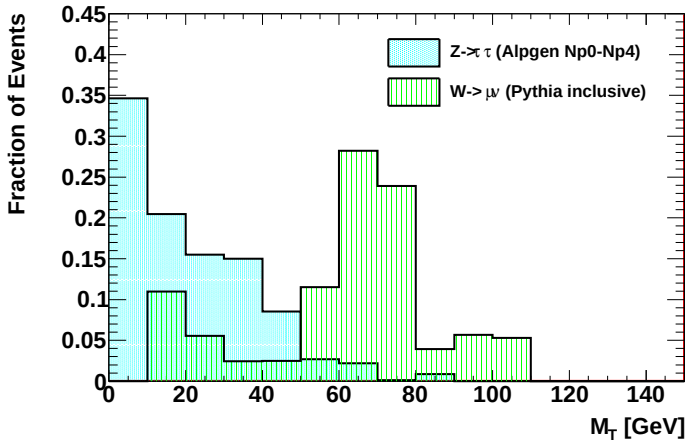

Figure 4.19: Transverse Mass distribution in signal and $W \to \mu\nu$ Monte Carlo after the selection described in table 4.4, without the cuts on the direction of $E_{\mathrm{T}}^{\mathrm{Miss}}$ and M_{T}.

provides a rejection of approximately 65-70% of the EW background at the top of all previously applied cuts, while rejecting only around 15% of the signal.

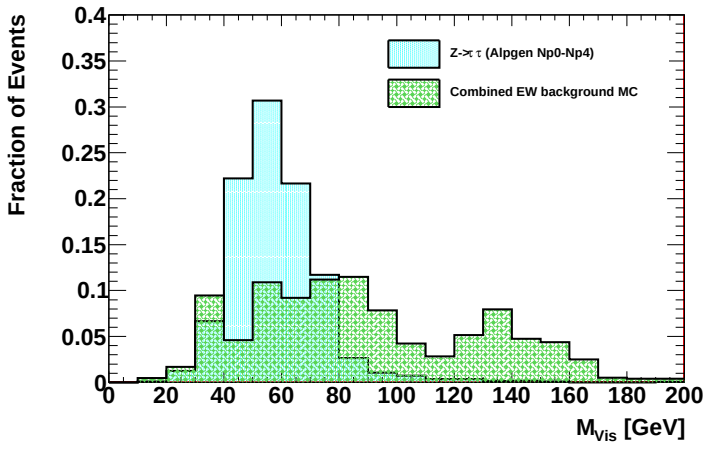

Figure 4.20: Distribution of the visible mass for signal and EW background Monte Carlo after the full selection described in table 4.4, without the cut on M_{Vis}.

4.1.4.1 Selected events in the $Z(\rightarrow \tau\tau)$+jet analysis

All cuts applied in the $Z(\rightarrow \tau\tau)$+jet analysis are summarized in table 4.4. The numbers of events passing this selection, for the integrated luminosity $\mathcal{L}_{\mathrm{int}} = 161$ pb^{-1}, in data, and for the estimated signal, EW background, and QCD background is shown in table 4.5, in column denoted as region A.

Trigger
EF_TAU16_LOOSE_MU15
Vertex
Jet Cleaning
Muon Selection
$p_{\mathrm{T}} > 15$ GeV , $\lvert\eta\rvert < 2.4$
Exactly one combined MuID muon
Muon Isolation
$E_{\mathrm{T}}^{\mathrm{Cone40}}/p_{\mathrm{T}}^{\mu} < 0.1$
$P_{\mathrm{T}}^{\mathrm{Cone40}}/p_{\mathrm{T}}^{\mu} < 0.05$
Tau Selection
$p_{\mathrm{T}} > 20$ GeV, $\lvert\eta\rvert < 2.47$, not considering taus from $1.37 < \lvert\eta\rvert < 1.52$
BDT medium
Exactly one selected tau
Trigger Matched Tau
$\Delta R^{\tau_{\mathrm{OL}},\tau_{\mathrm{EF}}} < 0.4$
Tau Number of Tracks 1 or 3
Opposite sign charge
Selected Jet
$p_{\mathrm{T}} > 30$ GeV, $\lvert\eta\rvert < 2.8$
$\Delta R^{\tau,\mathrm{jet}} > 0.6$
At least one selected jet
Dilepton Veto
No additional light lepton
Direction of $E_{\mathrm{T}}^{\mathrm{Miss}}$
$\cos(\phi^{\tau} - \phi^{E_{\mathrm{T}}^{\mathrm{Miss}}}) + \cos(\phi^{\mu} - \phi^{E_{\mathrm{T}}^{\mathrm{Miss}}}) > -0.4$
Transverse Mass
$M_{\mathrm{T}} < 50$ GeV
Visible Mass
35 GeV $< M_{\mathrm{Vis}} <$ 75 GeV

Table 4.4: Full cutflow in the Z+jet analysis in the tau decay channel.

The QCD multijet background is estimated using the ABCD method, as described in the section 4.1.1.1. The muon isolation requirement provides a powerful separation of the signal and the QCD background. Another separation of the signal and the QCD background, independent of the muon isolation, is the requirement on the opposite sign

charge of the tau and the muon. Therefore, to define the B, C and D control regions, the selection criteria on the charge product of the selected muon and the tau, and the muon isolation are used. The ABCD control regions are defined as:

- **A** - All signal selection cuts as described in table 4.4 are applied.
- **B** - All signal selection cuts except the requirement on the opposite sign charge (OS) are applied. The OS requirement is inverted, and same sign charge (SS) of the selected tau and the selected muon is required.
- **C** - All signal selection cuts are applied except the requirement on the muon isolation which is inverted. A non isolated muon, with $E_{\mathrm{T}}^{\mathrm{Cone40}}/p_{\mathrm{T}}^{\mu} > 0.1$ and $p_{\mathrm{T}}^{\mathrm{Cone40}}/p_{\mathrm{T}}^{\mu} > 0.05$, is required.
- **D** - All signal selection cuts are applied except the OS and the muon isolation criteria. A non isolated muon, with $E_{\mathrm{T}}^{\mathrm{Cone40}}/p_{\mathrm{T}}^{\mu} > 0.1$ and $p_{\mathrm{T}}^{\mathrm{Cone40}}/p_{\mathrm{T}}^{\mu} > 0.05$, and SS, are required.

Figure 4.21 shows a good agreement in the shapes of the isolation variables for OS and SS QCD background, showing that the isolation variables are independent on the charge product of the selected tau and muon.

Expression 4.3 from the chapter 4.1.1.1 is used to find the number of the QCD background events in the regions B, C, and D. The numbers of events in data, signal, and background, in the regions B, C and D, are summarized in table 4.5. The QCD background in region A is estimated using equation 4.2.

The large statistical uncertainty (in comparison to the number of estimated QCD background events) is caused by a very low statistics in the control region B. This region suffers from large EW background contamination and therefore relies on a good modeling of the EW background by the Monte Carlo. Although it is clear that within the uncertainty, the lower limit of the QCD background estimation can spread also into unphysical negative values, due to the fact that the QCD background is estimated to be small, both, the mean value and its uncertainty, are taken as such in further estimations.

To make sure that the EW background Monte Carlo is modeled accurately, an independent control region has been defined, that uses the full selection from table

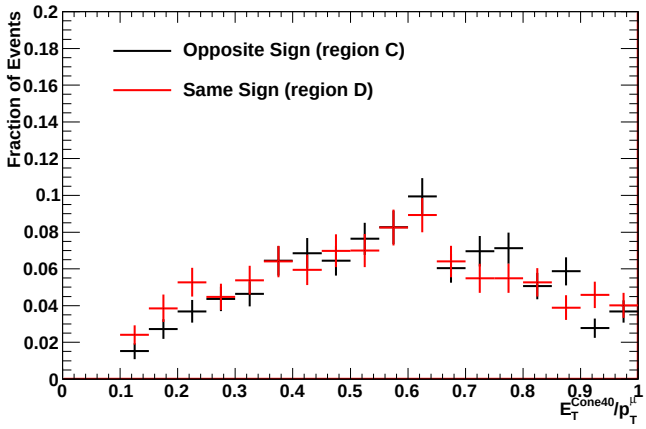

(a)

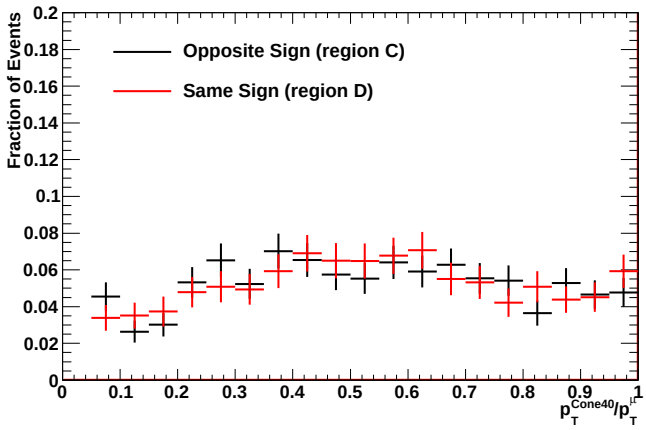

(b)

Figure 4.21: The QCD background distributions of $E_{\mathrm{T}}^{\mathrm{Cone40}}/p_{\mathrm{T}}^{\mu}$ (a) and $p_{\mathrm{T}}^{\mathrm{Cone40}}/p_{\mathrm{T}}^{\mu}$ (b). The QCD background is obtained from data, after subtracting the Monte Carlo EW background and signal. The shapes correspond to the QCD background shapes for the control regions C (black) and D (red).

Sample	region A	region B	region C	region D
Data	112	11	1286	1233
Signal	87.7 ± 1.3(MC)	1.3 ± 0.1(MC)	7.3 ± 0.4(MC)	0.5 ± 0.1(MC)
QCD	1.8 ± 3.9(stat.)	1.7 ± 3.7(stat.)	1269.9 ± 35.8(stat.)	1226.6 ± 35.1(stat.)
$Z \to \mu\mu$	2.9 ± 0.3(MC)	0.8 ± 0.1(MC)	0.5 ± 0.1(MC)	—
$W \to \mu\nu$	5.2 ± 0.9(MC)	4.2 ± 1.0(MC)	0.6 ± 0.4(MC)	—
$W \to \tau\nu$	2.2 ± 1.5(MC)	2.3 ± 1.4(MC)	—	1.1 ± 1.0
$t\bar{t}$	4.1 ± 0.1(MC)	0.40 ± 0.03(MC)	7.4 ± 0.2(MC)	4.7 ± 0.2(MC)
Total background	16.2 ± 4.3(stat.)	9.4 ± 4.1(stat.)	1278.4 ± 35.8(stat.)	1232.4 ± 35.1(stat.)

Table 4.5: Number of data events and the estimate of the QCD and EW (signal+background) events in the signal and background control regions. The number of QCD events is estimated by subtracting the EW contamination from the data events. The uncertainties (MC) come from the limited statistics of Monte Carlo, and the (stat.) uncertainties combine the statistical uncertainties from data and from Monte Carlo.

4.4, but uses an inverted cut on the transverse mass ($M_{\mathrm{T}} > 50$ GeV), and an inverted cut on the direction of $E_{\mathrm{T}}^{\mathrm{Miss}}$ ($\sum \cos(\Delta\phi) < -0.4$). In this way, a control sample is obtained, that is rich on the EW background, mainly $W \to \mu\nu$ and $W \to \tau\nu$. The QCD background contamination was estimated to be negligible and was not accounted. The distributions of p_{T} of the selected tau, M_{T} and $\sum \cos(\Delta\phi)$, for such selection, in data and in Monte Carlo, is shown in figure 4.22.

For the given selection, figure 4.22 demonstrates a good description (shape and the normalization) of the data by the $W \to \mu\nu$ and $W \to \tau\nu$ Monte Carlo and data. The overall difference between data and Monte Carlo has been found to be smaller than 2σ of the statistical deviation, therefore, no W background scale factors for the results shown in table 4.5 have been applied.

4.1.4.2 Comparison of data and the predicted signal+background in the Z+jet analysis

Figures 4.23 - 4.26 show the comparison of data and signal+background Monte Carlo (with the estimated QCD background) for the most important event variables in the $Z(\to \tau\tau)$+jet analysis. All signal and background distributions are normalized to the numbers in table 4.5 for region A, and the shapes of the QCD background distributions are taken from the control region C (from which the EW contamination is subtracted) with the specific non-isolation of the muon.

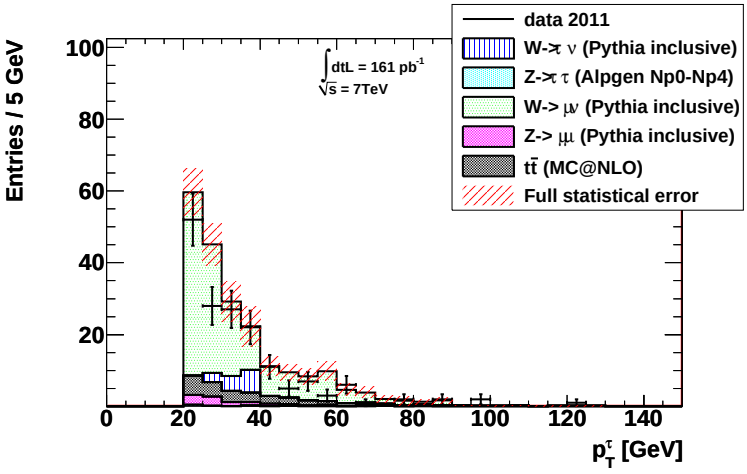

(a)

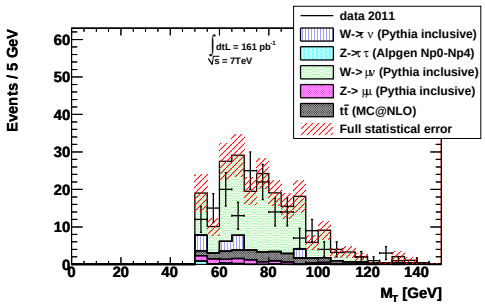

(b)

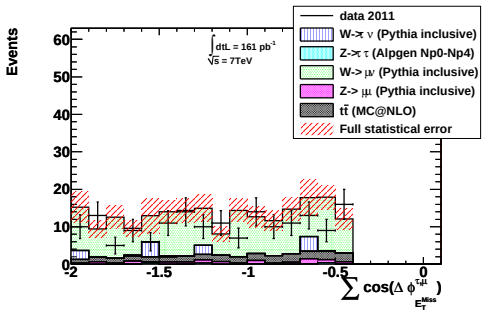

(c)

Figure 4.22: Distribution of p_{T} of the selected tau (a), M_{T} (b), and $\sum \cos(\Delta\phi)$ (c), in the W background enhanced control region. Full selection from table 4.4 is applied except the W suppression cuts (transverse mass and missing energy direction), which are for this particular case inverted, in order to enhance the W background.

Figures 4.23 to 4.25 show the quantities related to the Z boson and its decay products. Figure 4.26 shows the quantities of the leading jet in the $Z(\rightarrow \tau\tau)$+jet events, jet p_{T}, η and jet width, where the jet width represents an energy weighted measure of the spread of the clusters associated to the jet, w.r.t. the direction of the jet. A good agreement between data and the expected signal+background is observed in all distributions.

4.1.5 Cross section calculation

In order to interpret the observed events in terms of production cross sections of the $Z(\rightarrow \tau\tau)$+jet and $W(\rightarrow \tau\nu)$+jet processes, a reference phase-space referred to as the "full phase-space" is defined. The full phase-space to which the measurements will be extrapolated is defined in the means of the Monte Carlo simulation as:

- No phase-space restriction on the W and Z bosons.
- At least one accompanying truth anti$-k_{\mathrm{t}}04$ jet with the transverse momentum $p_{\mathrm{T}} > 30$ GeV, and inside the eta range $|\eta| < 2.8$.

Using the information about the cross sections from table 4.1, and using the Alpgen Monte Carlo signal samples, the theoretical prediction of the cross sections of $W(\rightarrow \tau\nu)$+jet and $Z(\rightarrow \tau\tau)$+jet is:

$$\sigma^{\mathrm{MC}}_{\mathrm{W+jet}} = 1.24 \pm 0.03(\text{cross section}) \text{ nb}, \tag{4.8}$$

$$\sigma^{\mathrm{MC}}_{\mathrm{Z+jet}} = 0.131 \pm 0.003(\text{cross section}) \text{ nb}, \tag{4.9}$$

where the uncertainties in 4.8 and 4.9 combine the partial $W(\rightarrow \tau\nu)$+N partons and $Z(\rightarrow \tau\tau)$+N partons cross section uncertainties and the effect of the limited Monte Carlo statistics.

From data, the full cross section, σ, and the fiducial cross section, σ^{fid}, which defines a cross section within a pre-defined fiducial region, are estimated. The fiducial cuts which define the fiducial region emulate at the generator level the event selection cuts. This allows in the cross section measurements to partially differentiate between the uncertainties related to the limits of the detector, and the theoretical uncertainties

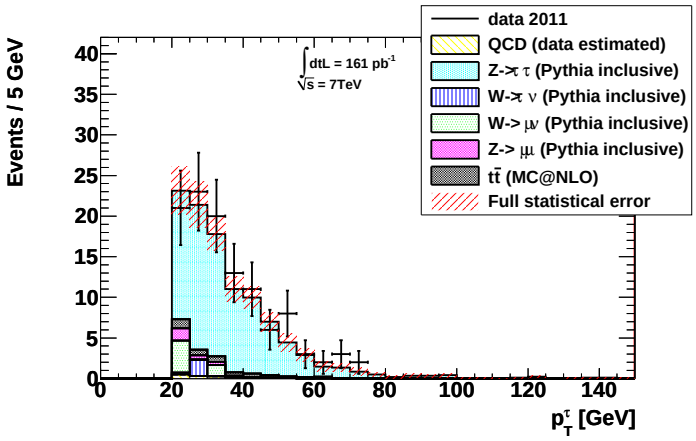

(a)

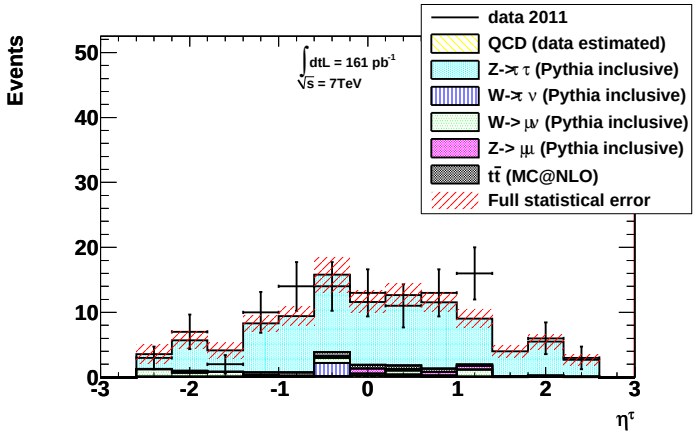

(b)

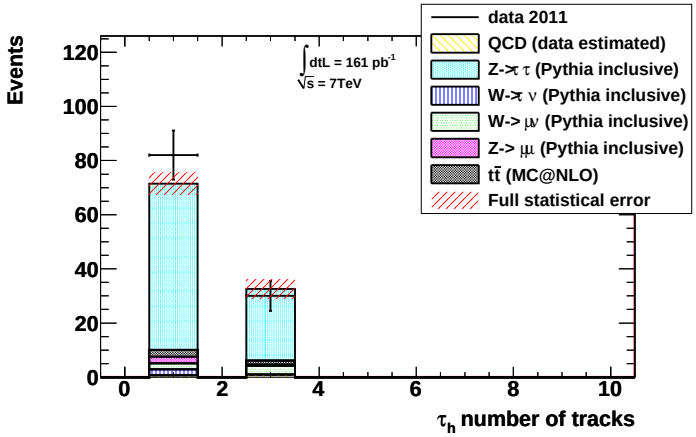

(c)

Figure 4.23: The selected tau p_{T} (a), η (b) and track multiplicity, after the full selection described in table 4.4.

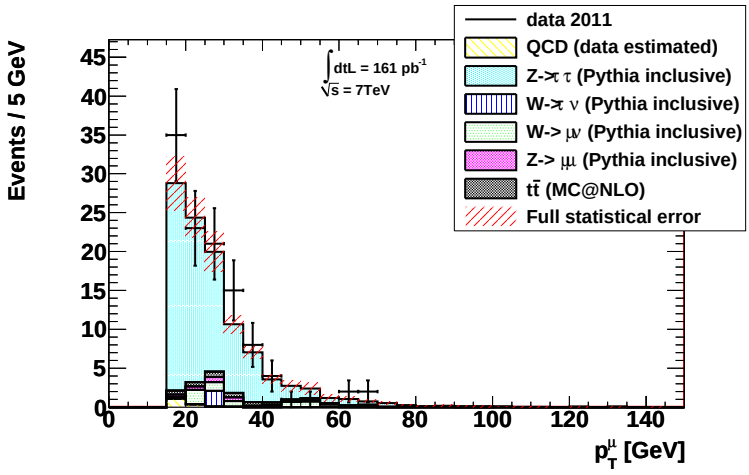

(a)

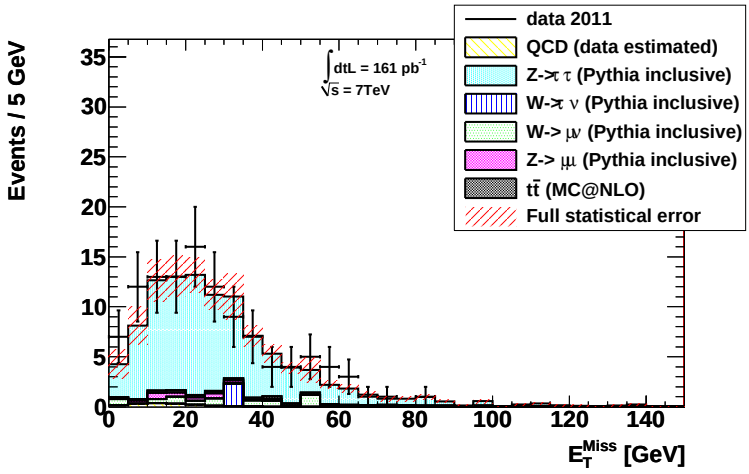

(b)

Figure 4.24: Distribution of p_{T} of the selected muon (a), and the missing transverse energy, $E_{\mathrm{T}}^{\mathrm{Miss}}$ (b), after the full selection described in table 4.4.

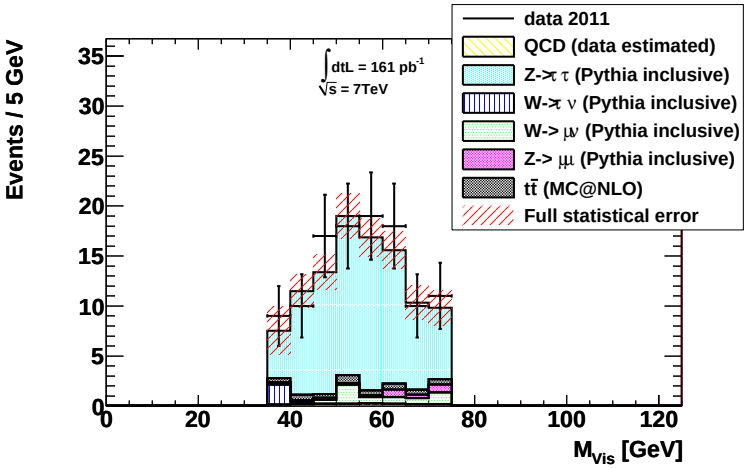

Figure 4.25: Final distribution of M_{Vis} after the full selection described in table 4.4.

that occur due to the extrapolation of the measurement to the outside of the fiducial region. σ and σ^{fid} are expressed as:

$$\sigma = \frac{N^{\mathrm{Data}} - N^{\mathrm{bckg}}}{A \cdot C \cdot \mathcal{L}_{\mathrm{int}}}, \qquad \sigma^{\mathrm{fid}} = \frac{N^{\mathrm{Data}} - N^{\mathrm{bckg}}}{C \cdot \mathcal{L}_{\mathrm{int}}}, \tag{4.10}$$

where N^{Data} and N^{bckg} are the numbers of data and estimated background events after the full selection, A is the generator acceptance, C is the reconstruction correction factor, and $\mathcal{L}_{\mathrm{int}}$ is the integrated luminosity. Both A and C are estimated using signal Monte Carlo. A is defined as:

$$A = \frac{N^{\mathrm{Fiducial}}}{N^{\mathrm{Truth}}}, \tag{4.11}$$

where N^{Truth} is the number of generated events for the full phase-space and N^{Fiducial} is the number of events that have passed the fiducial cuts at the Monte Carlo generator level. The reconstruction correction factor C is defined as:

$$C = \frac{N^{\mathrm{Selected}}}{N^{\mathrm{Fiducial}}}, \tag{4.12}$$

where N^{Selected} is the number of the selected Monte Carlo signal events. The selected signal events can be also from the outside of the acceptance region given by the fiducial cuts, and thus, C corrects also for these outlying events.

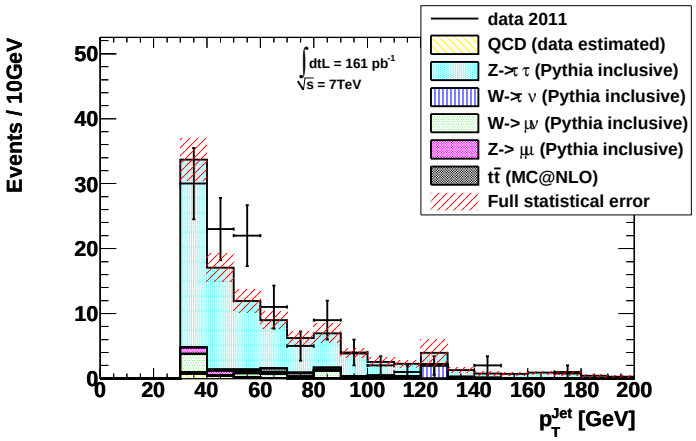

(a)

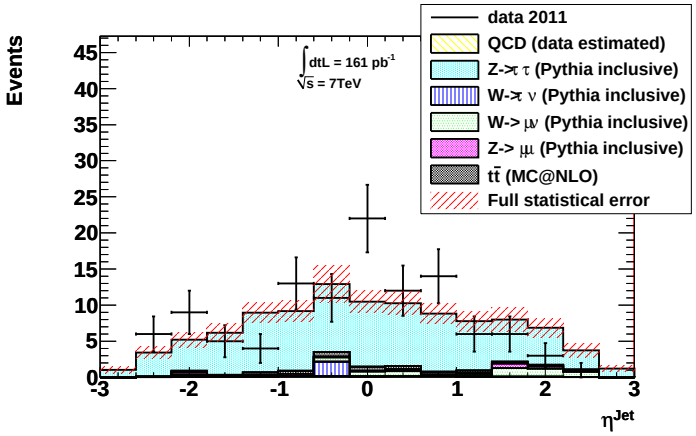

(b)

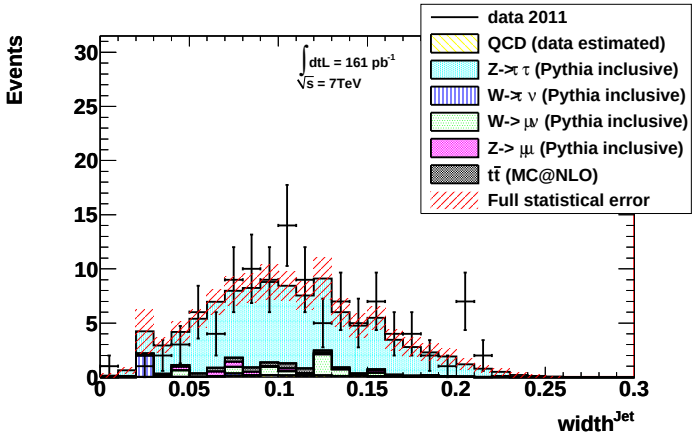

(c)

Figure 4.26: Distributions related to the leading jet in the selected $Z(\rightarrow \tau\tau)$+jet events. Leading jet p_{T} (a), η (b) and the jet width (c). The events are required to pass the full selection shown in table 4.4.

4.2 W+jet and Z+jet cross section measurements in the tau decay channel

Both, $W(\rightarrow \tau\nu)$+jet and $Z(\rightarrow \tau\tau)$+jet full cross sections and fiducial cross sections, are estimated using the expressions 4.10. The integrated luminosity of the data, $\mathcal{L}_{\mathrm{int}}$ = 161 pb^{-1}, is measured with the uncertainty of 3.4% (75), which is accounted as a contribution to the systematic uncertainty of the two measurements.

4.2.1 Signal acceptance in the W+jet analysis

The fiducial cuts in the $W(\rightarrow \tau\nu)$+jet analysis are defined with respect to the kinematics of the visible tau and the neutrinos at the Monte Carlo generator level. The visible tau is constructed from the decay products of the hadronically decaying tau, including the photons radiated by the tau and by its decay products, but excluding the tau neutrino. The fiducial cuts are defined as:

- One visible tau with p_{T} larger than 35 GeV.
- The visible tau has to have $|\eta| < 2.47$, and excluding the region $1.37 < |\eta| < 1.52$.
- The transverse projection of the momentum vector sum of neutrinos, coming from the decay of the W boson and the decay of the tau, has to be greater than 50 GeV.
- The $\Delta\phi_{\nu}^{\tau}$ angle between the direction of the visible tau and the direction of the momentum vector sum of the neutrinos has to be $0.3 < \Delta\phi_{\nu}^{\tau} < \pi - 0.3$.

Using equation 4.11 and using the Alpgen signal Monte Carlo, the acceptance in the $W(\rightarrow \tau\nu)$+jet analysis was found to be:

$$A_{\mathrm{W+jet}} = 0.0320 \pm 0.0001(\mathrm{MC\ stat.}) \pm 0.0025(\mathrm{syst.}), \tag{4.13}$$

where the first uncertainty occurs due to the limited Monte Carlo statistics, and the second is the systematic uncertainty estimated as the observed difference in the acceptances of the reference Alpgen Monte Carlo and the Pythia Monte Carlo. These Monte Carlo models differ in the used PDF set as well as in the modeling of the hadronization and the underlying events. For the given fiducial region, the estimated acceptance was

found to be higher in Pythia than in Alpgen. The difference in the estimated acceptance for Alpgen and Pythia was found to be mainly caused by the difference in η and p_{T} of the visible tau, as shown in figure 4.27. This difference was inherited from the difference in the modeling of the kinematic properties of the W boson in the two Monte Carlo models. This is shown by comparing the p_{T} distributions of the W boson, for the full phase-space, in Pythia and in Alpgen, shown in figure 4.27 (c).

To get an insight into the difference in the acceptances obtained in the two Monte Carlo models which lead to the 7.8% systematic uncertainty, a dedicated study was carried out. This study aimed to investigate to what extend this difference was connected to the different PDF sets used in the two generators (MRST LO* in Pythia and CTEQ6ll in Alpgen). By use of the LHAPDF tool (58), the Alpgen Monte Carlo event samples were reweighted in order to correspond to the Pythia PDF choice. The event weights that corrected for the difference in the used PDF sets that were provided by the LHAPDF tool were based on the information of the Bjorken variable x for each of the two interacting partons, the parton flavours, and the energy scale Q.

After reweighting of the Alpgen Monte Carlo so that its PDF set was consistent with MRST LO*, a much better agreement between Alpgen and Pythia was observed. The comparison of Pythia and Alpgen for the visible tau η, p_{T} and the W boson p_{T} distributions for the full phase space is shown in figure 4.28. The events in this figure were not pile-up reweighted due to the adverse effect of the pile-up reweighting on the statistics of the Monte Carlo, this however had only a negligible effect on the estimated acceptance.

As seen by comparing the figures 4.27 and 4.28, a much better agreement of the Pythia and Alpgen distributions is observed after the PDF reweighting is applied, and both Monte Carlo generators use the same PDF set. The difference between Pythia and Alpgen in the estimated acceptance after applying the PDF reweight on the Alpgen sample dropped from the initial 7.8% to 2.1%. This supports the conclusion that the most significant factor in the large systematic uncertainty in equation 4.13 lies in the difference of the PDF sets used in the Pythia and Alpgen samples. Since a judgement on which of the PDF sets better corresponds to the real observations fails out of the scope of this work, for all further results the Alpgen sample with the initial CTEQ6ll PDF set was used.

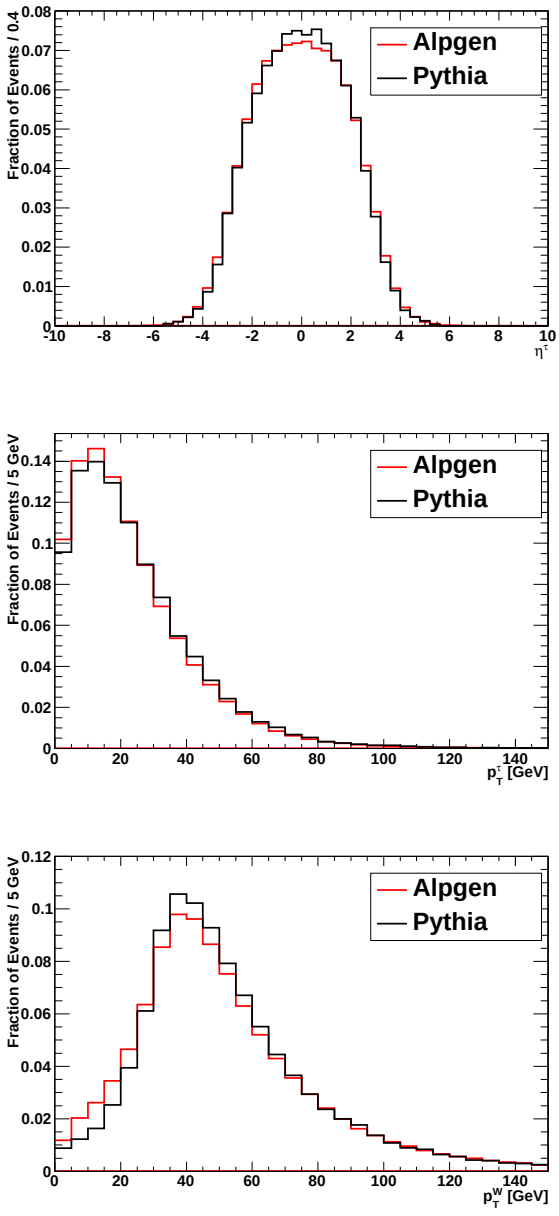

Figure 4.27: Distributions of the visible tau η (a), p_{T} (b), and the W boson p_{T} (c) at the Monte Carlo generator level, for the full phase-space of the $W(\rightarrow \tau\nu)$+jet cross section measurement, for Pythia and Alpgen.

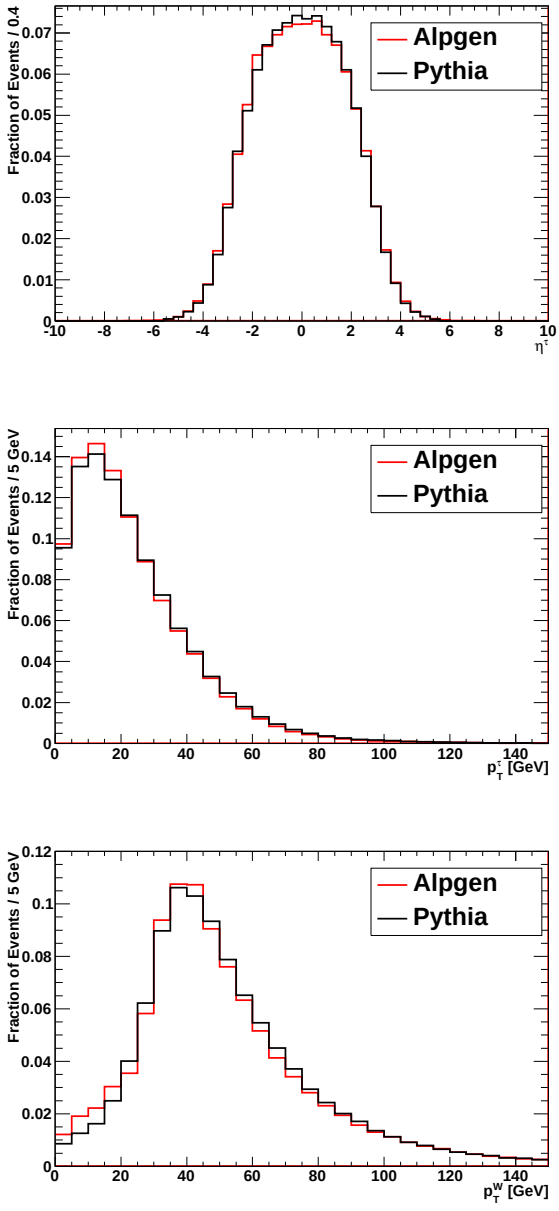

Figure 4.28: The reweighted Alpgen and Pythia distributions of the visible tau η (a), p_{T} (b), and the W boson p_{T} (c), at the Monte Carlo generator level, for the full phase-space of the $W(\rightarrow \tau\nu)$+jet analysis.

4.2.2 Reconstruction correction factor in the W+jet analysis

Using the equation 4.12, the reconstruction correction factor in the $W(\rightarrow \tau\nu)$+jet analysis was estimated as:

$$C_{\mathrm{W+jet}} = 0.086 \pm 0.001(\mathrm{MC\ stat.}), \tag{4.14}$$

where the uncertainty arises from the limited statistics of the Monte Carlo. The systematic uncertainty on the reconstruction correction factor will take into account the difference between data and Monte Carlo in the modeling of the trigger efficiency, tau identification and tau energy scale and jet energy scale.

4.2.2.1 Trigger efficiency in the W+jet analysis

The effect of the EF_TAU29_MEDIUM_XE35_NOMU trigger on the selected signal has been studied using Monte Carlo. Figure 4.29 (a) and (c) shows the significant effect of the trigger cuts on the offline tau p_{T} and offline $E_{\mathrm{T}}^{\mathrm{Miss}}$ distributions. The corresponding trigger efficiency curves are shown in figure 4.29. The Monte Carlo estimate of the EF_TAU29_MEDIUM_XE35_NOMU trigger efficiency, w.r.t the full offline selection, was found to be $\epsilon = 46.3\% \pm 0.2\%(\mathrm{MC\ stat.})$.

The main bias of the trigger on the analysis comes from the EF_XE35_NOMU part of the combined trigger. To reach the plateau of the EF_XE35_NOMU trigger, a cut of $E_{\mathrm{T}}^{\mathrm{Miss}} >$ 80-90 GeV would have to be applied, as seen in figure 4.29 (d). Such cut however is not applicable due to a strong rejective effect on the signal. Since the trigger is a very important part of the event selection, the analysis therefore relies on a good simulation of the EF_XE35_NOMU turn-on in Monte Carlo.

The systematic uncertainty on the efficiency of the EF_TAU29_MEDIUM_XE35_NOMU trigger is calculated from the systematic uncertainties of the partial EF_TAU29_MEDIUM and EF_XE35_NOMU triggers. Both triggers are assumed to be uncorrelated, and so, the uncertainties on the efficiencies of both triggers are added in quadrature when estimating the uncertainty of the combined trigger.

For the tau part of the trigger, the uncertainty is estimated by using the tag-and-probe method with $Z \rightarrow \tau\tau \rightarrow \mu\tau_{\mathrm{had}}$ events. The $Z \rightarrow \tau\tau \rightarrow \mu\tau_{\mathrm{had}}$ events in data are selected ("tagged"), using single muon trigger, and an offline selection, which follows

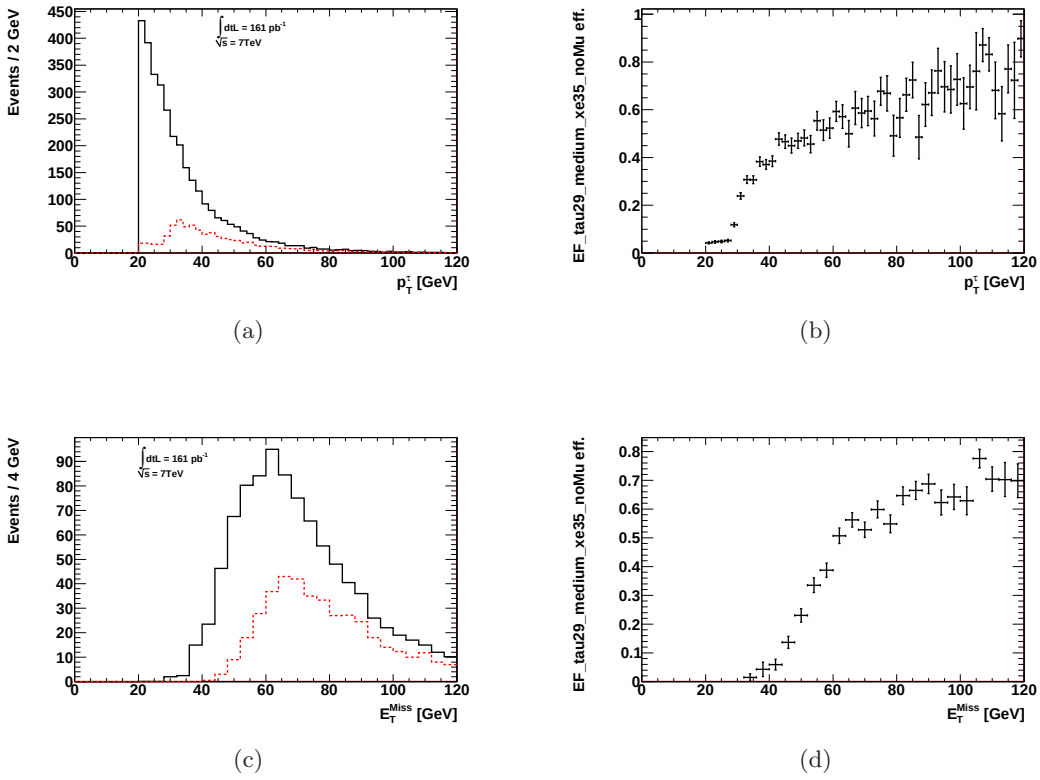

Figure 4.29: To the left are the kinematic variables of tau p_{T} and $E_{\mathrm{T}}^{\mathrm{Miss}}$ for selected Monte Carlo signal events before (full black line) and after (dashed red line) applying the EF_TAU29_MEDIUM_XE35_NOMU trigger. To the right are the corresponding turn-on curves showing the efficiency of the trigger (number of events after the trigger requirement over the number of events before the trigger) calculated by dividing the curves in the left plots. In both plots (a) and (c) the event selection summarized in table 4.2 is required, however, for the distributions in (a) the cut on the tau $p_{\mathrm{T}} > 35$ GeV is not required.

closely the offline selection in the study (65). The tau trigger efficiency is then estimated by using the τ_{had}, which is unbiased by the trigger.

The trigger efficiency of EF_TAU29_MEDIUM1 in data and in Monte Carlo is shown in figure 4.30 (45). A good agreement between the data and the Monte Carlo trigger efficiencies is observed. The 'medium1' requirement is the same as the 'medium' requirement, except a slightly tighter cut on the track multiplicity[1] of the trigger tau, which has no effect on this analysis.

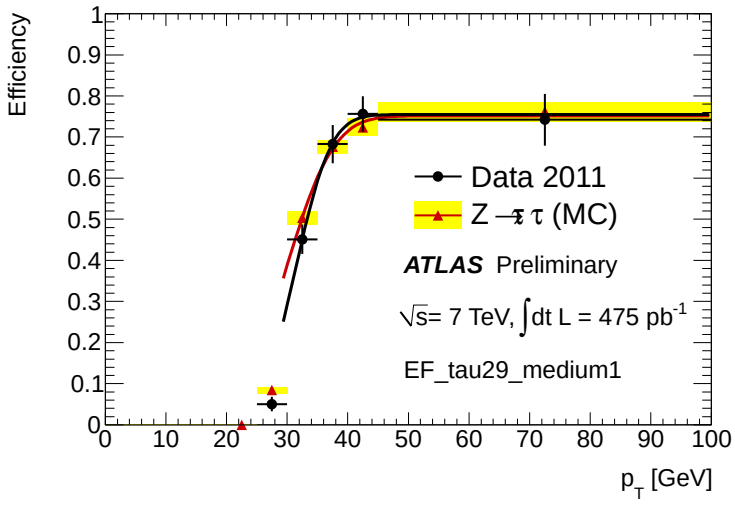

Figure 4.30: The EF_TAU29_MEDIUM1 trigger efficiency as a function of the offline tau p_{T}, for data and Monte Carlo (45).

The uncertainty is estimated from the quadratic sum of the observed difference of data and Monte Carlo trigger efficiencies, and the statistical uncertainties of data and Monte Carlo curves in every bin of the distribution 4.30. The uncertainties which are relevant for this analysis are shown for three different p_{T} bins in table 4.6. The uncertainties for the three bins are treated as uncorrelated.

p_{T} bin	35-40 GeV	40-45 GeV	>45 GeV
$\Delta\epsilon/\epsilon$	7.3 %	7 %	8.4 %

Table 4.6: Systematic uncertainty of the EF_TAU29_MEDIUM1 trigger for three different bins of the tau p_{T}.

[1] The track multiplicity of the trigger tau is smaller than six for the 'medium1' requirement.

The uncertainty on the EF_xe35_noMu trigger efficiency has been estimated by comparing the trigger efficiency in the selected $W \to e\nu$ events in data and in Monte Carlo. The $W \to e\nu$ events were used for this study since they provide one of the few possibilities to obtain an event kinematics which is similar to the signal in the main analysis. The following selection in data and Monte Carlo has been applied:

- **Trigger** - As a trigger, EF_tau16_loose_e15_medium was used. This trigger requires, besides of the electron (e15), an additional activity in the event that will cause firing of the tau16_loose trigger. This additional activity can come from an accompanying jet, yet, no explicit further requirements on the presence of a jet in the event are applied for this particular analysis. The usage of this trigger was partially also motivated by an easy access (within the analysis framework used for this study) to the real data selected by this trigger.

- **Electron Selection** - Exactly one reconstructed medium electron with $p_{\mathrm{T}} > 15$ GeV is required.

- **Electron Isolation** - The electron has to be isolated. The isolation is done by cutting on $E_{\mathrm{T}}^{\mathrm{Cone40}}/p_{\mathrm{T}}^{\mathrm{el}} < 0.1$ and $p_{\mathrm{T}}^{\mathrm{Cone40}}/p_{\mathrm{T}}^{\mathrm{el}} < 0.05$, where the $p_{\mathrm{T}}^{\mathrm{el}}$ is the transverse momentum of the electron, $E_{\mathrm{T}}^{\mathrm{Cone40}}$ is the energy in the electromagnetic calorimeter in the isolation cone $0.05 < \Delta R < 0.4$, centered around the direction of the electron, and $p_{\mathrm{T}}^{\mathrm{Cone40}}$ is the sum of the transverse momenta of all charged particles in the isolation cone $0.05 < \Delta R < 0.4$, around the electron direction.

- **Angular separation** - The ϕ angle between the missing transverse energy and the selected electron has to be $0.3 < \left|\Delta\phi^{\mathrm{el}}_{E_{\mathrm{T}}^{\mathrm{Miss}}}\right| < \pi - 0.4$.

- **Missing Transverse Energy Significance** - $S_{E_{\mathrm{T}}^{\mathrm{Miss}}} > 6$ is required.

The turn-on curves of the EF_xe35_noMu trigger, in data and in Monte Carlo, are shown in figure 4.31. The composition of the selected events has been estimated using Monte Carlo. The events that have passed the offline selection consisted of $W \to e\nu$ events (89.7%), $t\bar{t}$ (4.9%), $W \to \tau\nu$ (3.9%), $Z \to \tau\tau$ (1%) and $Z \to ee$ (0.2%). The events that have passed, in addition to the offline selection, also the EF_xe35_noMu trigger, accounted for $W \to e\nu$ (89.5 %), $t\bar{t}$ (6.6 %), $W \to \tau\nu$ (3.1 %), $Z \to \tau\tau$ (0.7 %)

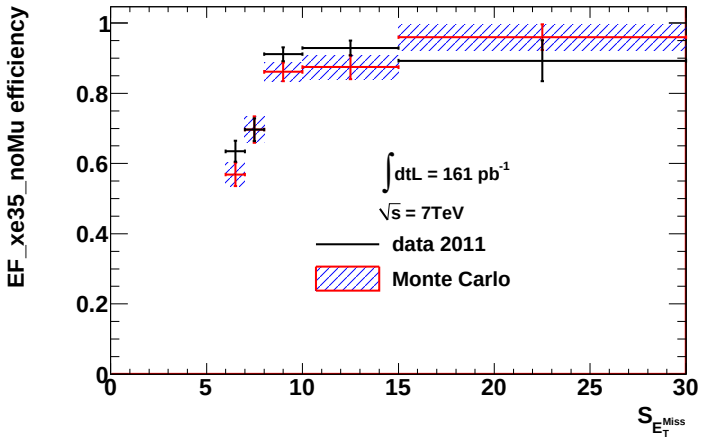

Figure 4.31: The EF_xe35_noMu trigger efficiency as a function of $S_{E_{\mathrm{T}}^{\mathrm{Miss}}}$, for data and Monte Carlo.

and $Z \rightarrow ee$ (0.01 %) events. In data, there was 833 events passing the offline selection, and 646 events that have passed the EF_xe35_noMu trigger.

A fairly good agreement in the turn-on curves of the EF_xe35_noMu trigger, in Monte Carlo and in data, is observed. Similarly as for the tau trigger, the systematic uncertainty of the EF_xe35_noMu trigger is estimated from the quadratic sum of the observed difference of data and Monte Carlo, and the statistical uncertainties of data and Monte Carlo curves, for the five $S_{E_{\mathrm{T}}^{\mathrm{Miss}}}$ bins in figure 4.31. The uncertainties for the five bins are treated as uncorrelated and are summarized in table 4.7.

$S_{E_{\mathrm{T}}^{\mathrm{Miss}}}$ value	6-7	7-8	8-10	10-15	> 15
$\Delta\epsilon/\epsilon$	13.8 %	7 %	7 %	7.6 %	10.1 %

Table 4.7: The systematic uncertainty of the EF_xe35_noMu trigger, binned in five different $S_{E_{\mathrm{T}}^{\mathrm{Miss}}}$ bins.

4.2.2.2 Tau identification and the tau energy scale uncertainty

The systematic uncertainty on the BDT medium tau ID efficiency was estimated (57) by comparing data and Monte Carlo, using $Z \rightarrow \tau\tau \rightarrow \tau_{\mathrm{had}}\mu$ events. The tau identification efficiency estimated from data was consistent with the Monte Carlo predictions. For

taus with $p_{\mathrm{T}} > 30$ GeV, the relative systematic uncertainty on the tau ID for the medium BDT ID was found to be 8.5%. This uncertainty directly propagates into the uncertainty on the reconstruction correction factor. Since the tau identification in offline and at the trigger level use different identification approaches, and are based on different variables, in this work, the uncertainty on the tau trigger and the uncertainty on the tau identification are assumed to be uncorrelated.

The uncertainty on the tau energy scale has been estimated (54) using Monte Carlo. The quantity $f_S = (p_{\mathrm{T}}^{\mathrm{Rec}} - p_{\mathrm{T}}^{\mathrm{True}})/p_{\mathrm{T}}^{\mathrm{True}}$, where the $p_{\mathrm{T}}^{\mathrm{Rec}}$ is the transverse momentum of the reconstructed tau, and $p_{\mathrm{T}}^{\mathrm{True}}$ is the transverse momentum of the true visible tau, has been defined. The systematic uncertainty was evaluated from the difference in the value of f_{S} for the nominal Monte Carlo configuration and the f_{S} values for the alternative Monte Carlo configurations, which accounted for the following seven distinct sources: Monte Carlo event generator and underlying event model, hadronic shower model, amount of detector material, electromagnetic energy scale, topological clustering noise thresholds, pile-up, and non-closure. The uncertainty was split in η and p_{T} bins of the true visible tau, estimated for one-prong and three-prong taus separately, and is summarized in table 4.8.

1-prong tau p_{T}	$\lvert\eta\rvert < 1.3$	$1.3 < \lvert\eta\rvert < 1.6$	$\lvert\eta\rvert > 1.6$
20-30 GeV	4.5 %	5 %	4.5 %
>30 GeV	3.5 %	5 %	4.5 %
3-prong tau p_{T}	$\lvert\eta\rvert < 1.3$	$1.3 < \lvert\eta\rvert < 1.6$	$\lvert\eta\rvert > 1.6$
20-30 GeV	6.5 %	5.5 %	5.5 %
30-40 GeV	5.5 %	5.5 %	5.5 %
> 40 GeV	4.5 %	5 %	5 %

Table 4.8: Tau energy scale uncertainty as a function of η and p_{T} of the true visible one-prong and three-prong taus.

In order to estimate the effect of the tau energy scale uncertainty on $C_{\mathrm{W+jet}}$, the selected tau has been first matched to the simulated true visible tau (within a cone of $\Delta R < 0.4$) and the corresponding uncertainty, according to the η and p_{T} of the true visible tau, has been obtained. Then, the p_{T} of the selected tau was recalculated, first varied by the upper value, and then by the lower value of the p_{T}, within the obtained uncertainty (in each case the $E_{\mathrm{T}}^{\mathrm{Miss}}$ was recalculated accordingly), and two $C_{\mathrm{W+jet}}^{\mathrm{up}}$ and

$C^{\mathrm{down}}_{\mathrm{W+jet}}$ were estimated. The difference of these two and the nominal $C_{\mathrm{W+jet}}$ has been calculated, and the larger has been taken as systematic uncertainty.

4.2.2.3 Jet energy scale and missing transverse energy scale

A software package, `JetUncertainties-00-03-03`, provided by the ATLAS Jet working group has been used to estimate the jet energy scale uncertainties for a given p_{T} and η bins of the anti$-k_{\mathrm{t}}04$ jets. The jet energy scale uncertainty was based on the results from the study (53), carried out by studying the jet response of the QCD jets in Monte Carlo. The difference in the nominal jet response and the alternative jet responses, which were estimated for five different categories of systematics contributions, was taken as systematic uncertainty. The typical relative jet energy scale uncertainties were between 2-4% for jets with $p_{\mathrm{T}} < 60$ GeV, and between 2-2.5% for jets with 60 GeV $< p_{\mathrm{T}} <$ 800 GeV in the central region of the detector, and 7% and 3%, respectively, for jets with $p_{\mathrm{T}} < 60$ GeV and $p_{\mathrm{T}} > 60$ GeV in the endcap region.

The effect of the jet energy scale uncertainty on $C_{\mathrm{W+jet}}$ has been estimated in a similar way as it was for the tau energy scale. The jet p_{T} has been varied by the upper and the lower value, within the uncertainty, and the larger of the differences in the number of the passed signal and background events from the nominal estimates described in the section 4.1.3.1 was taken as systematic uncertainty.

In the investigation of the effect of the small observed difference between data and Monte Carlo seen in both $E_{\mathrm{T}}^{\mathrm{Miss}}$ and $\sum E_{\mathrm{T}}$ distributions shown in figure 4.12, it is important to note that these variables are not directly used in the event selection. They are however used to define $S_{E_{\mathrm{T}}^{\mathrm{Miss}}}$, and thus the difference in data and Monte Carlo in these two variables could potentially cause a difference between data and Monte Carlo in the efficiency of the $S_{E_{\mathrm{T}}^{\mathrm{Miss}}} > 6$ cut. Even though there was no disagreement between data and Monte Carlo observed for $S_{E_{\mathrm{T}}^{\mathrm{Miss}}} > 6$, to understand whether there are any systematic effects it is important to compare data and Monte Carlo also for $S_{E_{\mathrm{T}}^{\mathrm{Miss}}} < 6$.

To compare data and Monte Carlo for the part of the spectrum where $S_{E_{\mathrm{T}}^{\mathrm{Miss}}} < 6$, the QCD background for such a comparison needs to be estimated. The number of QCD background events can be obtained by using the estimates from table 4.3 in section 4.1.3.1 for regions A and C which cover almost the full $S_{E_{\mathrm{T}}^{\mathrm{Miss}}}$ spectrum, except the gap region, $4.5 < S_{E_{\mathrm{T}}^{\mathrm{Miss}}} < 6$, and the region $S_{E_{\mathrm{T}}^{\mathrm{Miss}}} < 2$. The region $S_{E_{\mathrm{T}}^{\mathrm{Miss}}} < 2$ is

completely dominated by the QCD background and is therefore not interesting in this study.

To estimate the QCD background in the gap region it has been assumed that the tail of the $S_{E_{\mathrm{T}}^{\mathrm{Miss}}}$ distribution in the QCD background events is a continuously falling distribution, without any local minima or maxima. Therefore, using a fit of the existing space points in the QCD background $S_{E_{\mathrm{T}}^{\mathrm{Miss}}}$ distribution can provide a rough estimate of the missing space points in the gap region. The parts of the QCD background $S_{E_{\mathrm{T}}^{\mathrm{Miss}}}$ distribution estimated from data are shown, together with the fit of the tail of the distribution, in figure 4.32. The shape of the QCD background distribution for $2 < S_{E_{\mathrm{T}}^{\mathrm{Miss}}} < 4.5$ is taken from region D. The tail of the distribution was fitted by a Gaussian function with the parameters $C_1 = 1062.1 \pm 54.7$, $\sigma = 2.3 \pm 0.1$ and $\mu = 1.51 \pm 0.06$, where C_1 is a normalizing constant, σ is the standard deviation and μ is the mean.

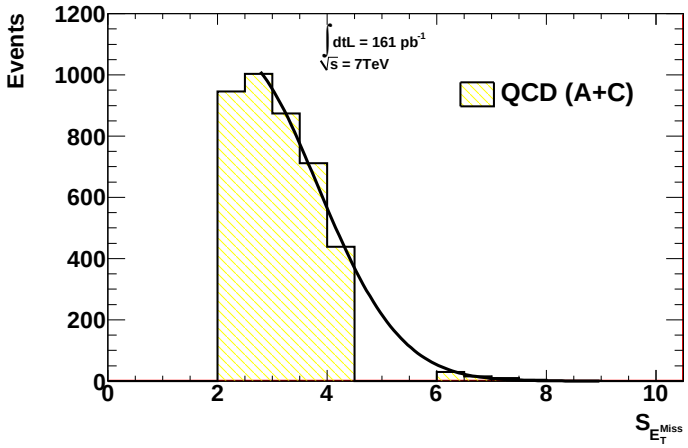

Figure 4.32: $S_{E_{\mathrm{T}}^{\mathrm{Miss}}}$ distribution in the QCD background events, normalized to the numbers corresponding to regions A and C in table 4.3. The shape of the distribution for $2 < S_{E_{\mathrm{T}}^{\mathrm{Miss}}} < 4.5$ is taken from region D.

The number of QCD background events in the region $4.5 < S_{E_{\mathrm{T}}^{\mathrm{Miss}}} < 6$ was estimated from the fit as $N_{\mathrm{QCD}}^{4.5<S_{E_{\mathrm{T}}^{\mathrm{Miss}}}<6} = 524.3 \pm 134.5$ events, where the uncertainty comes from the uncertainties on the parameters of the fit.

Using this estimate and using signal and EW background Monte Carlo estimations, the comparison to data for $S_{E_{\mathrm{T}}^{\mathrm{Miss}}}(>2)$ is shown in figure 4.33. A convincing agreement of data and Monte Carlo (with the estimated QCD background) is observed in the

$S_{E_{\mathrm{T}}^{\mathrm{Miss}}}$ spectrum. From this it is concluded that there is no reason to assume a different efficiency of the $S_{E_{\mathrm{T}}^{\mathrm{Miss}}} > 6$ cut in data and in Monte Carlo caused by the small shifts in the $E_{\mathrm{T}}^{\mathrm{Miss}}$ and $\sum E_{\mathrm{T}}$ distributions, and thus no systematic uncertainty from this source is included.

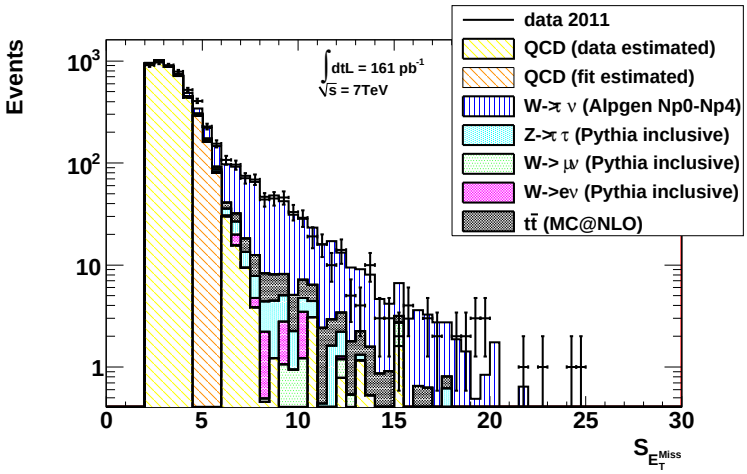

Figure 4.33: $S_{E_{\mathrm{T}}^{\mathrm{Miss}}}$ distribution for data and Monte Carlo (with the estimated QCD background) for $S_{E_{\mathrm{T}}^{\mathrm{Miss}}} > 2$.

4.2.2.4 Reconstruction correction factor uncertainty in the W+jet analysis

Besides the sources of systematic uncertainty mentioned in the previous sections, the systematic uncertainty on $C_{\mathrm{W+jet}}$ accounts also for the statistical uncertainty of the signal Monte Carlo. The single contributions to the systematic uncertainty, along with the total systematic uncertainty on $C_{\mathrm{W+jet}}$, are summarized in table 4.9.

4.2.3 Background estimation uncertainty in the W+jet analysis

The systematic uncertainty on $N_{\mathrm{W+jet}}^{\mathrm{bckg}}$ accounts, besides of the sources mentioned in the sections 4.2.2.1, 4.2.2.2, 4.2.2.3 and the statistical uncertainty of the Monte Carlo samples, also for:

Data Luminosity: The systematic uncertainty on the integrated luminosity also indirectly affects the number of background events, since the background, estimated using the Monte Carlo, is weighted accordingly to the luminosity of real data. The

Uncertainty	$\frac{\delta(C_{\mathrm{W+jet}})}{C_{\mathrm{W+jet}}}$
Trigger	12.0 %
Tau ID	8.5 %
Tau Energy Scale	7.8 %
Jet Energy Scale	0.7 %
MC stat.	1.1 %
Total	16.7 %

Table 4.9: The sources of systematic uncertainties on $C_{\mathrm{W+jet}}$ and the total systematic uncertainty.

weights of the Monte Carlo backgrounds are therefore recalculated with the upper value of the luminosity, within its uncertainty, and the difference of the new result of $N^{\mathrm{bckg}}_{\mathrm{W+jet}}$ and the nominal number of background events is taken as a systematic uncertainty.

Monte Carlo cross sections uncertainty: The uncertainty on the cross sections shown in table 4.1 is taken into account. The uncertainties on $W \to l\nu$ $(l = e, \mu, \tau)$, $Z \to ll$ $(l = e, \mu, \tau)$, and $t\bar{t}$, are assumed to be uncorrelated, and provide three independent contributions into the systematic uncertainty of the measurement[1]. The weights of the background Monte Carlo samples were recalculated by using the upper and the lower predictions of the cross sections, and the larger of the difference in N^{bckg} to the reference background estimation was taken as a systematic uncertainty.

The single contributions, and the total systematic uncertainty on the background estimation in the $W(\to \tau\nu)$+jet analysis, are summarized in table 4.10. The trigger uncertainty contribution is applied upon the Monte Carlo estimated background in the same way as it was for the signal in the $C_{\mathrm{W+jet}}$ uncertainty estimation. The tau ID and the tau energy scale contributions were applied only upon the Monte Carlo backgrounds which have true taus, i.e. $Z \to \tau\tau$ and $t\bar{t}$ backgrounds. The uncertainty on the jet energy scale was estimated as negligible and not accounted.

[1] The cross section uncertainty of the individual leptonic decays of the W (and Z) boson is due to the lepton universality assumed as fully correlated with the cross section uncertainty of the other leptonic decays.

Uncertainty	$\frac{\delta(N^{\mathrm{bckg}})}{N^{\mathrm{bckg}}}$
Luminosity	1.0 %
Cross sections	1.9 %
Trigger	7.3 %
Tau ID	2.4 %
Tau Energy Scale	2.6 %
MC stat.	1.7 %
Total	8.5 %

Table 4.10: Sources of systematic uncertainties on the total background in the $W(\rightarrow \tau\nu)$+jet analysis.

4.2.4 $W(\rightarrow \tau\nu)$+jet cross section

Using the equation 4.10, the $W(\rightarrow \tau\nu)$+jet fiducial cross section, for the fiducial region defined in the section 4.1.5 was found to be:

$$\sigma^{\mathrm{fid}}_{\mathrm{W+jet}} = 34.5 \pm 1.9(\mathrm{stat.}) \pm 6.0(\mathrm{syst.}) \pm 1.1(\mathrm{lumi.})\ \mathrm{pb} \tag{4.15}$$

The statistical uncertainty on $\sigma^{\mathrm{fid}}_{\mathrm{W+jet}}$ takes into account the statistics of real data and the statistical uncertainty on the QCD background estimation. The contributions to the systematic uncertainty are summarized in the tables 4.9 and 4.10.

Extrapolating the result 4.15 into to the full phase-space by using the estimated acceptance, the full $W(\rightarrow \tau\nu)$+jet cross section has been found to be:

$$\sigma_{\mathrm{W+jet}} = 1.08 \pm 0.06(\mathrm{stat.}) \pm 0.21(\mathrm{syst.}) \pm 0.03(\mathrm{lumi.})\ \mathrm{nb}. \tag{4.16}$$

The estimated full cross section 4.16 agrees within the uncertainty with the theoretical prediction from the equation 4.8.

4.2.5 Signal acceptance in the Z+jet analysis

The fiducial region in the $Z(\rightarrow \tau\tau)$+jet analysis is defined based on the following cuts applied upon the objects at the Monte Carlo generator level:

- One visible tau with $p_{\mathrm{T}} > 20$ GeV.
- Visible tau $|\eta| < 2.47$, excluding the region $1.37 < |\eta| < 1.52$.

- One true muon coming from a tau decay, with $p_{\mathrm{T}}^{\mu} > 15$ GeV and $|\eta| < 2.4$. The p_{T}^{μ} of the muon also takes into account radiated photons in the cone of $\Delta R < 0.1$ around the true muon.
- $\cos(\Delta\phi^{\mathrm{vis.}\,\tau}_{\sum\nu}) + \cos(\Delta\phi^{\mu}_{\sum\nu}) >$ -0.4, where $\sum\nu$ is the vector sum of the neutrino 4-vectors coming from both tau decays, and $\Delta\phi^{\mathrm{vis.}\,\tau}_{\sum\nu}$ and $\Delta\phi^{\mu}_{\sum\nu}$ is the $\Delta\phi$ angle between the neutrino sum and the visible tau, or the muon respectively.
- $M_{\mathrm{T}} = \sqrt{2 \cdot E_{\mathrm{T}}^{\sum\nu} \cdot p_{\mathrm{T}}^{\mu} \cos(1 - \cos(\Delta\phi^{\mu}_{\sum\nu}))} < 50$ GeV.
- The invariant mass of the visible tau and the muon coming from the tau decay is greater than 35 GeV and smaller than 75 GeV.

The Z+jet signal acceptance within this fiducial region has been estimated using signal Monte Carlo, and was found to be:

$$A = 0.0149 \pm 0.0001(\mathrm{MC\ stat.}) \pm 0.0012(\mathrm{syst.}). \tag{4.17}$$

The systematic uncertainty on the acceptance was estimated from the difference in A estimated for the Pythia and the Alpgen Monte Carlo. Similarly as in the case of the $(W \to \tau\nu)$+jet analysis, the estimated acceptance in Pythia was larger than in Alpgen. Also in this analysis the difference between Alpgen and Pythia occurs after applying the kinematic requirements on the visible tau and the muon. The comparison of Pythia and Alpgen in the distributions of the visible tau η, and p_{T}, muon η and the Z boson p_{T} at the Monte Carlo generator level are shown in figure 4.34 (a)-(d). The difference in the p_{T} distributions of the Z boson for the two Monte Carlo models shown in figure 4.34 (d) shows a similarity to the equivalent distributions for the W bosons in figure 4.27 (c). It is therefore assumed that the difference has a common origin with the similar difference observed in the W+jet analysis, and is related to the difference in the PDF sets used in Pythia and in Alpgen.

4.2.6 Reconstruction correction factor in the Z+jet analysis

Using the equation 4.12, and using the Alpgen Monte Carlo signal sample, the estimated reconstruction correction factor was found to be:

$$C_{\mathrm{Z+jet}} = 0.306 \pm 0.005(\mathrm{MC\ stat.}), \tag{4.18}$$

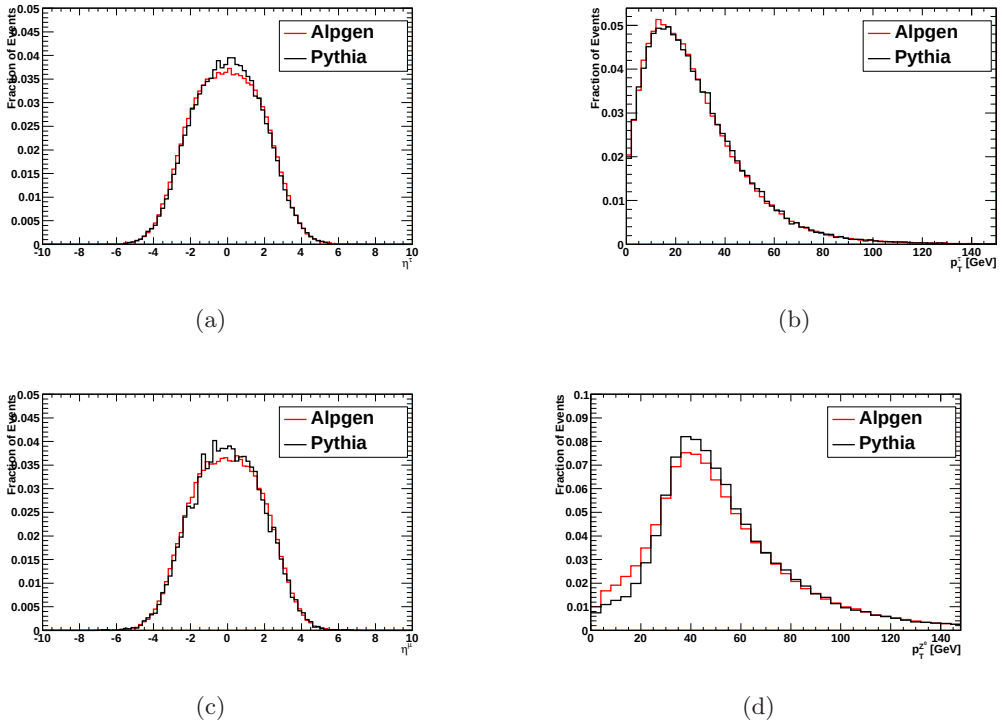

Figure 4.34: Distributions of the visible tau η (a), p_{T} (b), muon η (c), and the Z boson p_{T} (d), in the Pythia and Alpgen signal Monte Carlo, at the Monte Carlo generator level, for the full phase-space of the $Z(\rightarrow \tau\tau)$+jet cross section measurement.

where the uncertainty occurs due to the limited statistics in Monte Carlo. In addition, the following sources of systematic uncertainty on $C_{\mathrm{Z+jet}}$ were taken into account: trigger efficiency, tau ID and tau energy scale uncertainty, jet energy scale uncertainty and muon reconstruction uncertainty.

The tau energy scale uncertainty and the jet energy scale uncertainty were estimated as described in the sections 4.2.2.2 and 4.2.2.3. The tau identification uncertainty for a tau with $p_{\mathrm{T}} > 20$ GeV was estimated to be 9.9% (57).

4.2.6.1 Trigger efficiency in the Z+jet analysis

The efficiency of the EF_TAU16_LOOSE_MU15 trigger was estimated by using the signal Monte Carlo to be 57% ± 1%(MC stat.), with respect to the offline selection.

The trigger efficiency as a function of the p_{T} of the selected tau and the selected muon, as well as the p_{T} distributions of the selected tau and the muon before and after the trigger requirement, is shown in figure 4.35. As can be seen, the trigger plateau of the EF_TAU16_LOOSE_MU15 trigger is reached at tau p_{T} ∼40 GeV. This p_{T} threshold is however too high to apply due to its adverse effect on the signal. The analysis therefore relies on good modeling of the turn-on region of the trigger. The EF_TAU16_LOOSE_MU15 turn-on curve as a function of the muon p_{T} remains flat, with no significant deviations throughout the whole muon p_{T} spectrum, as shown in figure 4.35 (d).

The systematic uncertainty of the EF_TAU16_LOOSE trigger has been estimated by comparing the trigger efficiency in Monte Carlo and in data. The EF_TAU16_LOOSE efficiency in data has been estimated by using the tag-and-probe method, on a data sample with the integrated luminosity $\mathcal{L}_{\mathrm{int}} = 353$ pb^{-1}. For the method, $Z \to \tau\tau \to \tau_{\mathrm{had}}\tau_{\mu}$ events have been selected by using the single MU18 trigger. The offline selection was following most of the requirements from table 4.4, but the requirement on the additional jet was not applied, the muon isolation requirement has been tightened to $E_{\mathrm{T}}^{\mathrm{Cone40}}/p_{\mathrm{T}}^{\mu} < 0.03$ and $p_{\mathrm{T}}^{\mathrm{Cone40}}/p_{\mathrm{T}}^{\mu} < 0.03$, and to reduce the influence of the W background, the cut on the direction of $E_{\mathrm{T}}^{\mathrm{Miss}}$ has been tightened to $\cos(\phi^{\tau} - \phi^{E_{\mathrm{T}}^{\mathrm{Miss}}}) + \cos(\phi^{\mu} - \phi^{E_{\mathrm{T}}^{\mathrm{Miss}}}) > -0.1$. In data, 972 events have been selected from which 480 have passed the EF_TAU16_LOOSE trigger.

In figure 4.36 are the distributions of the selected tau p_{T} before (a) and after (b) the EF_TAU16_LOOSE trigger for data (black), and Monte Carlo (signal + EW background)

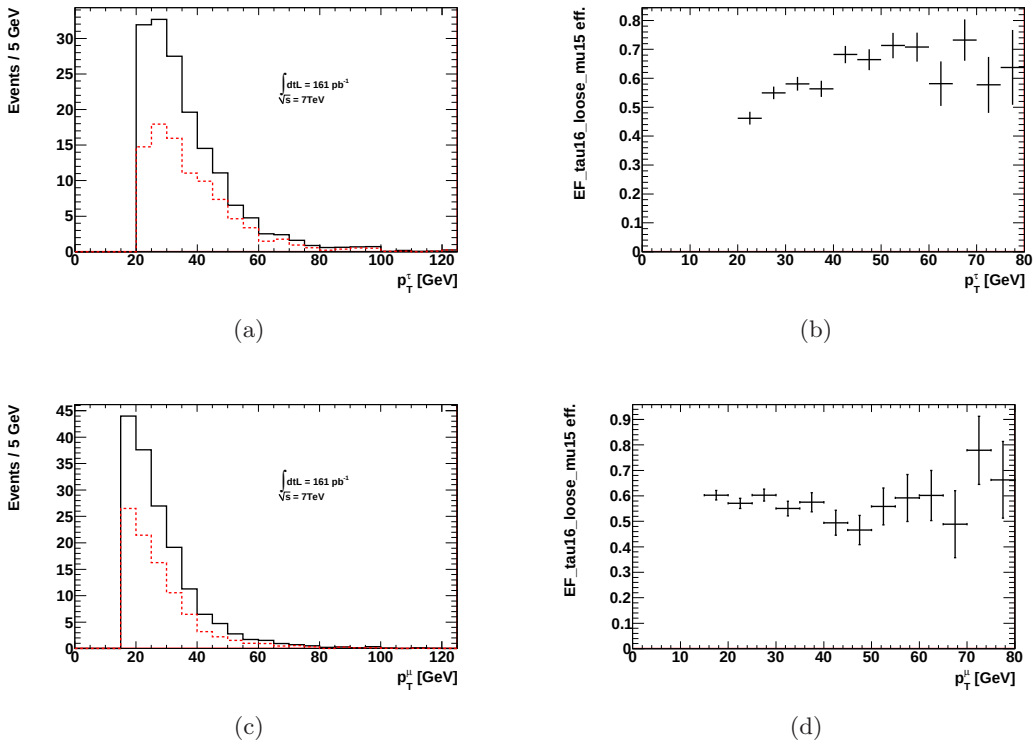

(a) (b)

(c) (d)

Figure 4.35: The plots (a) and (c) show the signal Monte Carlo distributions of the transverse momenta of the tau (a), and the muon (c), after the full offline selection, before (black curve), and after (red dashed curve) the EF_TAU16_LOOSE_MU15 requirement. The plots (b) and (d) show the efficiency of the EF_TAU16_LOOSE_MU15 trigger,as a function of the tau (b) and the muon (d) p_{T}. The offline selection is summarized in table 4.4.

with the estimated QCD background (red). For the QCD background estimation, the same method as described for the $Z(\rightarrow \tau\tau)$+jet analysis has been used. Pythia Monte Carlo has been used to simulate the signal as well as the EW background, and MC@NLO has been used to simulate $t\bar{t}$. Based on the Monte Carlo prediction, the data composition before the EF_TAU16_LOOSE requirement accounted for $Z \rightarrow \tau\tau$ (79.9%), QCD background (7%), $W \rightarrow \mu\nu$ (5.9%), $Z \rightarrow \mu\mu$ (5.3%), $W \rightarrow \tau\nu$ (1%) and $t\bar{t}$ (0.8%). The data after the EF_TAU16_LOOSE trigger requirement consisted of $Z \rightarrow \tau\tau$ (90.1%), QCD background (2.4%), $W \rightarrow \mu\nu$ (3.5%), $Z \rightarrow \mu\mu$ (3.1%) and $t\bar{t}$ (0.8%). The efficiency curves of the EF_TAU16_LOOSE trigger in Monte Carlo and in data are shown in figure 4.36 (c).

The systematic uncertainties of the EF_TAU16_LOOSE trigger are given for four different p_{T} bins of the selected tau, and are shown in table 4.11. This uncertainty will propagate directly into the uncertainty on the number of the selected signal and background events for a given p_{T} bin of the selected tau.

p_{T} bin	20-30 GeV	30-40 GeV	40-50 GeV	>50 GeV
$\Delta\epsilon/\epsilon$	13.8 %	6.9 %	14.6 %	12.7 %

Table 4.11: The systematic uncertainties of the EF_TAU16_LOOSE trigger item in different bins of the transverse momentum of the selected tau.

The uncertainty on the efficiency of the MU15 trigger has been estimated approximately, by using the results on the uncertainty of the MU18 trigger. The systematic uncertainty of the mu18 trigger was 2.8 % (76). Since the MU18 is the closest trigger to the MU15 trigger (both MU15 and MU18 start from the same L1 item, L1_MU10), the same systematic uncertainty is used also for the MU15 trigger efficiency. Since in the comparison to the tau trigger uncertainty, the uncertainty of the MU18(MU15) trigger is relatively low, the extrapolation from the MU18 results to the MU15 results should be sufficient for the purpose of having an estimate on the combined TAU16_LOOSE_MU15 combined trigger uncertainty.

4.2.6.2 Muon Reconstruction and Muon isolation

The muon reconstruction efficiency has been studied on $Z \rightarrow \mu\mu$ events in Monte Carlo and in real data (60). Tag-and-probe method has been used with real data sample

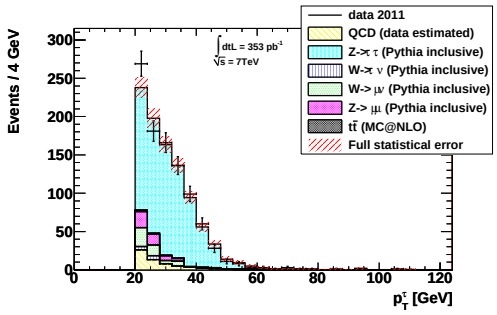

(a)

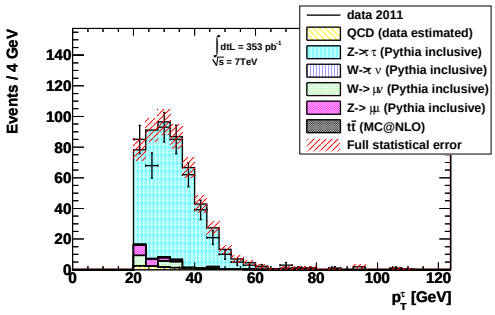

(b)

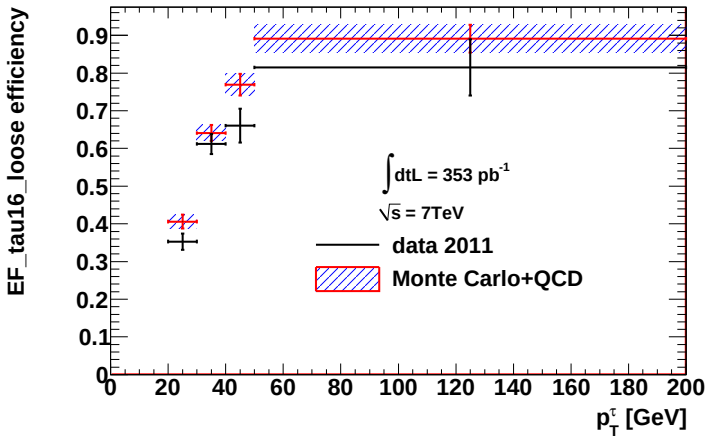

(c)

Figure 4.36: In (a) and (b) are the distributions of the selected tau p_{T} after the selection described in the text, before (a), and after (b), the EF_TAU16_LOOSE requirement in data, and Monte Carlo + QCD background. In (c) are the efficiency curves of the EF_TAU16_LOOSE trigger for Monte Carlo + QCD background, and data.

with the integrated luminosity $\mathcal{L}_{\text{int}} = 40$ pb^{-1}. The muon reconstruction efficiency of the combined muons has been estimated to be greater than 96%, and agrees with the Monte Carlo within less than 1% (60). To estimate the uncertainty on the muon reconstruction efficiency, a software package provided by the ATLAS muon working group, `MuonEfficiencyCorrections-00-02-02`, has been used. This provided the uncertainty split in η-ϕ bins of the reconstructed muons. The events passing the selection obtained an additional weight, corresponding to the upper value of the uncertainty. The difference in the final number of signal and background events, with respect to the result in the section 4.4, was taken as systematic uncertainty.

In order to study the accuracy of the modeling of the muon isolation in Monte Carlo, selected $Z \to \mu\mu$ events were used. A good agreement between data and Monte Carlo in these events was observed (60). The muon isolation variables for data and Monte Carlo are shown in figure 4.37. Although, in comparison to the $Z \to \mu\mu$ events, the $Z(\to \tau\tau \to \tau_{\text{had}}\mu)$+jet events are busier, a good understanding of the shape of the accompanying leading jet, as shown in figure 4.26 (c), allows to apply the conclusions from (60) also in this study. The systematic uncertainty due to the muon isolation is thus assumed to be negligible.

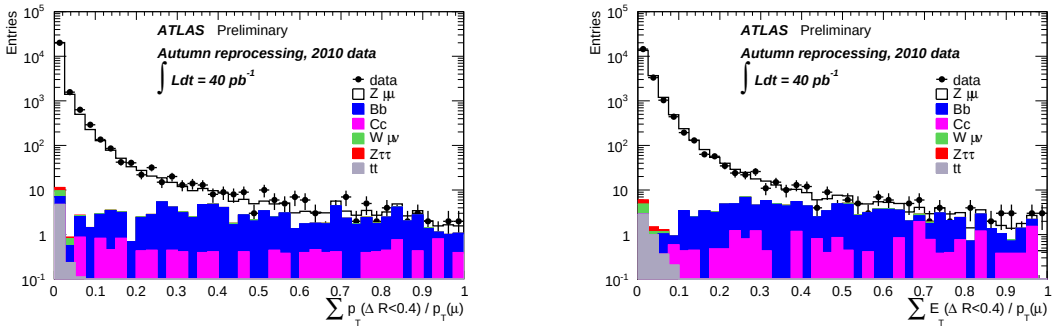

(a) (b)

Figure 4.37: The isolation variables $p_{\text{T}}^{\text{Cone40}}/p_{\text{T}}^{\mu}$ (a) and $E_{\text{T}}^{\text{Cone40}}/p_{\text{T}}^{\mu}$ (b) of the "probe" muons, selected from $Z \to \mu\mu$ events, using the tag-and-probe method. The analysis with the selection is described in the work (60). A good agreement in Monte Carlo and in data is observed.

4.2.6.3 Reconstruction correction factor uncertainty in the Z+jet analysis

The contributions to the total systematic uncertainty on the reconstruction correction factor, $C_{\mathrm{Z+jet}}$, are summarized in table 4.12.

Uncertainty	$\frac{\delta(C_{Z+jet})}{C_{Z+jet}}$
Trigger	12.1 %
Tau ID	9.9 %
Tau Energy Scale	2.0 %
Jet Energy Scale	2.6 %
Muon Reconst.	0.4 %
MC stat.	1.6 %
Total	16.0 %

Table 4.12: Sources of systematic uncertainties on the reconstruction correction factor in the $Z(\rightarrow \tau\tau)$+jet analysis.

4.2.7 Background estimation uncertainty in the Z+jet analysis

The systematic uncertainty on the background estimation takes into account the same contributions as discussed for the reconstruction correction factor uncertainty. In the same way as described in the W+jet analysis, the uncertainties on the data luminosity and on the Monte Carlo cross sections are also taken into account. Table 4.13 summarizes the contributions to the total systematic uncertainty on the background estimation in the Z+jet analysis.

In the same way as in the W+jet analysis, the uncertainties on the tau identification and the tau energy scale apply only to the backgrounds which have a true tau, such as the $t\bar{t}$ background.

4.2.8 $Z(\rightarrow \tau\tau)$+jet cross section

Combining the obtained partial results, the $Z(\rightarrow \tau\tau)$+jet fiducial cross section in the fiducial region defined in the section 4.2.6 was found to be:

$$\sigma^{\mathrm{fid}}_{\mathrm{Z+jet}} = 1.9 \pm 0.2(\mathrm{stat.}) \pm 0.3(\mathrm{syst.}) \pm 0.1(\mathrm{lumi.})\ \mathrm{pb}, \tag{4.19}$$

Uncertainty	$\frac{\delta(N^{\mathrm{bckg}})}{N^{\mathrm{bckg}}}$
Luminosity	1.0 %
Cross sections	2.6 %
Trigger	11.7 %
Tau ID	1.1 %
Tau Energy Scale	0.4 %
Jet Energy Scale	4.8 %
Muon Reconst.	0.4 %
MC stat.	11.1 %
Total	17.1 %

Table 4.13: Sources of systematic uncertainties in the $Z(\rightarrow \tau\tau)$+jet analysis.

where the statistical uncertainty combines the statistical uncertainty from data and from the estimated QCD background and the systematic uncertainty contributions are summarized in tables 4.12 and 4.13.

The fiducial cross section was extrapolated into the full phase-space using the estimated acceptance from section 4.2.5. The $Z(\rightarrow \tau\tau)$+jet cross section for the full phase-space was estimated as:

$$\sigma_{\mathrm{Z+jet}} = 0.130 \pm 0.015(\mathrm{stat.}) \pm 0.023(\mathrm{syst.}) \pm 0.004(\mathrm{lumi.})\ \mathrm{nb} \tag{4.20}$$

This result corresponds well within uncertainties with the theoretical prediction of equation 4.9.

4.3 R_{JET} measurement

The theoretical prediction for R_{JET}, obtained by combining the results from equations 4.8 and 4.9, and using the equation 4.1, was:

$$R_{\mathrm{JET}}^{\mathrm{MC}} = 9.5 \pm 0.3(\mathrm{cross\ section}), \tag{4.21}$$

where the uncertainty comes from the $W(\rightarrow \tau\nu)$+jet and $Z(\rightarrow \tau\tau)$+jet cross sections uncertainties which are assumed as uncorrelated.

For data, R_{JET} from equation 4.1 can be rewritten using equation 4.10 to:

$$R_{\mathrm{JET}} = \frac{N^{\mathrm{Data}}_{\mathrm{W+jet}} - N^{\mathrm{bckg}}_{\mathrm{W+jet}}}{N^{\mathrm{Data}}_{\mathrm{Z+jet}} - N^{\mathrm{bckg}}_{\mathrm{Z+jet}}} \cdot \frac{C_{\mathrm{Z+jet}}}{C_{\mathrm{W+jet}}} \cdot \frac{A_{\mathrm{Z+jet}}}{A_{\mathrm{W+jet}}} = \frac{\sigma^{\mathrm{fid}}_{\mathrm{W+jet}}}{\sigma^{\mathrm{fid}}_{\mathrm{Z+jet}}} \cdot \frac{A_{\mathrm{Z+jet}}}{A_{\mathrm{W+jet}}}. \tag{4.22}$$

The fiducial cross sections ratio, $R^{\mathrm{fid}}_{\mathrm{JET}} = \frac{\sigma^{\mathrm{fid}}_{\mathrm{W+jet}}}{\sigma^{\mathrm{fid}}_{\mathrm{Z+jet}}}$, was estimated by taking the results in equations 4.15 and 4.19 as:

$$R^{\mathrm{fid}}_{\mathrm{JET}} = 17.8 \pm 2.2(\mathrm{stat.}), \tag{4.23}$$

where the uncertainty arises from the statistics of the measured data. To estimate the total systematic uncertainty on $R^{\mathrm{fid}}_{\mathrm{JET}}$, the correlation of some sources of systematic uncertainty on the single results 4.15 and 4.19 needs to be taken into account. This leads into a partial cancellation of these sources in the ratio.

The contributions to the total systematic uncertainty which enter both $\sigma^{\mathrm{fid}}_{\mathrm{W+jet}}$ and $\sigma^{\mathrm{fid}}_{\mathrm{Z+jet}}$ come from:

- **Luminosity** - The luminosity uncertainty which affects the estimation of the EW background affects both W+jet and Z+jet analyses in the same way, and thus will in the ratio cancel to high degree. Yet, second order effects from the background estimation remain and cause a small systematic uncertainty on $R^{\mathrm{fid}}_{\mathrm{JET}}$ of 0.2%.

- **Cross sections** - The EW backgrounds which are common for both W+jet and Z+jet analyses are $W \to l\nu$ (where l can be e, μ and τ) and $t\bar{t}$. The uncertainties on the cross sections for these backgrounds is therefore canceled when estimating the systematic uncertainty on $R^{\mathrm{fid}}_{\mathrm{JET}}$. The systematic uncertainty on $R^{\mathrm{fid}}_{\mathrm{JET}}$ from the Monte Carlo cross section uncertainties was found to be 0.4%.

- **Tau ID** - To estimate how the tau ID uncertainty cancels in the ratio, the selected signal and background taus in the Z+jet analysis have been split according to their p_{T} as those above the threshold of 35 GeV, and those below. The effect of the tau ID uncertainty on $R^{\mathrm{fid}}_{\mathrm{JET}}$ has then been studied separately for the case when the taus in both Z+jet and W+jet analyses have the same threshold of $p_{\mathrm{T}} > 35$ GeV (i.e. only taus above this p_{T} threshold are contributing into the $\sigma_{\mathrm{Z+jet}}$ measurement) and for the case when the taus in the Z+jet analysis have 20 GeV

$< p_{\mathrm{T}} < 35$ GeV. In the first case, the tau ID uncertainty in both analyses is fully correlated, while in the second case a conservative assumption has been made that the tau ID uncertainties in both analyses are uncorrelated.

The estimated contribution to the $R_{\mathrm{JET}}^{\mathrm{fid}}$ uncertainty in the case when in both analyses the taus have $p_{\mathrm{T}} > 35$ GeV was found to be 0.5%. The reason why for this case the uncertainty was not completely cancelled was due to different compositions of backgrounds containing true taus in the two analyses. The tau ID uncertainty for taus with 20 GeV $< p_{\mathrm{T}} < 35$ GeV has been assumed to be equal to the tau ID uncertainty for taus with $p_{\mathrm{T}} > 20$ GeV, i.e. 9.9%. The contribution to the uncertainty on $R_{\mathrm{JET}}^{\mathrm{fid}}$, when in the Z+jet analysis only the taus with 20 GeV $< p_{\mathrm{T}} < 35$ GeV contribute to $\sigma_{\mathrm{Z+jet}}$, was found to be 7.4%.

- **Trigger** Although the triggers in the W+jet and Z+jet analysis are different, the tau trigger parts in both combined triggers (EF_TAU29_MEDIUM in the W+jet analysis and EF_TAU16_LOOSE in the Z+jet analysis) are assumed to be correlated to some degree. Similarly as in the discussion to the tau ID systematics cancellation, to estimate the correlation of the two triggers, the selected taus in the Z+jet analysis are split in two samples based on whether the selected taus have passed at the trigger level the EF_TAU29_MEDIUM trigger requirement (the taus are also required to pass the tau $p_{\mathrm{T}} > 35$ GeV cut), and in taus which didn't pass the EF_TAU29_MEDIUM trigger (or the tau p_{T} cut). In the first case, the tau trigger uncertainty for taus in the Z+jet analysis will be fully correlated with the tau trigger uncertainty for taus in the W+jet analysis. On the other hand the taus which didn't pass the EF_TAU29_MEDIUM trigger are assumed to have the tau trigger uncertainty, and thus the whole combined trigger uncertainty fully uncorrelated. The contribution to the $R_{\mathrm{JET}}^{\mathrm{fid}}$ uncertainty from the triggers, in case the uncertainty on the tau part of trigger was correlated in both $\sigma_{\mathrm{Z+jet}}$ and $\sigma_{\mathrm{W+jet}}$ measurements, has been estimated to be 2.4%. The contribution to the $R_{\mathrm{JET}}^{\mathrm{fid}}$ uncertainty when the triggers in both analyses were assumed to be uncorrelated was estimated to be 14.2%.

- **Tau energy scale** - The uncertainty on $R_{\mathrm{JET}}^{\mathrm{fid}}$ coming from the uncertainty on the tau energy scale has been estimated by simultaneously (in both W+jet and Z+jet analyses) recalculating the energy of the selected tau. The energy of the

selected tau has been set to the lower value, within the energy scale uncertainty given by the table 4.8. The difference from the reference value on $R^{\mathrm{fid}}_{\mathrm{JET}}$ was found to be 7.3%, and was taken as systematic uncertainty.

- **Jet energy scale** - The effect of the jet energy scale uncertainty on $R^{\mathrm{fid}}_{\mathrm{JET}}$ has been estimated in the same way as for the tau energy scale uncertainty, scaling down (within the uncertainty) simultaneously the jet energy in both W+jet and Z+jet analyses and comparing the newly obtained $R^{\mathrm{fid}}_{\mathrm{JET}}$ with the reference from 4.23. The difference was taken as systematic uncertainty. The uncertainty was estimated to be 2.6%.

The systematic uncertainties that enter only either $\sigma^{\mathrm{fid}}_{\mathrm{W+jet}}$, or $\sigma^{\mathrm{fid}}_{\mathrm{Z+jet}}$, were estimated as independent sources of systematic uncertainty, whose values were taken from the tables 4.9, 4.10, 4.12 and 4.13. The statistical uncertainty on Monte Carlo is also taken as an independent source of systematic uncertainty on $R^{\mathrm{fid}}_{\mathrm{JET}}$. All contributions to the systematic uncertainty, along with the total relative systematic uncertainty, are summarized in table 4.14.

Uncertainty	$\frac{\delta(R^{\mathrm{fid}}_{\mathrm{JET}})}{R^{\mathrm{fid}}_{\mathrm{JET}}}$
Luminosity	0.2%
Cross sections	0.4%
Tau ID	7.4%
Tau energy scale	7.3%
Jet energy scale	2.6%
Trigger	14.4 %
Muon reconst.	0.4 %
MC stat.	2.8 %
Total	18.2%

Table 4.14: Contributions to the systematic uncertainties on $R^{\mathrm{fid}}_{\mathrm{JET}}$.

The acceptance ratio:

$$\frac{A_{\mathrm{Z+jet}}}{A_{\mathrm{W+jet}}} = (465.6 \pm 3.4(\text{MC stat.}) \pm 0.9(\text{syst.})) \cdot 10^{-3}, \tag{4.24}$$

was estimated by using the results from the sections 4.2.1 and 4.2.5. The result takes into account the statistical uncertainty coming from the Monte Carlo and a systematic

uncertainty which was obtained by comparing the acceptance ratio in two different Monte Carlo models, Pythia and Alpgen. In contrast to the systematic uncertainty on the individual acceptances, $A_{\mathrm{Z+jet}}$ and $A_{\mathrm{W+jet}}$, which were at the order of ∼8-9% it is worth to mention that this systematic uncertainty, coming mainly from the PDF uncertainty, got reduced in the ratio of the acceptances to approximately 0.2%.

Using the equation 4.22, the R_{JET} ratio in the tau decay channel, calculated with ATLAS data with the integrated luminosity $\mathcal{L}_{\mathrm{int}} = 161\ \mathrm{pb}^{-1}$, was found to be:

$$R_{\mathrm{JET}} = 8.3 \pm 1.0(\mathrm{stat.}) \pm 1.5(\mathrm{syst.}) \tag{4.25}$$

This result agrees with the theoretical prediction, within the statistical and systematic uncertainty of the measurement. The largest contribution to the total systematic uncertainty of the result in equation 4.25 provide the trigger uncertainty. This contribution is large since in the W+jet and Z+jet analyses the trigger uncertainties represent the largest errors, and because only the tau part of the triggers could be partially cancelled in the ratio.

The canceling of the energy scale uncertainties (jet and tau energy scale) was not successful. The comparison of figures 4.11 (a) with 4.23 (a), and 4.14 (a) with 4.26 (a), shows a clear difference in the p_{T} spectra of the selected tau and the leading jet in the two analyses. The explanation of this lies in the fact that the event selection in the W+jet analysis has preferred, due to the high energy thresholds, boosted decay products of the W's (thus boosted W's). This caused a bias on the p_{T} of the accompanying jet towards higher values. In the Z+jet analysis, however, this was not the case and the jet p_{T} was not biased in this way. Due to the systematically different energies of the taus and jets in the two analyses, the canceling of the energy scale uncertainties in the R_{JET} ratio could not be fully carried out. This also caused that the effort to cancel the contributions from the tau ID uncertainty was only partially successful, since the tau ID uncertainty is bound to a certain energy scale which was different in the two analyses.

The systematic uncertainties on the luminosity, the cross sections, and the uncertainty on the Monte Carlo model, have had only a minor effect on the R_{JET} ratio. Their contribution to systematics of the measurement has been effectively cancelled out in the ratio.

4. W+JET CROSS SECTION, Z+JET CROSS SECTION AND THE R_{JET} MEASUREMENT IN THE TAU DECAY CHANNEL WITH 2011 ATLAS DATA

5

Summary

The studies presented in this work were the first approach to provide the observations and the cross section measurements of the $W(\rightarrow \tau\nu)$+jet and $Z(\rightarrow \tau\tau)$+jet events, and the R_{JET} measurement in the tau decay channel.

In the second and in the third chapter, the Standard Model and the the LHC accelerator with the ATLAS experiment were introduced. This was supposed to give the reader a theoretical background needed to understand the measurements done in this analysis.

The $W(\rightarrow \tau\nu)$+jet, $Z(\rightarrow \tau\tau)$+jet, and the R_{JET} measurements were presented in chapter 4. Both separate cross section measurements included the estimations of the acceptances, the reconstruction correction factors, EW and QCD backgrounds, and the estimations of the systematic uncertainties. The direct comparison of the estimated $W(\rightarrow \tau\nu)$+jet and $Z(\rightarrow \tau\tau)$+jet cross sections has shown a good agreement with the theoretical predictions. Within the uncertainties of the measurement, no large deviations of the results from the predictions, that could lead us to the signs of new physics, could be observed.

A crucial improvement of the R_{JET} measurement would be the usage of a common trigger for both W+jet and Z+jet analyses. With this improvement, the systematic uncertainty of the trigger could be reduced. Furthermore, having the same trigger in both analyses would allow to apply a more similar event selection in the W+jet and the Z+jet analyses, leading to a better canceling of the energy scale uncertainties, which was one of the practical arguments for doing the R_{JET} measurement. However, designing such a trigger for the data taking at high instantaneous luminosity, and at

the same time fulfill the constraints on the signal efficiencies and the rates of such a trigger, remains a very ambitious task. Nonetheless, if these improvements would be carried out, a more precise testing of the existence of the physics beyond the Standard Model at the TeV scale could be provided.

Bibliography

[1] Lord Kelvin, Nineteenth-Century Clouds over the Dynamical Theory of Heat and Light, *Phil. Mag.* Sixth Series, 2, 1-40 (1901) 1

[2] P. Langacker, Structure of the Standard Model, arXiv:hep-ph/0304186v1 (2003) 4, 20

[3] A. Pich, The Standard Model of Electroweak Interactions, arXiv:0705.4264v1 [hep-ph] (2007) 4

[4] K. Nakamura *et al.*, (Particle Data Group), *J. Phys. G* 37, 075021 (2010) 5, 8, 9, 10, 12, 20, 21, 23

[5] UA1 Collaboration, Experimental observation of isolated large transverse energy electrons with associated missing energy at $\sqrt{s}$ = 540 GeV, *Phys. Lett.* B **122**, 103-116 (1983) 7

[6] UA2 Collaboration, Evidence for Z0 → e+e- at the CERN $\overline{p}p$ collider, *Phys. Lett.* B**129**, 130-140 (1983) 7

[7] MuLan Collaboration, Improved Measurement of the Positive Muon Lifetime and Determination of the Fermi Constant, *Phys. Rev. Lett.* **99**, 032001 (2007), arXiv:0704.1981v2 [hep-ex] 7

[8] G. Gabrielse, D. Hanneke, T. Kinoshita, M. Nio, B. Odom, New Determination of the Fine Structure Constant from the Electron g Value and QED, *Phys. Rev. Lett.* **97**, 030802 (2006) 7

[9] G. P. Zeller *et al.*, Precise Determination of Electroweak Parameters in Neutrino-Nucleon Scattering, *Phys. Rev. Lett.* **88**, 091802 (2002) 8

[10] S. Bethke, The 2009 World Average of α_s, *Eur. Phys. J.* C**64**, 689-703 (2009), arXiv:0908.1135v2 [hep-ph] 9

[11] V. N. Gribov and L. N. Lipatov, *Sov. J. Nucl. Phys.* **15**, 438 (1972); G. Altarelli and G. Parisi *Nucl. Phys. B***126**, 298 (1977); Y. L. Dokshitzer *Sov. Phys. JETP* **46**, 641 (1977). 10

[12] G. Watt, http://projects.hepforge.org/mstwpdf/plots/plots.html 11

[13] J. Stirling, http://projects.hepforge.org/mstwpdf/plots/plots.html 15

[14] C. Grojean, M. Spiropulu, Proceedings of the 2009 European School of High-Energy Physics, Bautzen, Germany, 14 - 27 June 2009, arXiv:1012.4643 [hep-ph] 1-44 (2009) 16

[15] The LEP Collaborations ALEPH, DELPHI, L3 and OPAL and the LEP Electroweak Working Group, arXiv:hep-ex/0612034; http://www.cern.ch/LEPEWWG/ 16

[16] The ALEPH, DELPHI, L3, OPAL and SLD Collaborations, the LEP Electroweak Working Group and the SLD Electroweak and Heavy Flavour Groups, *Phys. Rept.* **427** (2006) 257. 16

[17] T. Kluge, K. Rabbertz, and M. Wobisch, fastNLO: Fast pQCD Calculations for PDF Fits, arXiv:hep-ph/0609285 (2006) 17

[18] The ATLAS Collaboration *et al.*, Combined search for the Standard Model Higgs boson using up to 4.9 fb^{-1}of pp collision data at $\sqrt{s} = 7$ TeV with the ATLAS detector at the LHC, *Phys. Lett.* B**710**, 4966 (2012) 18

[19] The CMS Collaboration *et al.*, Combined results of searches for the standard model Higgs boson in pp collisions at $\sqrt{s} = 7$ TeV, *Phys. Lett.* B**710**, 2648 (2012) 18

[20] U. Amaldi, W. de Boer, H. Furstenau, Comparison of Grand Unified Theories with electroweak and strong Coupling Constants measured at LEP *Phys. Lett.* B**260**, 447-455 (1991) 18, 20

[21] D. I. Kazakov, Beyond the Standard Model (In Search of Supersymmetry), arXiv:hep-ph/0012288v2 (2001) 19

[22] N. Arkani-Hamed, S. Dimopoulos, G. Dvali, *Phys. Lett.* B**429** (1998), hep-ph/9803315 263; I. Antoniadis, N. Arkani-Hamed, S. Dimopoulos and G. Dvali, *Phys. Lett.* B**436** (1998), hep-ph/9804398 257 19

[23] L. Randall, R. Sundrum, A Large Mass Hierarchy from a Small Extra Dimension, *Phys. Rev. Lett.* **83**, 3370-3373 (1999), arXiv:hep-ph/9905221v1 19

[24] S. P. Martin, A Supersymmetry Primer, arXiv:hep-ph/9709356v6 (1997) 20

[25] H. Georgi, AIP Conf Proc. 23 575 (1975); H. Fritzch and P. Minkowski, *Ann. Phys.* **93** 193 (1975) 20

[26] The CDF Collaboration, Search for Pair Production of Scalar Top Quarks Decaying to a tau Lepton and a b Quark (CDF note 7835) (2005) 21

[27] I. Hinchliffe, Use of Taus in ATLAS, eConf C0209101 (2002) WE13, arXiv:hep-ph/0210340v1 21

[28] Z. Czyczuła, Search for New Physics in Tau-pair Events in ATLAS at the LHC Doctoral Dissertation, Niels Bohr Institute, Faculty of Science, University of Copenhagen (2009) 21, 56

[29] M. A. Doncheski, R. W. Robinett, Third-generation leptoquark decays and collider searches, *Phys.Lett.* B**411**, 107-111 (1997), arXiv:hep-ph/9707486v1 21

[30] M. L. Perl *et al.*, Evidence for Anomalous Lepton Production in $e^+ - e^-$ Annihilation, *Phys. Rev. Lett.* **35**, 14891492 (1975) 21

[31] E.I. Shibata, Hadronic structure in $\tau^- \to \pi^-\pi^-\pi^+$ neutrino decays, eConf C0209101 TU05 (2002); Nucl.Phys.Proc.Suppl.123, 40-46 (2003), arXiv:hep-ex/0210039v1 22

[32] D. Asner *et al.* (CLEO Collaboration), Hadronic Structure in the Decay $\tau^- \to \nu_\tau \pi^- \pi^0 \pi^0$ and the Sign of the Tau Neutrino Helicity, *Phys. Rev.* D**61** 112002 (2000), arXiv:hep-ex/9902022v1 22

[33] T. Sjostrand, S. Mrenna and P. Skands, PYTHIA 6.4 Physics and Manual, JHEP **0605** (2006) 026 [hep-ph/0603175] 23

[34] M.L. Mangano, M. Moretti, F. Piccinini, R. Pittau, A.D. Polosa, ALPGEN, a generator for hard multiparton processes in hadronic collisions, JHEP **0307** (2003) 001, [arXiv:hep-ph/0206293v2] 23

[35] G.Corcella, I.G.Knowles, G.Marchesini, S.Moretti, K.Odagiri, P.Richardson, M.H.Seymour, B.R.Webber, HERWIG 6.5: an event generator for Hadron Emission Reactions With Interfering Gluons (including supersymmetric processes), JHEP **0101** 010 (2001), [hep-ph/0011363]; hep-ph/0210213 24

[36] S. Frixione and B. R. Weber, Matching NLO QCD computations and parton shower simulations, JHEP **0206** (2002) 029 [arXiv:hep-ph/0204244] 24

[37] Z. Was, TAUOLA the library for tau lepton decay, and KKMC/KORALB/KORALZ/... status report, Nucl.Phys.Proc.Suppl. **98** (2001) 96-102, [arXiv:hep-ph/0011305v1] 24

[38] The CERN Large Hadron Collider: Accelerator and Experiments vol. 1, JINST 3 S08001 (2008) 25, 26, 28

[39] http://lhc.web.cern.ch/lhc/ 26

[40] The ATLAS Experiment, https://twiki.cern.ch/twiki/bin/view/AtlasPublic 28, 29, 42

[41] G. Papotti, Luminosity Analysis, CERN-2011-005 266-269 (2011) 28

[42] The ATLAS Experiment, https://twiki.cern.ch/twiki/bin/view/AtlasPublic/EventDisplayPublicResults 29

[43] The CERN Large Hadron Collider: Accelerator and Experiments vol. 1, JINST 3 S08003 (2008) 29, 31, 32, 34, 35, 36, 37, 38, 39, 46, 47

[44] A. Artamonov *et al.*, The ATLAS Forward Calorimeter, JINST 3 P02010 (2008) 37

[45] The ATLAS Experiment, https://twiki.cern.ch/twiki/bin/view/AtlasPublic/TauTriggerPublicResults 42, 43, 108

[46] The ATLAS Collaboration, Expected Performance of the ATLAS Experiment: Detector, Trigger and Physics, (CERN-OPEN-2008-020) (2008) 43

[47] S. Agostinelli *et al.* (GEANT4 Collaboration), Geant4: A simulation toolkit, *Nucl. Instrum. Meth.* A**506** 250 (2003) 45

[48] W. Lampl *et al.*, Calorimeter Clustering Algorithms : Description and Performance, ATL-LARG-PUB-2008-002 (2008) 47

[49] T. Barillari *et al.*, Local Hadronic Calibration, ATL-LARG-PUB-2009-001-2 (2009) 47

[50] T. Cornelissen *et al.*, The new ATLAS Track Reconstruction (NEWT), *J. Phys.: Conf. Ser.* **119** 032014 (2008) 46

[51] G. Piacquadio *et al.*, Primary Vertex Reconstruction in the ATLAS Experiment at LHC, *J. Phys.: Conf. Ser.* **119** 032033 (2008) 47

[52] M. Cacciari, G. P. Salam, G. Soyez, The anti-kt jet clustering algorithm, JHEP **0804**, 063 (2008), [arXiv:0802.1189 [hep-ph]] 48, 49

[53] The ATLAS Collaboration, Jet energy scale and its systematic uncertainty in proton-proton collisions at $\sqrt{s}$=7 TeV in ATLAS 2010 data, ATLAS-CONF-2011-032 (2011) 49, 112

[54] The ATLAS Collaboration, Performance of the Reconstruction and Identification of Hadronic Tau Decays with ATLAS, ATLAS-CONF-2011-152, (2011) 49, 50, 51, 53, 55, 56, 58, 59, 61, 111

[55] The ATLAS Collaboration, Reconstruction, Energy Calibration, and Identification of Hadronically Decaying Tau Leptons in the ATLAS Experiment, ATLAS-CONF-2011-077 (2011) 53, 57

[56] A. Hoecker *et al.*, TMVA 4 Toolkit for Multivariate Data Analysis with ROOT Users Guide, PoS ACAT:040 (2007), [arXiv:physics/0703039v5 [physics.data-an]] 56, 57

[57] The ATLAS Collaboration, Measurement of hadronic tau decay identification efficiency using W$\rightarrow \tau\nu$ events, ATLAS-CONF-2011-093 (2011) 59, 60, 110, 119

[58] M. R. Whalley, D. Bourilkov, R. C. Group, The Les Houches Accord PDFs (LHAPDF) and Lhaglue, [arXiv:hep-ph/0508110v1] (2005) 103

[59] The ATLAS Collaboration, Expected electron performance in the ATLAS experiment, ATL-PHYS-PUB-2011-006 (2011) 60, 62

[60] The ATLAS Collaboration, Muon reconstruction efficiency in reprocessed 2010 LHC proton-proton collision data recorded with the ATLAS detector, ATLAS-CONF-2011-063 (2011) 62, 86, 121, 123

[61] The ATLAS Collaboration, Reconstruction and Calibration of Missing Transverse Energy and Performance in Z and W events in ATLAS Proton-Proton Collisions at $\sqrt{s}$=7 TeV, ATLAS-CONF-2011-080 (2011) 63, 65

[62] The ATLAS Collaboration, Observation of $W \rightarrow \tau\nu$ Decays with the ATLAS Experiment, ATLAS-CONF-2010-097 (2010) 67

[63] The ATLAS Collaboration, Measurement of the W to tau nu Cross Section in pp Collisions at $\sqrt{s} = 7$ TeV with the ATLAS experiment, *Phys.Lett.* B**706** 276-294 (2012), [arXiv:1108.4101v2 [hep-ex]] 67

[64] The ATLAS Collaboration, Observation of Z$\rightarrow \tau_h\tau_l$ Decays with the ATLAS detector, ATLAS-CONF-2011-010 (2011) 67

[65] The ATLAS Collaboration, Measurement of the $Z \rightarrow \tau\tau$ Cross-Section with the ATLAS Detector, *Phys.Rev.* D**84** 112006 (2011), [arXiv:1108.2016v2 [hep-ex]] 67, 73, 108

[66] E. Abouzaid, H. Frisch, The Ratio of W + N jets To Z/gamma + N jets As a Precision Test of the Standard Model, *Phys.Rev.*D**68** 033014 (2003), [arXiv:hep-ph/0303088v1]

[67] The ATLAS Collaboration, A measurement of the ratio of the W and Z cross sections with exactly one associated jet in pp collisions at $\sqrt{s} = 7$ TeV with ATLAS, *Phys.Lett.* B**708** 221-240 (2012), [arXiv:1108.4908v2 [hep-ex]] 68

[68] S. Allwood-Spires *et al.*, Monte Carlo samples used for top physics, ATL-PHYS-INT-2010-132 (2010) 68

[69] K. Melnikov and F. Petriello, 2006 *Phys. Rev.* D**74**, 114017 (2006); R. Gavin, Y. Li, F. Petriello, S. Quackenbush, Comput.Phys.Commun.182:2388-2403 (2011), [arXiv:1011.3540v1 [hep-ph]]; S. Catani, L. Cieri, G. Ferrera, D. de Florian, M. Grazzini, *Phys.Rev.Lett* **103** 082001 (2009), [arXiv:0903.2120v1 [hep-ph]] 68

[70] A. Sherstnev, R. S. Thorne, Parton Distributions for LO Generators, *Eur.Phys.J.* C**55** 553-575 (2008), [arXiv:0711.2473v3 [hep-ph]] 68

[71] P. M. Nadolsky *et al.*, Implications of CTEQ global analysis for collider observables, *Phys.Rev.*D **78** 013004 (2008), [arXiv:0802.0007v3 [hep-ph]] 68

[72] J. Pumplin, *et al.*, New Generation of Parton Distributions with Uncertainties from Global QCD Analysis, JHEP 0207:012 (2002), [arXiv:hep-ph/0201195v3] 68

[73] The ATLAS Collaboration, Data-Quality Requirements and Event Cleaning for Jets and Missing Transverse Energy Reconstruction with the ATLAS Detector in Proton-Proton Collisions at a Center-of-Mass Energy of $\sqrt{s} = 7$ TeV, ATLAS-CONF-2010-038 (2010) 71

[74] The ATLAS Collaboration, Performance of the Missing Transverse Energy Reconstruction and Calibration in Proton-Proton Collisions at a Center-of-Mass Energy of $\sqrt{s} = 7$ TeV with the ATLAS Detector, ATLAS-CONF-2010-057 (2010) 76

[75] The ATLAS Collaboration *et al* 2011 Updated Luminosity Determination in pp Collisions at sqrt(s)=7 TeV using the ATLAS Detector (ATLAS-CONF-2011-011) 102

[76] The ATLAS Experiment, https://twiki.cern.ch/twiki/bin/view/AtlasPublic/MuonTriggerPublicResults 121